8-2015

A study of diblock copolymer/charged particle nanoporous membranes; morphology, design and transport property modeling

Bo Zhang
University of Tennessee - Knoxville, bzhang13@vols.utk.edu

To the Graduate Council:

I am submitting herewith a dissertation written by Bo Zhang entitled "A study of diblock copolymer/ charged particle nanoporous membranes; morphology, design and transport property modeling." I have examined the final electronic copy of this dissertation for form and content and recommend that it be accepted in partial fulfillment of the requirements for the degree of Doctor of Philosophy, with a major in Chemical Engineering.

Brian J. Edwards, Major Professor

We have read this dissertation and recommend its acceptance:

Thomas A. Zawodzinski, Bamin Khomami, Dibyendu Mukherjee

Accepted for the Council:
Dixie L. Thompson

Vice Provost and Dean of the Graduate School

(Original signatures are on file with official student records.)

A study of diblock copolymer/charged particle nanoporous membranes; morphology, design and transport property modeling

A Dissertation Presented for the

Doctor of Philosophy

Degree

The University of Tennessee, Knoxville

Bo Zhang

August 2015

Dedication

This dissertation is dedicated to my parents, Jinkui Zhang and Xueling Li, my advisor, Dr. Brian J Edwards, and my girlfriend, Jing Wang.

Acknowledgements

It takes several years to produce up a Ph. D. dissertation, and it is impossible to do all this work alone. During the past four years, many professors, colleagues, and friends have given me a lot of help in my work and life. I sincerely thank to my supervisor, Dr. Brian Edwards, for his support in all aspects of my doctorate program. Dr. Edwards always motivated me to do better and higher quality research. Dr. Edwards allowed me to choose my research topic, which led me to have indispensable experiences in various research areas. I thank Drs. Thomas Zawodzinski, Bamin Khomami, and Dibyendu Mukherjee for serving on my committee and their critical questions and comments during preparation of this dissertation. I also appreciate the kindness, help, and support from all CBE staff (Rita Gray, Kat Forst, Amy Brewer, Jennifer Wolfenbarger, Amber Tipton, Marie Parigin). Last, but not the least, I express my sincere thanks to my family for their love, patience, and continuous support. They always encouraged me to achieve my goals, and were always next to me whenever I needed help and encouragement.

Abstract

A combination of self-consistent field theory and density functional theory was used to examine the stable, 3-dimensional equilibrium morphologies formed by diblock copolymers with a neutral or charged nanoparticle attached either between the two blocks or at the end of copolymer. Particle size was varied between one and four tenths of the radius of gyration of the copolymer. Phase diagrams were constructed and analyzed in terms of thermodynamic diagrams to understand the molecular-level self-assembly processes with the aim of determining the appropriate morphologies used as nanoporous membranes, (*i.e.* the periodic, hexagonal arrays of cylinders wherein the particles would primarily be located within the interface between the two blocks). Key factors were determined to be the particle position, particle size, interactions between the blocks and particles, and the copolymer composition and molecular weight.

Self-assembly of a diblock copolymer under an external field was also investigated by overlaying a free energy for an entropic chain, herein modeled as finitely-extensible nonlinear elastic dumbbell, onto the standard diblock copolymer free energy expression along with the associated energy of the external field. The additional influence of the external field, dramatically affected the overall chain extension and orientation, thus commensurately affecting the free energy. As a consequence, the stable, equilibrium properties of the diblock copolymer system were directly responsive to changes in the global properties. The results demonstrated a promising strategy for controlling the polymer segmental orientation, the domain densities, as well as the microphase domain dimensions.

We also studied the conductivity of perfluorosulfonate acid (PFSA) polymer membranes using a nanoporous network model. The transport of hydronium ions inside the network was expressed by an extended Nernst-Einstein equation. Percolation theory was used to modify the diffusion coefficient and to illustrate the transport mechanism. The conductivity of typical PFSA membranes was quantified in terms of water content, equivalent weight, temperature, and polymer architecture. Theoretical predictions of this model were compared against experimental data for four different membranes: Nafion, Membrane C, a Dow membrane, and a 3M membrane at different water contents and temperatures. The comparisons displayed qualitative and quantitative agreement between theory and experiment.

Table of Contents

List of Tables

List of Figures

Chapter 1

Introduction

The goals of this dissertation are as follows:

1st: To investigate the morphologies of the diblock copolymer/charged particle system via a combination of self-consistent field theory and density functional theory.

2nd: To propose a general proton conductivity equation for the perfluorosulfonate acid (PFSA) membranes using continuum percolation theory.

The progress toward these goals will be presented in successive chapters of this dissertation.

1.1 Morphology of Diblock/Charged Particle Systems

The design of microporous thin films (especially multicomponent thin film) is an emerging area of technology with great potential to address many outstanding applications in the areas of energy conversion and storage, filtration technology, targeted drug delivery, biosensors, microscale separation processes, *etc*. As one example, consider the nanofiltration process.[1, 2] The key benefit of nanofiltration membranes over other available types of separation processes (such as ultrafiltration and reverse osmosis) is their capability to retain small molecules and ions, both organic and inorganic, at high throughput levels; hence steric exclusion is an important factor in their application. However, another important factor to their extensive application in the separations and purification industries is their ability to retain molecules and ions based on charge; *i.e.*, the so-called "Donnan exclusion."[3, 4] Several types of nanofiltration membranes, organic

and inorganic, have been developed and produced on an industrial scale, such as zeolite membranes, titanium dioxide membranes, polyamide membranes, sulfonated polymer membranes, *etc.*[5-8] One microporous example is Nafion, a perfluorosulfonic acid membrane, which is a well-studied material that has been in use for over 50 years by the fuel cell research community in spite of the fact that it has severe limitations in terms of maximum conductance capacity, mechanical and thermal stability, and hydration level.[9-11] The primary reason for the ubiquitous use of Nafion is simply that in all these 50 years, nothing substantially better has been discovered.

The pore size, size distribution and component distribution are three key factors affecting the performance of microporous membranes. Furthermore, an effective microporous membrane should also remain insoluble in the operating environment, possess a low thickness, and be mechanically, chemically, and thermally stable.[12] Effective methods of microporous membrane preparation nowadays include interfacial polymerization, layer-by-layer self-assembly, surface modification, and so on. However, all these could be very complex processes; *e.g.*, interfacial polymerization depends on many conditions, such as the chemical properties of the monomer and solvent, pH, temperature, concentration of monomer, and phase transfer catalysis, which lead to control and consistency issues in industrial manufacture.[7] In 1991, layer-by-layer self-assembly technology was first developed by Decher to prepare nanofiltration membranes through alternating assembly of anionic and cationic layers.[13] Another well-known method of microporous membrane production is using hydrophilizing agents (sulfuric, hydrochloric, nitric, and phosphoric acids) to modify reverse osmosis membranes.

However, the mechanical properties are generally adversely affected during the modification.[14]

Microporous membranes composed of homopolymers with functional side-chains, such as Nafion, are also application-limited by their mechanical and thermal stability, irregular pore microstructure, hydration capacity, and so on. Diblock copolymers, in which the two blocks are composed of mutually immiscible monomeric segments, offer one new avenue of progress on account of the wide range of thin film morphologies that can be formed due to the microphase separation that results from the chemical tethering of the blocks.[15-21] This separation occurs in response to a delicate balance between the enthalpic driving force of the constituent copolymer blocks to phase separate and their inherent entropic driving force to avoid extended chain configurations. A few examples that illustrate the breadth of possible thin-film morphologies are lamellar phases (both parallel and perpendicular to the film width) of alternating blocks, hexagonally packed cylindrical structures formed by one of the copolymer blocks surrounded by a matrix phase of the other block, spheroids of one block surrounded by the other, and more.[15-24] The key advantages of these diblock membranes over homopolymer derivatives are the regular pore structure, controllable size, uniform size distribution, as well as the ability to choose the blocks of the copolymer to suit particular applications; *i.e.*, the matrix phase polymer can be chosen to provide thermal or mechanical stability to the membrane and impermeability, whereas the minority phase component can be tuned to the desired physiochemical properties of the membrane. Furthermore, the minority phase polymer can be so chosen such that it can be thermally or chemically degraded without affecting

the matrix phase, thus creating a porous network within a mechanically and thermally stable, impermeable thin film.[25, 26] The pore size and size distribution of these pores can be controlled by a suitable choice of immiscible copolymer blocks and variations of the relative length of each block.

Self-assembly of block copolymers (BCP) with nanoparticles (NP) provides an even more promising means to construct microporous membranes with specific applications or requirements, since the BCP-NP system can not only self-assemble into an enormous range of interesting nanoscale morphologies,[13, 25, 27-39] but also allows for the possibility of tailoring the physiochemical properties of the microphase structure to enhance or modify key elements of the membrane functionality, such as conductivity, ionic selection and exclusion, *etc*. Composites of nanoparticles and copolymers lead to the self-assembly of a diverse array of complex mesophases, depending on such factors as particle size, chemical properties of the particles and blocks, volume fraction of a given block, *etc*.[30, 32, 36, 37] Many complex mesophases of particles and copolymer mixtures depend on such factors as particle size, chemical properties of the particles and blocks, applied external field, volume fraction of a given block, etc.[24, 40]

In most research carried out to date, the copolymer/nanoparticle systems have been primarily composite systems; *i.e*., mixtures of particles and the diblock copolymers. Recently, BCP-NP systems have been studied in which the nanoparticles have been chemically tethered to the copolymer.[26, 41-44] This incorporates an additional constraint into the self-assembly of membrane morphology since the particle contributions to the free energy of the system help to direct the formation of the microstructure of the

material; *i.e.*, the nanoparticles are directly associated with the entropic configurational arrangements of the copolymer block segments, rather than merely energetically (either actively, or merely through screening opposite copolymer block segments). In other words, the particles cannot simply be pushed into membrane regions that minimize the energetic interactions between the blocks of the copolymer, but must be accommodated in the entropic self-assembly process as part of the copolymer chain. This can result in additional interesting morphologies with more regular patterning (with respect to particle density) than BCP-NP composites without particle/chain tethering.[41-44]

Researchers have studied the self-assembled BCP-NP systems for both inorganic (Si, Au) and organic (polyhedral oligomeric silsesquioxane, POSS) molecules experimentally.[45, 46] The polystyrene-capped gold BCP-NP system has been studied in both aqueous and organic media for a wide range of chain lengths. These studies showed that a fairly uniform particle distribution could be produced throughout the film.[45] A block copolymer tethered with POSS can form arrays of cylindrical channels, with radii of approximately 9 nm, by spin coating on a silicon substrate and then exposing to solvent vapor.[26] The location and orientation of nanoparticles within the polymer matrix can also be controlled by their selectivity and size, opening up a wide range of potential applications.[27]

To meet the numerous and demanding technological applications of thin film membranes, it will ultimately be necessary to possess the capability to tailor specific membrane morphologies using theoretical methods and simulations. For example, in nanofiltration membranes, one must be able to control not only the size of the pores but

also their charge (Donnan) exclusion via surface charge density, the latter of which is predominantly controlled by the nanoparticles. Much experimental effort is currently being expended in this area following the intuitive pathways described above, but very little theoretical guidance is available to allow a systematic approach toward future directed membrane self-assembly.

Until relatively recently, the development of novel membrane materials has been rate-limited by the process of experimental determination; *i.e.*, the reliance on physical intuition to guide trial-and-error experimentation of potential new membrane materials. This involves lengthy and time-consuming chemical syntheses, membrane preparation, and physical testing. During the past twenty years, however, a combination of experimentation, theory, and simulation have been applied to understanding the key physical principles involved in membrane formation, with the result being a growing body of knowledge regarding the self-assembly of microporous media. Theoretical advances have led to new simulation algorithms as well as adaptation of older techniques, such as Monte Carlo,[29, 39] Molecular Dynamics,[47, 48] Dissipative Particle Dynamics,[31, 34] Self-Consistent Field Theory,[15-17] and Hybrid Field Theory,[28, 33] to the study of microporous membrane formation.

A complete mean field theory for copolymers was first developed by Helfand, which was based on the Gaussian random walk model, in 1975.[49, 50] The real-space, self-consistent field theory (SCFT) is only one of the approximations of this complete mean field theory, which has proven to be a powerful technique that is successful for discovering and predicting morphologies of complex copolymers, both in bulk and in

solution.[23] Much effort has been expended on this type, such as the traditional A-B diblock copolymer,[51] A-B-C linear triblock copolymers,[52] A-B-C star triblock copolymers,[53] polymer rings,[54] and so on, which were all investigated in either 2 or 3 dimensions during the past two decades. Recently, much attention has been focused on the effect of using chemically pattern substrates to control the resulting system morphology,[22, 23] as well as the simulation box size and dimensional confinement effects on the resulting phase diagrams, free energy, morphologies and disorder-order transition critical point,[41] and the polymer chain behavior in a dilute solutions.[32] The theoretical prediction of copolymer mixtures, (such as with hard sphere particles, either free or tethered to the blocks block,[37, 41, 43] or short ligands[55]) also have drawn a lot of attention.

Thompson *et al*. have developed a "SCFT/DFT" approach that combines self-consistent field theory for the blocks with density functional theory (DFT) for the nanoparticles to examine hybrid composite morphologies.[36, 37] Recent theoretical research along these lines has demonstrated that these BCP-NP systems can self-assemble into a variety of interesting morphologies with variable particle distributions concentrated at the interfaces between the distinct polymer-rich regions of the self-assembled structure.[28, 29, 32, 33, 36, 42] Tethering neutral nanoparticles to one end of the BCP chain directs additional self-assembled structures, including several types of micellar structures, such as rod-like micelles, vesicles, and sphere-like micelles.[28, 30, 32, 43, 44]

Zhu *et al*.[43] performed primarily 2-dimensional simulations of BCP-NP systems with a nanoparticle tethered to one end of the BCP chain. Two cases were studied, one in which the particles were neutral to both blocks of the BCP, and one in which the particles disfavored both of the blocks. In cases where a neutral nanoparticle (P) was tethered to the B block of an AB copolymer, three distinct long-range ordered structures were observed. At constant particle radius, when the volume fraction of the A block (f_A) was low, the ABP molecules packed into a hexagonal array of A-rich cylinders surrounded by a B-rich matrix, which preferentially contained the majority of the particles. At intermediate values of f_A, lamellar phases were formed, again with the nanoparticles preferentially located in the B-domains. At high values of f_A, a narrow region of B-rich cylinders was present, and again the nanoparticles were mostly confined to the B-rich domains (*i.e.*, the cylinders). Changing the particle radius had no effect on the qualitative characteristics of the phase diagram, although increasing particle size tended to narrow the f_A-range of all three ordered phases. When the interactions of the nanoparticles were unfavorable to both blocks of the copolymer, a wider range of ordered structures was observed, such as morphologies where the particles formed hexagonal arrays of cylindrical domains within a matrix of the AB copolymer and lamellar structures where particle-rich cylinders were located within the B-rich domains. Zhu *et al.* also performed several fully 3-d simulations, apparently corroborating in these cases the extension of their equilibrated 2-d morphologies to 3-dimensional space, although additional domains of nanospheres arranged in cubic and quasi-face-centered cubic structures were also

noted. However, for many points within the investigated parameter space, it is not clear how the restriction to 2-d simulations affected the resulting phase diagrams.

The second chapter of this dissertation examines the phase diagrams of BCP-NP systems in which the nanoparticles are tethered either between the two blocks or at the end of one of the blocks using a combination of self-consistent field theory and density functional theory in a fully 3-dimensional, as described by Thompson, *et al.*[36, 37] The nanoparticles are allowed to interact (via a standard interaction potential) with neither or both blocks of the copolymer (both favorably and unfavorably), and the stable equilibrium morphologies are obtained via a suite of 3-dimensional simulations. Phase diagrams of the equilibrium morphologies are constructed, of a similar nature to those of Zhu *et al.*,[43] and are compared with their results in the overlapping cases to validate our simulations and to explore the differences between their 2-d and our 3-d simulations. Using these phase diagrams, identification of several key parameter ranges (in terms of molecular weight of the blocks, interaction potentials, nanoparticle position along the BCP chain, *etc*.) are identified that might serve as a guide to future morphological tailoring studies of microporous membranes. The primary goal is to determine parameter ranges wherein one can obtain morphologies that are amenable to applications in microporous membrane technology, such as cylinders of one component of the BCP arrayed within a matrix of the other, with a heavy concentration of nanoparticles at the interface between the two phases. Selective thermal or chemical degradation of the cylindrical BCP component could then lead to a membrane of charged nanotubes,

tailoring both steric and charge exclusion into potential microporous membrane applications.[25, 26]

The third chapter of this dissertation is to extend the suite of simulations in order to study the effect of particle size in fully 3-dimensional geometries to discern not only the effect of particle size on the observed morphology, but also to understand the microscale physics of the self-assembly process in terms of the system free energy, internal energy, and entropy. Similar cases of tethered nanoparticle/copolymer systems are examined as in the previous work using a combination of self-consistent field theory and density functional theory, as described by Thompson, *et al.*[36, 37] The nanoparticles are allowed to interact (via a standard interaction potential) with neither or both blocks of the copolymer, and the stable equilibrium morphologies are also obtained via a suite of 3-dimensional simulations. Phase diagrams of the equilibrium morphologies are constructed, of a similar nature to those of Zhang *et al.*,[41] as presented in Ch. 2, for several values of the particle radius (R_g) ranging from 0.1 to 0.4 R_g, where the symbol R_g represents the radius of gyration of the diblock copolymer chain. The thermodynamics of the self-assembly process are also evaluated to aid understanding of the configurational interactions that lead to the various morphologies observed in the simulations for the various cases.

In the fourth chapter of this dissertation, a new type of self-consistent mean-field model is developed primarily for the purpose of describing equilibrium self-assembly of a generic diblock copolymer system under application of an external field. This novel type of self-consistent field theory is developed to include local chain properties within the

self-consistent free energy expression along with the associated energy of the external field. This is necessary because traditional self-consistent field theory is expressed in terms of local segmental densities which carry no direct information regarding local chain stretching and orientation, both of which can be dramatically affected by the application of an external electric or magnetic field. In order to account properly for the application of an external field, it was necessary to overlay a free energy expression for an entropic chain, herein modeled as a finitely-extensible nonlinear elastic (FENE) dumbbell, onto the standard free energy expression of a diblock copolymer within self-consistent field theory, which is essentially a Gaussian chain. The additional influence of an external field can possibly dramatically affect the segmental, and hence overall, chain extension and orientation, thus commensurately affecting the overall system free energy. As a consequence, the stable, equilibrium properties of the diblock copolymer system were directly responsive to changes in the cumulative properties of an individual polymer chain. This investigation reveals the contributing factors that affect the stable morphology of a generic diblock copolymer system. The morphological phase diagram is thus influenced by the typical parameters, such as volume fractions of the blocks and the energetic interaction parameter between the opposite chain segments, but also by the strength and orientation of the applied external field. The physical and thermodynamic properties of the copolymer system are also highly affected by the external field, such as the segmental density distributions, segmental orientation and extension, the degree of microphase separation, and the overall free energy, internal energy, and entropy of the system.

The core of the self-consistent field theory (SCFT) is a coarse-grained model in which a polymer was described as a Brownian random walk of a certain number of steps (N) with constant step length, l.[51] The step length is treated as the polymer segmental length and N is the number of statistical chain segments (one segment may contain one or many individual monomeric units). However, the direction of the random step is not necessarily always isotropic in the presence of external forces, such as an external field, pressure gradient, or shear stress, since compression and/or elongation may occur in a certain direction. The FENE model, which was first proposed by Warner when he studied the steady shear flow, provides a potential solution to this problem.[56] This model is based upon the Hookean (linearly elastic) dumbbell model, which is the simplest model for linear flexible polymer.[57] However, whereas the Hookean dumbbell allows for the unrealistically infinite extension of the molecules, the FENE dumbbell can be parameterized such that the spring is very stiff, hence limiting the segmental extension to physically realistic values.

The FENE model has been extensively used in numerical calculations of equilibrium and flow properties of polymer solutions and melts; *e.g.*, Brownian dynamics simulations.[58] Based on the difficulty of solving the FENE model, which is expressed in terms of a probability distribution function for dumbbell orientation and bead locations, researchers have developed several different closed-form expressions for significantly simplifying the averaging of orientational and positional degrees of freedom, such as the FENE-P model, proposed by Peterlin, and the FENE-CR model, proposed by Chilcott and Rallison.[59] The FENE, FENE-P and FENE-CR have a very similar behavior in

steady state and transient shear and elongational flows, and there is no quantifiable difference in their equilibrium distribution functions.

The FENE-P model, adopted in this work, provides a very good approximation of Hooke's Law for low values of the trace of the conformation tensor. In the FENE-P model, all the necessary information is contained within the second moment of the distribution function.[60] Hence this model provided a very convenient method of introducing the concept of local segmental orientation and extension/compression into the traditional SCFT simply by introducing the known free energy expression for the FENE-P model into the original SCFT expression for the block copolymer free energy, along with the requisite energy expression for the effects of the applied external field. Hence, the resulting novel SCFT method makes possible a realistic, consistent simulation for determining the self-assembled phase diagram of A-B block copolymer materials under the application of an external field, and associated effects and dimensions.

1.2 Conductivity in Perfluorosulfonic Acid Membranes

One of the most efficient alternative clean energy conversion devices for long-term use is the polymer electrolyte membrane fuel cell (PEM-FC). The essential but performance-limiting component of a PEM-FC is the proton exchange membrane. Perfluorosulfonic acid (PFSA) polymer membranes are the most widely adopted in PEM-FC technology; for examples, DuPont's Nafion, Membrane C of Chlorine Engineers Corp., Dow's XUS 13204.10, Aciplex of Asahi Kasei Corp., and membranes developed by 3M Corp., all of which are currently commercially available.[61] Hydrogen gas is

commonly used as an energy source in a PEM-FC by splitting the H_2 molecules into pairs of protons and electrons. The hydrated protons move through the membrane, while the electrons pass through an external circuit. The efficiency of the PEM-FC depends strongly on the rate of transport of protons, which is directly related to the morphology of the membrane.

The chemical structure of a PFSA polymer combines a hydrophobic backbone with short hydrophilic side chains terminated with sulfonic acid groups. The chain backbone provides the structural support of the membrane, while the sulfonic acid groups donate protons to water clusters within the hydrated pores of the membrane.

During the last two decades, numerous physical and chemical property data of PFSA polymer membranes were accumulated under different operational conditions; however, their morphological characteristics are still subject to debate. Various membrane structural models have been proposed based on the monomeric chemical properties of typical PFSA polymers as well as data from neutron and small angle X-ray scattering experiments. In hydrated membranes, the PFSA molecules are generally classified as assuming various types of model morphologies, such as spherical clusters,[47, 62] the reverse micelle-channel model,[63] polymer bundles,[64, 65] channel networks,[66] layered structures,[67] and parallel cylindrical pores.[68] Of course, the exact nature of the nanoporous morphology is likely highly dependent on the water content.[11] Several of these typical morphologies were compared by Schmidt-Rohr and Chen based upon experimental data from small-angle X-ray scattering data of Nafion, which was compared to simulated structures of the hydrated PFSA environment. [68] These simulations

suggested that a Nafion morphology based on a parallel cylindrical pore channel array gave a better match to the X-ray scattering data than the spherical water cluster model, channel network model, or the polymer-bundle model. Nevertheless, the conclusion is still subject to vigorous debate.

The hypothesis of cylindrical conduction channels within PFSA membranes has been used previously to study the transport properties and proton conductivity within these materials. Din and Michaelides performed molecular dynamics simulations to study the movement of proton and water within pores of radii 9.36 and 12.24 Å.[69] They found that the proton and water distributions depended on the water content and wall surface-charge density. Paddison *et al*. derived a statistical model for a similar system in order to investigate the wall surface-charge density dependence.[70, 71] This model was extended to incorporate species transport equations within the pores by Kumar *et al*.;[72] these researchers were able to predict conductivities of Nafion membranes as functions of pore radii, surface-charge distribution, water content, *etc*. Although fundamental, these transport equations require the specification of several structural parameters (such as pore radius, charge distribution, pore length, *etc*.) that cannot easily be obtained directly from experiments. In the fifth chapter of this dissertation, we exploit some key architectural characteristics of the PFSA macromolecules, coupled with percolation theory, to calculate the diffusion coefficient that dictates the strength of the conduction effect of the Nernst-Einstein equation under different environmental conditions of water content and temperature.

In the model derived herein for conductivity and dry membrane density calculations, we assumed that the PFSA polymer membrane was composed of a nanoporous network of indeterminate morphology. The sulfonic acid groups at the terminal position of the side chains were assumed to be distributed randomly on the inside walls of the pores. For a given PFSA polymer membrane, the free volume of the dry membrane was calculated and assumed to equate to the total dry-channel volume of the nanoporous network. Under exposure to humidified air, water enters into the nanopores and hydrates the protons of the sulfonic acids groups. These pores were assumed to be deformable. The expression of membrane conductivity was based on the Nernst-Einstein equation, which depends directly on the diffusion coefficient of hydronium ion. This coefficient was developed using continuum percolation theory, which also aided the theoretical understanding of the proton transport mechanism. Predictions of this model were compared against experimental data for four different types of PFSA membranes: Nafion 117, Dow XUS 13204.10, Membrane C (produced by Chlorine Engineers, Japan), and a 3M membrane.

Chapter 2

Simulations of Block Copolymer/Charged Particle Systems at Constant Particle Radius

This chapter is based on the published paper

"A self-consistent field study of diblock copolymer/charged particle system morphologies for nanofiltration membranes," B. Zhang, X. Ye, and B.J. Edwards, *J. Chem. Phys.*, **139**, 244909 (2013).[41]

2.1 Methodology

We examine two block copolymer/nanoparticle (BCP-NP) systems: (a) the particle is tethered at the free end of the B block of the copolymer (ABP), and (b) the particle is tethered between the two blocks (APB). The free energy of the system is expressed within the framework of self-consistent field theory/density functional theory (SCFT/DFT) with interaction parameters quantifying the affinities between the blocks and particles. These parameters are denoted using $\chi_{AB}N$ and $\chi_{iP}N$ (i = A or B), where χ_{AB} is a binary interaction potential of the Flory-Huggins type between dissimilar monomers and N is the total number of monomers per chain. The quantity χ_{AB} is positive and describes the degree of incompatibility (immiscibility) of the two blocks of the BCP. In this study, we have assumed typical ranges for this interaction parameter in the five target systems (described below) that were examined using SCFT/DFT simulations; *i.e.*, $\chi_{AB}N \in [8, 28]$ in dimensionless units.[17, 20, 21, 23, 24, 32, 36, 43, 73-77] The interaction

parameters between the particles and blocks, $\chi_{iP}N$, are assumed to be short-ranged and of the Flory-Huggins type; i.e., negative when the particles favor a particular block, and positive when they disfavor a block. This type of short-range interaction potential has been assumed in prior dissipative particle dynamics studies of charged polymer membranes (*e.g.*, Wu *et al*.[78]) where the effects of atomistic potentials, such as Lennard-Jones and Coulombic, are coarse-grained into Flory-Huggins type of mesoscopic interaction parameters. Hence the interactions of charged particles on diblock film morphology are primarily steric (excluded volume) and energetic (particle surface interactions with neighboring chain segments), both being short-ranged interactions at the mesoscale. Hence, modeling the particle interactions using Flory-Huggins type parameters should provide a reasonable estimation of these interactions for the types of block copolymers used for nanofiltration membranes, where charge susceptible polymer backbone chains is undesirable. The values of the $\chi_{iP}N$ assumed for the target systems are presented in Table 2-1. These values were chosen based on those assumed by Zhu *et al.*[43]

We chose five target systems to study in the 3-dimensional simulations, with the corresponding interaction parameter values defined in Table 2-1. The first of these corresponds to the case examined in two dimensions by Zhu *et al.*,[43] that of neutral, end-tethered nanoparticles (ABP-N), which can be used to validate our 3-d simulations and to determine differences between these and the 2-d simulations of Zhu *et al.* We also examined the following four cases: 1.) particles tethered to the end of the B-block which disfavor the A-block and favor the B-block (ABP-AP); 2.) particles tethered to the end of

the B-block which disfavor the B-block and favor the A-block (ABP-BP); 3.) neutral particles tethered between the two blocks (APB-N); and 4.) particles tethered between the two blocks that disfavor the A-block and favor the B-block (APB-AP). (Note that APB-BP was not examined since it is symmetric with the APB-AP case.) These systems were targeted because together they describe all combinations of charged-species interactions with the possible blocks of the BCP.

Table 2-1. Interaction parameters between blocks and particles for the target systems.

System	ABP-N	ABP-AP	ABP-BP	APB-N	APB-AP
$\chi_{AP}N$	0.0	30.0	-30.0	0.0	30.0
$\chi_{BP}N$	0.0	-30.0	30.0	0.0	-30.0

The radius of a spherical hard particle, R_P, is set to $0.33\,R_g$, where R_g is the unperturbed mean-square radius of gyration of the copolymer chain. (This value was chosen since it is the lowest value of this parameter examined by Zhu *et al.*, where the various regions of the phase diagrams are the widest—see Fig. 3 of Zhu *et al.*)[43] For a given system volume, V, the variable f denotes the overall volume fraction of the AB copolymer chain, and f_P represents the overall particle volume fraction. According to the assigned value of R_P ($0.33R_g$), f_P=0.035. We denote as f_A and f_B the volume fractions of the A and B blocks of the polymer chain. Thus we have $f(f_A + f_B) + f_P = 1.0$.

In the framework of the SCFT/DFT method, the dimensionless free energy *F* (relative to $N_C k_B T$, where N_C is the number of chains, k_B is Boltzmann's constant, and T is the absolute temperature) of an ABP or APB system is given by the expression[16, 17, 36, 37]

$$F = -\ln\left(\frac{Q}{V}\right) + \frac{1}{V}\int d\mathbf{r}\Big[\chi_{AB}N\phi_A(\mathbf{r})\phi_B(\mathbf{r}) + \chi_{AP}N\phi_A(\mathbf{r})\phi_P(\mathbf{r}) + \chi_{BP}N\phi_B(\mathbf{r})\phi_P(\mathbf{r}) - w_A(\mathbf{r})\phi_A(\mathbf{r}) - w_B(\mathbf{r})\phi_B(\mathbf{r}) - w_P(\mathbf{r})\rho_P(\mathbf{r}) - \xi(\mathbf{r})\big(1-\phi_A(\mathbf{r})-\phi_B(\mathbf{r})-\phi_P(\mathbf{r})\big) + \rho_P(\mathbf{r})\psi_{HS}\big(\bar{\phi}_P(\mathbf{r})\big)\Big] \quad (2.1)$$

Here $\phi_A(\mathbf{r})$, $\phi_B(\mathbf{r})$, and $\phi_P(\mathbf{r})$ are the local volume fractions of the A-block, B-block, and the particles. Also, $\xi(\mathbf{r})$ is the Lagrange multiplier that is used to ensure the incompressibility condition, $\chi_{ij}N$ quantifies the interaction between components *i* and *j*, and $\rho_P(\mathbf{r})$ is the distribution of particle centers. The local particle volume fraction, $\phi_P(\mathbf{r})$, is expressed as

$$\phi_P(\mathbf{r}) = \frac{1-f}{V_R}\int_{|\mathbf{r}'|<R_P} d\mathbf{r}'\,\rho_P(\mathbf{r}+\mathbf{r}') \quad (2.2)$$

and the weighted nonlocal volume fraction of particles, $\bar{\phi}_P(\mathbf{r})$, is given by

$$\bar{\phi}_P(\mathbf{r}) = \frac{1-f}{V_{2R}}\int_{|\mathbf{r}'|<2R_P} d\mathbf{r}'\,\rho_P(\mathbf{r}+\mathbf{r}') \quad (2.3)$$

In the above expressions, V_R is the volume of a sphere with radius R_P, and V_{2R} is the volume of a sphere with radius $2R_P$. ψ_{HS} quantifies the steric energy of the particles according to a modified Carnahan-Starling equation for a hard-sphere fluid,[79]

$$\psi_{HS}\left(\bar{\phi}_P\right) = \frac{4\bar{\phi}_P(\mathbf{r}) - 3\bar{\phi}_P(\mathbf{r})}{\left(1-\bar{\phi}_P(\mathbf{r})\right)^2} \quad (2.4)$$

The hard-sphere fluid described by this equation is rather limited in scope, primarily being limited to solid particles with very little surface flexibility, such as metallic nanoparticles which were investigated in previous work.[41, 43] There are other potentials that could be used in a similar treatment, such as potentials for core-shell

nanoparticles,[80] but care needs to be exercised for these soft particle systems with respect to the surface integrations, discussed below.

The symbol Q in Eq. (2.1) is the system partition of the entire chain, including the particle, and is defined as

$$Q = \int d\mathbf{r}\, q(\mathbf{r},s) q^{+}(\mathbf{r},s) \tag{2.5}$$

where $q(\mathbf{r},s)$ and $q^{+}(\mathbf{r},s)$ are the forward and backward propagators, which represent the probabilities of finding a segment s at position $\mathbf{r}$, with the particle viewed as an additional chain segment. This is slightly different than the approach of Ginzburg,[55] who separated the contribution of the grafted particles to the overall partition function since, in that work, the particles were grafted onto oligomeric ligands and not the polymer chains. The propagators are introduced according to a Markov process, and satisfy the modified diffusion equations[38]

$$\frac{\partial}{\partial s} q(\mathbf{r},s) = \nabla^2 q(\mathbf{r},s) - w_i q(\mathbf{r},s) \tag{2.6}$$

$$\frac{\partial}{\partial s} q^{+}(\mathbf{r},s) = -\nabla^2 q^{+}(\mathbf{r},s) + w_i q^{+}(\mathbf{r},s) \tag{2.7}$$

The w_i in Eq. (2.1) is the self-consistent field potential of component i. In Eqs. (2.6) and (2.7), this quantity is w_A, if $0 < s < f \cdot f_A$, and w_B, if $f \cdot f_A < s < f$. The initial condition on the forward propagator, $q(s,\mathbf{r})$, is $q(0,\mathbf{r}) = 1$ for both the ABP and APB systems. The initial condition on the backward propagator, $q^{+}(s,\mathbf{r})$, is $q^{+}(f,\mathbf{r}) = \int d\mathbf{n} \exp\left(-w_p(\mathbf{r} + R_P\mathbf{n})\right)$ for the ABP system, while it is $q^{+}(f,\mathbf{r}) = 1$ for the APB system. Note the implication that the particles are firmly grafted onto the polymer chains;

i.e., they are effectively constrained to the role of an additional segment of the overall chain in this work, or a ligand in previous work.[55] A particle will at least partially occupy a number of adjacent simulation cells, and it is hence necessary to consider the orientation of the tethering point at the particle surface. The symbol **n** denotes a unit vector, which specifies the direction from the surface of a particle to its adjacent segment of the copolymer chain. A surface integral thus quantifies an orientational probability of the tethering location. The forward and backward propagators are then determined using Eqs. (2.6) and (2.7).

Minimizing the free energy of Eq.(2.1) with respect to the system variables $w_A(\mathbf{r})$, $w_B(\mathbf{r})$, $w_P(\mathbf{r})$, $\phi_A(\mathbf{r})$, $\phi_B(\mathbf{r})$, $\rho_P(\mathbf{r})$, and $\xi(\mathbf{r})$ yields the mean-field equations

$$\phi_A(\mathbf{r}) = \frac{V}{Q}\int_0^{f\cdot f_A} q(\mathbf{r},s)q^+(\mathbf{r},s)\,ds \tag{2.8}$$

$$\phi_B(\mathbf{r}) = \frac{V}{Q}\int_{f\cdot f_A}^{f} q(\mathbf{r},s)q^+(\mathbf{r},s)\,ds \tag{2.9}$$

$$\rho_P(\mathbf{r}) = \frac{V}{Q}\exp\left(-w_P(\mathbf{r})\right)\int q(\mathbf{r}+\mathbf{n}R_P,\, f)\,d\mathbf{n} \quad \texttt{(ABP)} \tag{2.10}$$

$$\rho_P(\mathbf{r}) = \frac{V}{Q}\exp\left(-w_P(\mathbf{r})\right)\int q(\mathbf{r}+\mathbf{n}R_P,\, f\cdot f_A)\, q\left(\mathbf{r}+\mathbf{n}R_P,\, f\cdot(1-f_A)\right)d\mathbf{n} \quad \text{(APB)} \tag{2.11}$$

$$w_A(\mathbf{r}) = \chi_{AB}N\phi_B(\mathbf{r}) + \chi_{AP}N\phi_P(\mathbf{r}) + \xi(\mathbf{r}) \tag{2.12}$$

$$w_B(\mathbf{r}) = \chi_{AB}N\phi_A(\mathbf{r}) + \chi_{BP}N\phi_P(\mathbf{r}) + \xi(\mathbf{r}) \tag{2.13}$$

$$w_P(\mathbf{r}) = \psi_{HS}\left(\bar{\phi}_P(\mathbf{r})\right) + \frac{1-f}{V_{2R}}\int_{|\mathbf{r}'|<2R_P} \rho_P(\mathbf{r}+\mathbf{r}')\psi'\left(\bar{\phi}_P(\mathbf{r}+\mathbf{r}')\right)d\mathbf{r}' + \frac{1-f}{V_R}\int_{|\mathbf{r}'|<R_P}\left[\chi_{AP}N\phi_A(\mathbf{r}+\mathbf{r}') + \chi_{BP}N\phi_B(\mathbf{r}+\mathbf{r}') + \xi(\mathbf{r}+\mathbf{r}')\right]d\mathbf{r}' \quad (2.14)$$

$$\phi_A(\mathbf{r}) + \phi_B(\mathbf{r}) + \phi_P(\mathbf{r}) = 1.0 \quad (2.15)$$

where

$$\psi'_{HS} = \frac{d\psi_{HS}}{d\bar{\phi}_P(\mathbf{r})} \quad (2.16)$$

We used the Alternating Direction Implicit Method with periodic boundary conditions in three dimensions to solve the SCFT/DFT equations.[81-83] The calculation results were used for the combinatorial screening of new mesophases in BCP-NP systems. A simulation began with setting the initial values of $\phi_A(\mathbf{r})$ and $\phi_B(\mathbf{r})$ according to the Gaussian distribution, while the initial value for the particle center distribution function, $\rho_P(\mathbf{r})$, was uniform and the initial Lagrange multiplier $\xi(\mathbf{r})$ was set to the null value. Next, calculations were performed of the particle volume fraction $\phi_P(\mathbf{r})$ via Eq. (2.2), the weighted non-local volume fraction $\bar{\phi}_P(\mathbf{r})$from Eq. (2.3), and the self-consistent field potential fields $w_A(\mathbf{r})$, $w_B(\mathbf{r})$, $w_P(\mathbf{r})$ from Eqs. (2.12)-(2.14). The propagators $q(s,\mathbf{r})$ and $q^+(s,\mathbf{r})$ could then be determined, which were used to calculate the copolymer chain partition function Q from Eq. (2.5). The next step evaluated the local block volume fractions $\phi_A(\mathbf{r})$ and $\phi_B(\mathbf{r})$ using Eqs. (2.8) and (2.9), while the particle volume fraction $\phi_P(\mathbf{r})$ and the weighted non-local volume fraction $\overline{\phi}_P(\mathbf{r})$ were determined using Eqs. (2.2) and (2.3) after evaluating $\rho_P(\mathbf{r})$ using Eqs. (2.10) and (2.11). The surface integrals in Eqs. (2.10) and (2.11) were approximated with sufficient accuracy using the mean-

value theorem, $\int f(\mathbf{n})\, d\mathbf{n} = \bar{f} \cdot S$, where S is the area of the surface of integration and $\bar{f}$ is the mean value of $f(\mathbf{n})$ over the surface. surface. In the present case, $f(\mathbf{n})$ is given by the local particle density function. Since a particle center is located at the center of a cell, it was assumed that the surface area of the particle in each adjacent cell had a common value. In this circumstance, an average particle density can be calculated using the simulated value in each cell, which can then be multiplied by the total surface area of the particle, $4\pi R_p^2$. This calculation was tested using an independent code that calculated the local particle densities in adjacent cells based on a randomly-generated distribution with explicit area counting in each cell. The two methods agreed with each other within 5% of the total area in all cases. The Lagrange multiplier $\xi(\mathbf{r})$ was calculated according to Eqs. (2.12) and (2.13) under the incompressibility constraint of Eq. (2.15). Finally, the fields $w_A(\mathbf{r})$, $w_B(\mathbf{r})$, $w_P(\mathbf{r})$, and $\xi(\mathbf{r})$ were updated using a simple mixing method and the procedure was iterated until convergence was achieved.[16, 83] The calculations were carried out until the self-consistent field potential differences between two consecutive iterations were smaller than 10^{-5}, and the incompressibility condition was satisfied.[42, 43, 73]

The calculation box size must be determined in correspondence with the natural periodic length of the system morphology, especially in the transition regions between lamellar, spherical, and cylindrical structures. We performed verifications typically using twelve different box sizes varying from about 4.6 R_g to 6.9 R_g (from $32 \times 32 \times 32$ to $48 \times 48 \times 48$ cell numbers) with cell cubes of dimension 0.144 $R_g$with 200 segments of a Gaussian chain. We used different initial conditions to decide which morphology was

the most stable by comparing their free energies.[17] We varied f_A and $\chi_{AB}N$ systematically to construct phase diagrams for the target systems in Table 2-1 in order to determine the most promising morphologies for nanofiltration applications and the strategies (*i.e.*, parameter mappings) required to generate them. Each phase diagram presented above consists of results of 3-d simulations covering 91 distinct points in a representative range of parameter space, $(f_A\,, \chi_{AB}N)$, optimizing box size as necessary.

2.2 Results and Discussion

In each of the five target systems, the cylinder, lamellar, and spherical morphologies were the most stable ordered structures formed during the self-assembly process. The particles were generally distributed unequally in the two block copolymer domains, and often agglomerated into distinct particle-dense regions of the self-assembled structures, as described in Section 2.2.3.

2.2.1 Phase diagram of end-tethered particle systems

We examined three separate cases of end-tethered particles. In each case, the particle was tethered to the free end of the B-block of the copolymer. The three systems studied correspond to cases where the particle is neutral to both blocks of the copolymer (ABP-N), where it disfavors the A-block but favors the B-block (ABP-AP), and vice versa (ABP-BP). We will discuss each of these three cases in the following subsections.

2.2.1.1 The neutral particle system (ABP-N)

The ABP-N system of end-tethered nanoparticles was first studied using 2-dimensional SCFT/DFT simulations by Zhu *et al.*,[43] for which $\chi_{AP}N = \chi_{BP}N = 0$. We performed 3-d simulations of the same system at $R_P/R_g = 0.33$ over similar ranges of $\chi_{AB}N$ ($\in$ [11,28]) and f_A ($\in$ [0.2,0.8]) as assumed by Zhu *et al.* Figure 2-1 presents the phase diagram of these 3-d simulations, which is similar to the phase diagram of stable, 2-d morphologies of Zhu *et al.*; however, the phase diagram for our system is shifted to lower values of $\chi_{AB}N$ than that of Zhu *et al.* for the appearance of the ordered regions (*cf.* Figure 2-1, where $\chi_{AB}N \approx 12.0$ at the ordered-phase critical point, with Figure 2-2 of Zhu *et al.*, where $\chi_{AB}N \approx 15.0$). Presumably, this is due to the 2-d confinement effect: the confinement is known to increase the miscibility of polymer blends. Therefore, the critical point of their 2-d simulation is much higher than our 3-d simulations.[84] The particle volume fractions are also different between our 3-d and their 2-d simulations: as mentioned above, we chose to use the same value for the ratio $R_P/R_g = 0.33$ as Zhu *et al.*; however, this corresponds to a value of $f_P = 0.098$ in the 2-d simulations, whereas it is 0.035 in the 3-d simulations. This difference impacts the values of the particle surface and volume integrations appearing in Eqs. (2.10), (2.11) and (2.14). Therefore, our critical point of the ordered-phase transition is closer to that of the pure diblock copolymer, which is known to occur at a value of $\chi_{AB}N \approx 10.0$.[20]

As evident from Figure 2-1, only disordered morphologies (D) exist for $\chi_{AB}N < 12.0$. For higher values of this parameter, one also finds five distinct ordered morphologies depending on the volume fraction of the A-block. At relatively low values

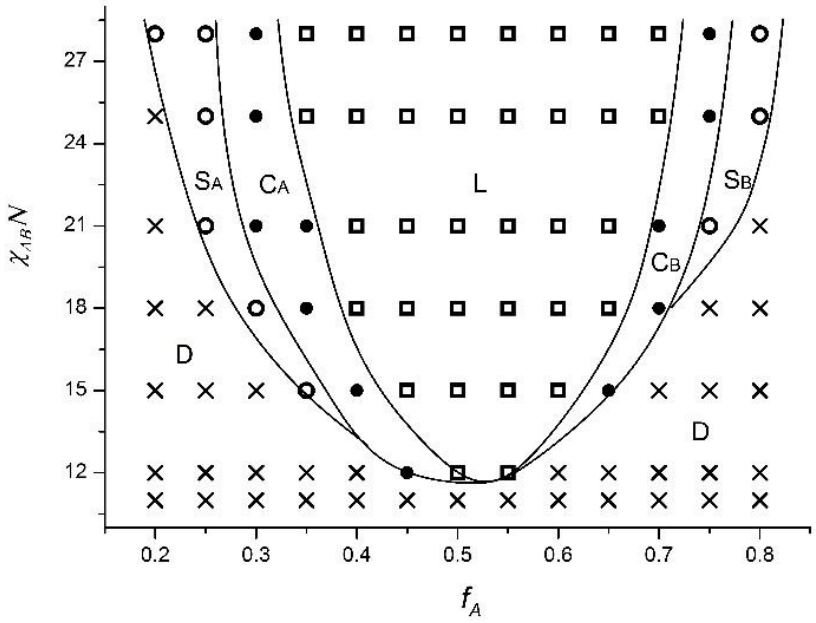

Figure 2-1. Morphological phase diagram of the ABP-N system, as defined in Table 2-1. The different morphological regions are denoted as lamellae (L), hexagonally packed cylinders formed by the A block (C_A), cylinders formed by the B block (C_B), nanospheres formed by the A block (S_A), nanospheres formed by the B block (S_B), and disordered phases (D).

of f_A, there exists a morphology composed of A-rich cylinders (C_A) that are hexagonally packed within the B-dominated matrix region. Conversely, at relatively high values of f_A, the hexagonal cylinders are rich in the B-block of the copolymer (C_B), surrounded by an A-rich matrix phase. Typical values of the local volume block fraction of the dominant cylinder component typically reach 0.95. For intermediate values of f_A, we observe the usual lamellar region (L) where the segregation of the blocks of the copolymer is extreme, with alternating layers typically possessing a local volume fraction of the dominate block in the range of $[0.9, 0.95]$. Two spherical morphologies, S_A and S_B, are formed immediately outside of the C_A and C_B regions, at slightly lower and higher values

of f_A, respectively. These morphologies are comprised of nanospheres arranged on body-centered cubic lattices, which are either A-rich or B-rich, depending on the value of f_A.

The spherical morphologies described above were not found in the 2-d simulations of Zhu *et al.* at this value of $R_P/R_g = 0.33$—see Fig. 2 of Zhu 2010.[43] The reason for this is most likely that the 2-d simulations simply were not able to distinguish between the spherical and cylindrical morphologies, and hence the C_A region of the 2-d simulations corresponds almost exactly to the combined C_A and S_A regions of the 3-d simulations, and likewise for C_B. However, Zhu *et al.* stated that they performed a few sample 3-d simulations for this system for R_P/R_g values in the neighborhood of 0.33, but noticed no differences between their 2-d and 3-d simulation phase diagrams. Therefore, we investigated these regions of our phase diagram very carefully to ascertain the most stable morphology by varying the simulation box size from 4.6×4.6×4.6 to 6.9×6.9×6.9R_g^3 (corresponding to 30×30×30 to 48×48×48 cells) and initial conditions (covering metastable morphologies of disordered, cylindrical, and spherical states formed from previously converged solutions). Zhu *et al.* stated that they examined box sizes of 48×48×48, whereas most of our minimum free energy states were determined with box sizes in the neighborhood of 33×33×33 or 42×42×42. For a box size of 48×48×48, we found free energy values significantly higher than those for smaller box sizes, and morphologies that were either perforated lamellar[20, 73] or gyroidal,[20, 74, 75] depending on the state point. The accuracy of the particle surface integration in our model is limited by the lattice size, which might cause the free energy comparisons between the various morphologies at specific state points in these narrow regions of phase space to contain

numerical approximation errors; however, the particular morphology we report at each state point corresponds to the one with the absolute lowest value of the free energy as calculated in our simulations. Regardless of any possible approximation error, we believe that these more complex morphologies, if occurring at all, only exist in such narrow regions of state space (at least at the particle size examined herein) as to be practically inaccessible. Specifically, the difference between two simulation state points is 0.05 f_A at the same value of $\chi_{AB}N$, whereas the region where the gyroidal morphology is present is known to be quite narrow (< 0.05), and the cylinder or lamellar regions are also known to overlap partially the gyroidal region (which is only metastable in these overlapping regimes).[83] These reasons make it is difficult to decide the exact gyroidal region of global stability in this method, assuming that it exists. Note that at higher values of R_P/R_g (0.45), Zhu *et al.* did observe spherical morphologies of the sort noted above. (For the value of $R_P/R_g = 0.45$, the corresponding value of f_P is 0.0835.)

It is instructive to examine the behavior of the internal energy and entropy of the stable morphologies within the various regions of the phase diagram—see Figure 2-2. For this purpose, the free energy of Eq. (2.1) is split into components arising from energetic effects (the first three terms within the integral), which we assign the symbol U and entropic effects (all other terms), which we define as S, according to the standard Legendre transformation, $F = U - TS$. Each of these quantities is rendered dimensionless in the same way as the free energy of Eq.(2.1), with U relative $N_C k_B T$ and S relative to $N_C k_B$. At $\chi_{AB}N = 11$, the system is always in the disordered regime regardless of the value of f_A. The energetic contribution to the free energy displays a

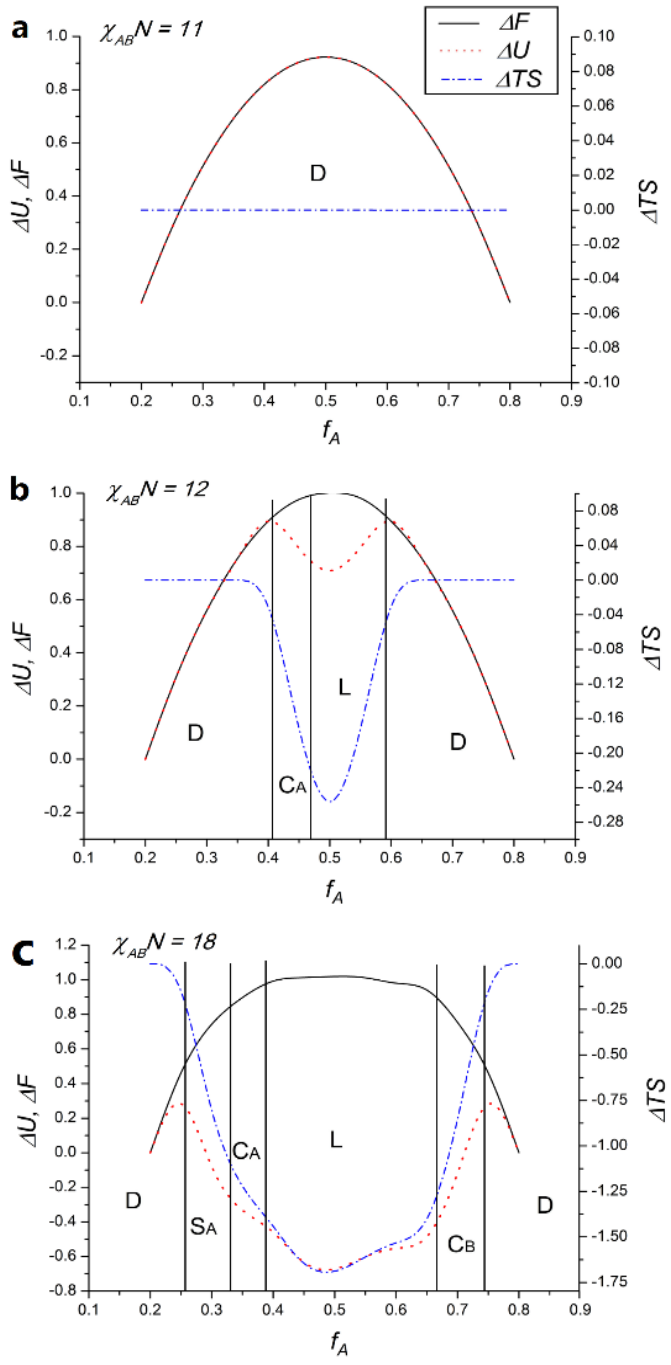

Figure 2-2. Energetic and entropic contributions to the free energy at various values of $\chi_{AB}N$, as noted in the legends. ΔU and $\Delta(TS)$ are calculated relative to their values at $f_A = 0.2$ at the respective value of $\chi_{AB}N$. The vertical lines denote the approximate phase boundaries of the various morphologies.

maximum at roughly $f_A \approx 0.5$. (This maximum occurs slightly less than $f_A = 0.5$ because of the non-zero value of the particle volume fraction, $f_P = 0.035$.) The energetic contribution for the ABP-N system varies as the integral of $\chi_{AB}N\phi_A\phi_B \approx \chi_{AB}N\phi_A(1 - \phi_A)$ since $\phi_P \ll 1$, so in a disordered state, where the local concentration of each block is roughly proportional to its relative fractional chain length, the maximum of ΔU in the vicinity of $f_A \approx 0.5$ is expected. The entropic contribution remains null, independent of the value of f_A, which is a consequence of the assumption of statistical equivalence of the A and B segments (sometimes referred to as "conformational symmetry"). Since the A and B segments are indistinguishable from each other in the model, as long as the overall chain length remains the same there is no configurational entropic effect associated with varying the relative lengths of the blocks. With $\Delta S = 0$, the free energy change with increasing f_A is equivalent to ΔU. Although the change in entropy (relative to its value at $f_A = 0.2$) is $\Delta S = 0$ regardless of f_A, its absolute value is not zero, and configurational entropy is the dominant driving force in maintaining the disordered state of the system in spite of the non-zero value of $\chi_{AB}N = 11.0$.

When the interaction parameter is increased to $\chi_{AB}N = 12.0$, as in Figure 2-2b, ordered phases develop in the vicinity of $f_A \approx 0.5$—see Figure 2-1. The increased interaction energy, *U*, has grown to a magnitude where it can compete with the randomizing entropic potential, *S*. At small and large values of f_A, the entropy can still overcome the energetics of the repulsive forces between the A and B segments since the number of interactions is fewer than when the blocks have an equal number of segments. In these regions, the phase is disordered and the energy and entropy display the same

qualitative behavior as for the case of $\chi_{AB}N = 11$. For $f_A \approx 0.5$, however, the energy can be reduced by phase segregating the A and B segments, as mandated by the parabolic expression $\chi_{AB}N\phi_A(1-\phi_A)$, which nears global minima as $\phi_A \to 0, 1$. This segregation results in a large decrease in the configurational entropy due to packing frustration as the chains adopt unnatural configurations, which drives up the free energy. The chain configurations are compressed and packed within the minor phase domains, whereas the chains comprising the matrix phase are stretched in accordance with the constant density assumption. Nevertheless, this randomizing driving force is not severe enough to overcome the energetic decrease, leading to a stable ordered phase. Phases of cylinders or lamellae are formed, depending on the relative block lengths (*i.e.*, the value of f_A), with the junctures of the two blocks and particles primarily located at the interfaces. The surface area of these interfaces is determined by a delicate balance between the entropic packing frustration within the structure and the necessity of minimizing the contact area between the A and B segments. The exact morphology (cylinders, lamellae, or, at higher χ_{AB}, spheres) that appears is determined largely by this balance between the packing volume of the structure and its interfacial surface area. As the relative lengths of the blocks change (varying f_A), this balance can change drastically, hence requiring more numerous but smaller domains (higher surface area to volume ratio), vice versa, or, in the most drastic cases, a change in the morphology of the system to accommodate it.

When the interaction parameter is increased to $\chi_{AB}N = 18$, there are five distinct morphological regimes: D, S_A, C_A, L, C_B and D, moving from left to right in Figure 2-2c. At this value of $\chi_{AB}N$, the energetic contribution to the free energy is comparable to that

of the entropy, and more morphologies arise to accommodate the required balance between interfacial surface area and packing volume. Furthermore, these structures appear for smaller minority chain lengths (*i.e.*, smaller and larger values of f_A) than for the case of $\chi_{AB}N = 12$ since the relative contribution of the entropy to the free energy has decreased.

2.2.1.2 Interacting particle systems (ABP-AP and ABP-BP)

Zhu *et al.*[43] also examined a 2-dimensional system wherein particles tethered to the end of one of the blocks were disfavored equally by both of the blocks of the copolymer. Here we study the case where the end-tethered particle favors the B block, to which it is attached, while disfavoring the A block (ABP-AP) and the inverse case (ABP-BP), as displayed in Table 2-1. We retained the particle radius at $R_P/R_g = 0.33$.

In the case of the ABP-AP system, we set the particle-block interaction parameters at values of $\chi_{AP}N$ = 30 and $\chi_{BP}N = -30$, such that the particle has an affinity to the B block to which it is tethered and a revulsion to the A block. Since the particles are attached to the B blocks, we expect that the phase diagram for this system will qualitatively resemble that of the ABP-N system, but drive the particle distributions even more prominently into the domains of the self-assembled structures that are dominated by the B block. Consequently, one could possibly tailor in a specific volume fraction of particles within the B-rich regions of the morphologies by fine-tuning the affinity of the particles to the B block of the copolymer, as discussed in Section 2.2.3.

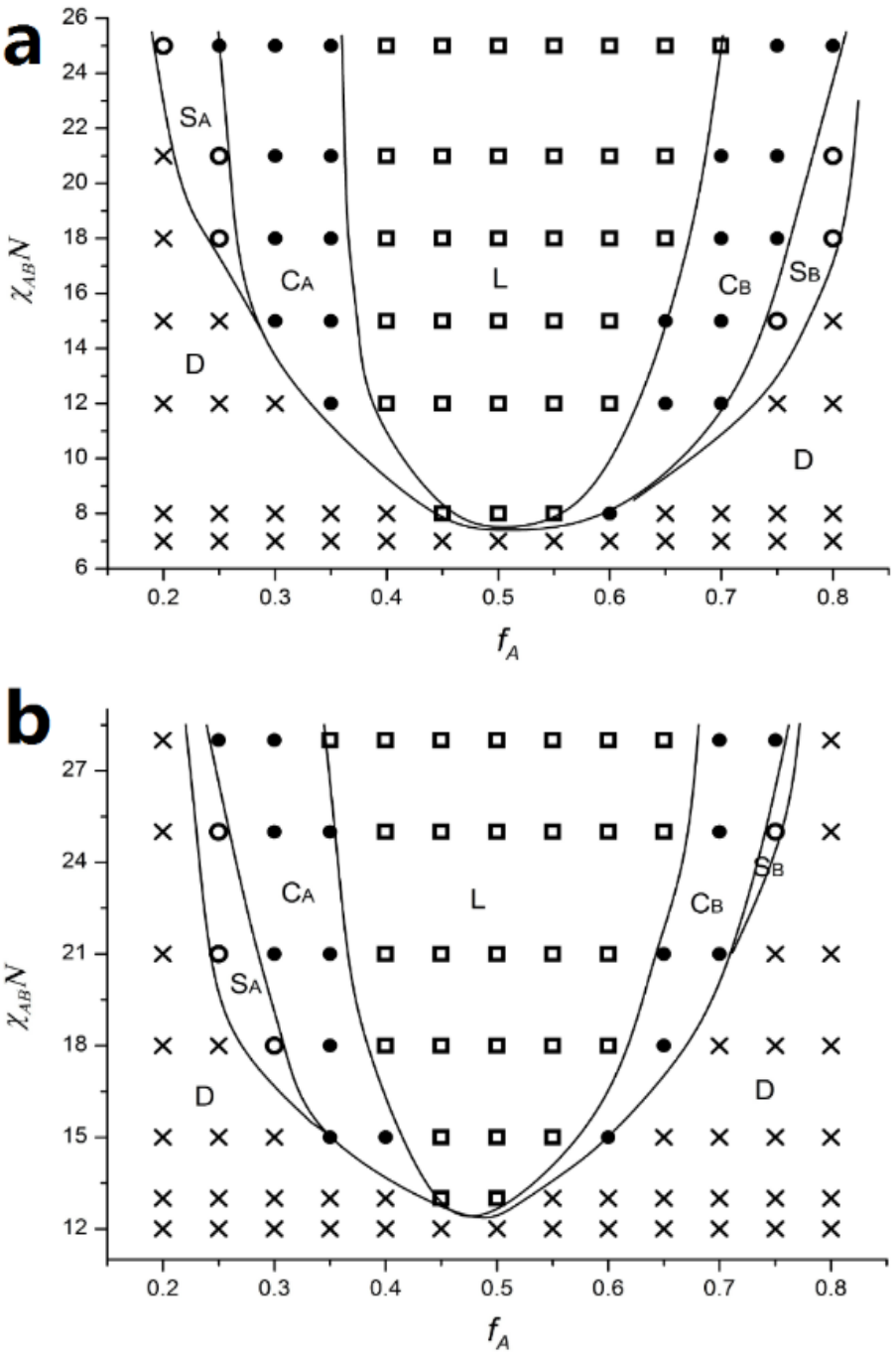

Figure 2-3. a.) Morphological phase diagram of the ABP-AP system with favorable BP interactions and unfavorable AP interactions. b.) Phase diagram of the ABP-BP system with favorable AP interactions and unfavorable BP interactions.

The phase diagram for the ABP-AP system is presented in Figure 2-3a. For $\chi_{AB}N <$ 8, only the disordered phase was stable as the order-inducing energetic contribution of the repulsive A-B block interactions was not sufficient to overcome the randomizing entropic contributions to the free energy. An evident change from the ABP-N system of Figure 2-1 is that the ordered-phase critical point in the ABP-AP system has been shifted downward on the $\chi_{AB}N$ -axis relative to that of the ABP-N copolymer. Because the $\chi_{AP}N$ and $\chi_{BP}N$ parameters are no longer zero, two additional terms in Eq. (2.1) are contributing to the internal energy of the system. Although the terms $\chi_{iP}N\phi_i\phi_P$ can significantly impact the free energy in localized domains, which are relatively rich in particles, they do not contribute substantially to the overall free energy of the system since $f_P \ll 1.0$. Nevertheless, the primary driver of this downward shift is the affinity of the B segments for the particles, which induces the B segments to cluster and compress around the particles, thereby reducing the number density of particles and B segments directly exposed to the A blocks. This results in a lower overall internal energy contribution to the total free energy, but also relieves some of the entropic packing stress, thus allowing ordered phase segregation at lower values of $\chi_{AB}N$ than in the ABP-N system. Another key change evident in Figure 2-3a from the ABP-N phase diagram of Figure 2-1 is that the C_A and C_B regions have widened whereas the lamellar region has shrunk, which is likely due to the lowering of the internal energy by the negative BP interactions (recall that $\chi_{BP}N\phi_B\phi_P$ is a negative quantity), thus shifting the ratio of interfacial area to packing volume higher.

The corresponding phase diagram for the ABP-BP system is displayed as Figure 2-3b, where the particle-block interaction parameters were set at $\chi_{AP}N = -30$ and $\chi_{BP}N$=30.0. In the ABP-BP case, it is evident that the ordered-phase critical point has shifted upward. Now that the particles favor the A segments, rather than the B blocks to which they are tethered, a huge entropic penalty must be overcome to form an ordered phase since the particles preferentially tend to concentrate at the interfaces where they can be near to the A segments, thus forcing the B blocks to assume loop and hairpin-like configurations, or to stretch across the dimensions of the domain. Consequently, the overall contribution of the internal energy to the free energy must be significantly larger than in the neutral particle (ABP-N) case to overcome the large reduction in short-range configurational entropy of the B blocks—refer to Figure 2-2, which is qualitatively similar to the present case. The morphological phase diagram of Fig. 3b resembles more that of the neutral particle case of ABP-N (Figure 2-1) than that of the ABP-AP case (Figure 2-3a). As in the ABP-BP case, the phase diagram exhibits an expanded C_A region, while the C_B region is relatively narrow. The A-rich cylinder morphology of the C_A region is stabilized by the favorable AP interactions.

2.2.2 Phase diagram of center-tethered particle systems (APB-N and APB-AP)

We simulated two systems in which the interacting particles were located at the juncture of the diblock copolymer, between the A and B blocks. The first case is that of a particle that is neutral to both blocks (APB-N), and the second where the particle favors the B segments and disfavors the A segments (APB-AP). Note that the second case is

statistically equivalent to that in which the particle favors A and disfavors B. Since the particles are tethered between the two copolymer blocks, it seems natural to expect that one might find many interesting morphologies here in which the particles are heavily concentrated at the interfaces between the A-rich and B-rich domains.

The morphological phase diagram of the APB-N system is presented in Figure 2-4a, where $\chi_{AP}N = \chi_{BP}N = 0.0$. Because the particle is neutral to both A and B segments, the phase envelope is symmetric about $f_A = 0.5$ since there is no physical difference in this model between A and B blocks, other than through the dimensionless interaction parameters. Again there appear six general types of morphologies, corresponding to disordered domains, A-rich and B-rich cylinders, A-rich and B-rich spheres, and lamellae. The morphological phase diagram for the APB-AP system (center-tethered particle for $\chi_{AP}N = 30.0$ and $\chi_{BP}N = -30.0$) is depicted in Figure 2-4b. Compared to the APB-N system, the C_A region of the phase diagram has widened whereas the C_B region has shifted to the right. In all cases, the particles are heavily dispersed within the B-rich domains of the structures, as one would expect given the high degree of affinity between the particles and the B segments—refer to section 2.2.3. (Note that this case is equivalent to the APB-BP system with the A and B blocks interchanged.)

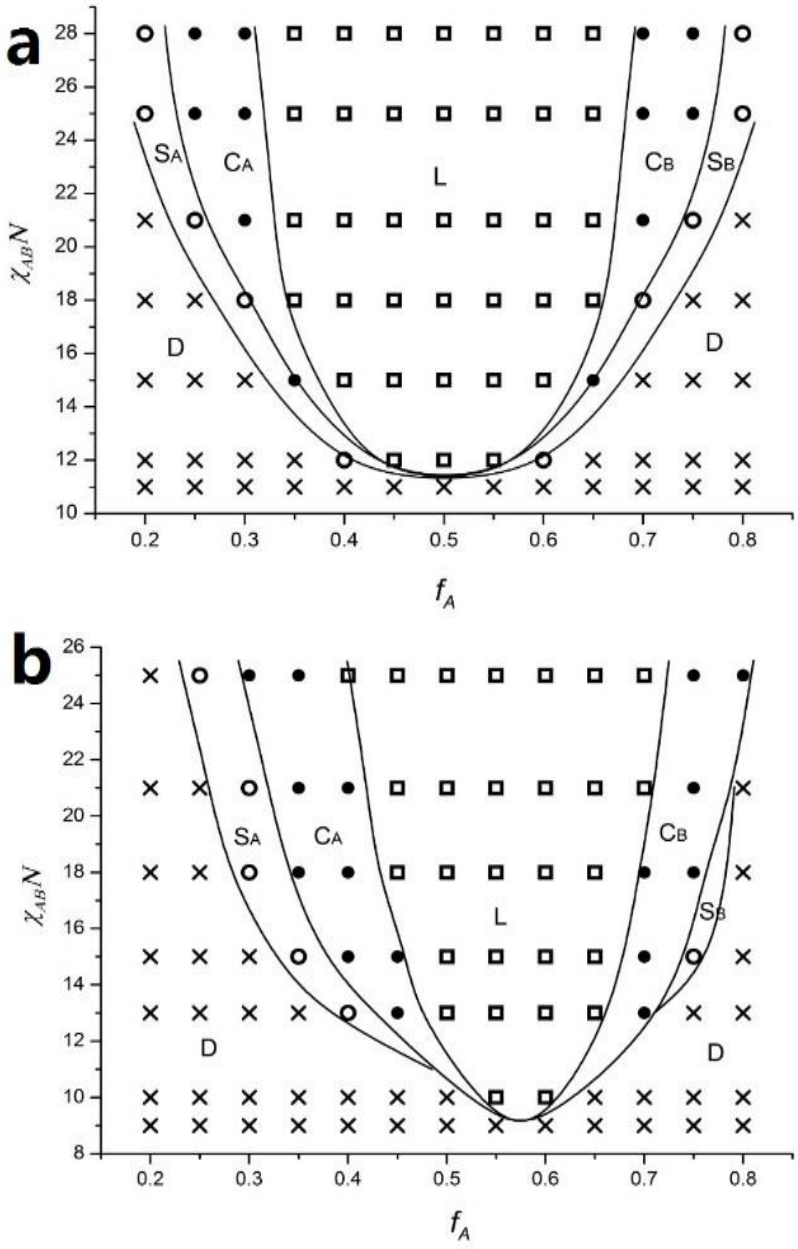

Figure 2-4. a.) Morphological phase diagram of the APB-N system in which the particle is tethered between the two blocks and is neutral to both. b.) The phase diagram of the APB-AP system where the particles favor the B blocks and disfavor the A blocks. Due to symmetry, the inverse system, APB-BP, has the same phase diagram when f_A is replaced with f_B.

2.2.3 Particle density distributions

Three types of cylinder morphologies were discovered in the 3-d simulations, each with a distinct distribution of particles within the A-block and B-block dominated domains—refer to Figure 2-5a. In reference to Figure 2-5b, c, and d, these three morphologies are as follows: (a) particle-rich matrix domains surrounding hexagonally-packed, particle-lean cylinder cores; (b) particle-rich interfaces between the cylinders of one block and the matrix formed by the other; and (c) particle-concentrated cylinder cores surrounded by a particle-depleted matrix phase with a dilute layer of screening particles at the interface. Three important factors acted concertedly to affect particle location during the self-assembly process, as well as the cylinder diameter and the length scale of the hexagonal array: (1) the location of the tethering point of the particle to the copolymer chain, (2) the particle-block interaction parameters and the block-block interaction parameter ($\chi_{ij}N$), and (3) the A-block volume fraction (f_A). The effects of these quantities on the phase diagrams of the previous sections of the self-assembled structures will be described in the following paragraphs, focusing primarily on the cylinder morphologies rather than those forming lamellae or spheres, as being of greater interest to nanofiltration applications.

With reference to Table 2-2, the values of the cylinder diameters in the C_A and C_B regions are determined based on the intersection of the ϕ_A and ϕ_B curves in Figure 2-5b, c, and d, and the packing dimensions are defined as the distance between neighboring cylinder centers. These values are critically important for steric exclusion in nanofiltration membranes. Typical values of the cylinder diameter and packing

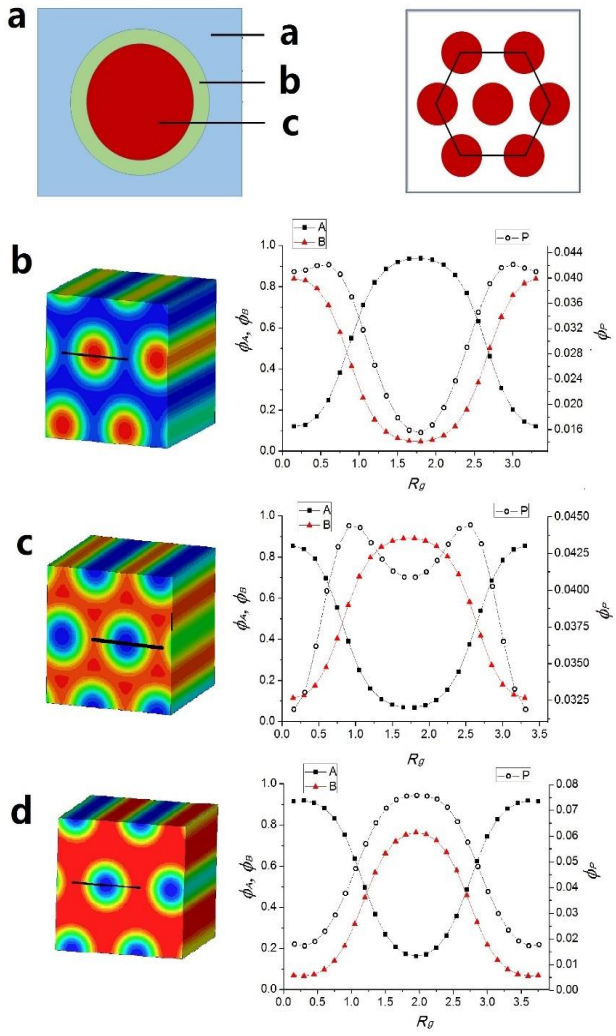

Figure 2-5. a.) Schematic diagram of possible particle-rich regions (left) and the cylinder hexagonal packing configuration (right). In the left figure, the symbols denote the following regions of the most stable, ordered cylindrical structure: polymer matrix (a), cylinder interface (b), and cylinder core (c). In the right diagram, the lengths of the black line segments denote the packing dimension. Rows b.), c.), and d.) are the example morphologies (left column) and sample distributions (right column) representing the various regions depicted in a.): b.) particles concentrated within the matrix domain (APB-AP, $f_A = 0.75$, $\chi_{AB}N = 18$); c.) particles concentrated at the interface (ABP-BP, $f_A = 0.65$, $\chi_{AB}N = 21$); and d.) particles concentrated within the cylinder cores (APB-AP, $f_A = 0.35$, $\chi_{AB}N = 18$). The block and particle volume fractions in the right column are plotted in units of R_g corresponding to the periodic spatial location along the black line in the morphological images on the left.

dimension for different values of f_A and $\chi_{ij}N$ are displayed in Table 2-2. The results are as one would intuitively expect: as $\chi_{AB}N$ is increased at fixed f_A, the diameter of the cylinders and the packing dimension increase. This trend occurs because the cylinder surfaces require less curvature (*i.e.*, less surface area relative to volume) since the associated decrease in internal energy is mitigated by the increased energetics of the mismatch between the two copolymer blocks.[18, 20]. Furthermore, as f_A is increased (when $f_A < 0.5$) at fixed $\chi_{AB}N$, the diameter of the cylinders and the packing dimensions also increase. This is also intuitive since in these C_A morphologies, increasing the length of the A block increases the potential for packing frustration, which balances the energetics of the interfacial curvature.

Besides steric exclusion, an equally important factor influencing the rejection ratio of nanofiltration membranes is the charge (Donnan) exclusion. To proceed, it is necessary to set quantitative criteria as to acceptable design specifications; *i.e.*, concentration levels of particles at the interface, *etc*. This is, of course, rather arbitrary without a specific application in mind, so we set rather strict criteria and screened parameter space to identify cylindrical morphologies that possess cores with a local volume fraction of the major component of at least 0.80 while that of the minority phase is less than 0.10, as well as interfaces with local particle volume fractions that are at least 75% greater than the overall particle concentration of $f_P = 0.035$; *i.e.*, $\phi_P \approx 0.06$.

Table 2-3 displays information about each of the cylindrical morphologies observed in the simulations: the domain with the greatest concentration of particles, the average

Table 2-2. Typical values of cylinder diameters and packing dimensions. The error associated with these values is $\pm 0.14\ R_g$, which is due to the discretization of the simulation grid.

system	*diameter (R_g)*	*packing dimension (R_g)*	$\chi_{AB}N$	f_A
ABP-N	*[2.0, 2.2]*	*[4.1, 4.6]*	*21*	*[0.3, 0.35]*
	[2.0, 2.5]	*[4.1, 5.0]*	*⌈21, 25]*	*0.3*
ABP-AP	*[2.1, 2.5]*	*[4.4, 4.7]*	*25*	*[0.25, 0.35]*
	[1.8, 2.5]	*[3.0, 4.7]*	*[12, 25]*	*0.35*
ABP-BP	*[1.3, 1.8]*	*[3.0, 4.1]*	*25*	*[0.3, 0.35]*
	[1.5, 1.8]	*[3.0, 4.1]*	*[15, 25]*	*0.35*
APB-N	*[1.6, 2.1]*	*[3.1, 3.4]*	*25*	*[0.25, 0.3]*
	[1.4, 2.1]	*[3.0, 3.4]*	*[21, 25]*	*0.3*
APB-AP	*[2.4, 3.0]*	*[4.8, 5.0]*	*25*	*[0.3, 0.35]*
	[2.0, 3.0]	*[4.4, 5.0]*	*[18, 25]*	*0.35*

values of ϕ_P at the interfaces, and whether or not it is possible for the specific morphology to meet the nanofiltration (NF) membrane design criteria, as stated above.

The particles in the ABP-N system are primarily uniformly distributed within the B-rich domains for all ordered morphologies occurring within the investigated region of parameter space, $(f_A\ , \chi_{AB}N)$, which confirms the results of Zhu *et al.* at this value of $R_P/R_g = 0.33$. This is intuitively expected, since the particles do not disfavor either block, and thus effectively act as an additional non-interacting B segment at the end of B block. Consequently, there is no energetic driving force to preferentially distribute the particles non-uniformly within the A or B domains, and the particle distribution is then naturally concentrated within the B-rich domains since it is tethered to the end of this block. In the C_B region of parameter space, the particle volume fraction at the interface is approximately 0.065, and the concentrations of the A and B blocks within the cylinder cores and matrix, respectively, are approximately 0.85; hence this region of the

morphological phase diagram meets are criteria for application to nanofiltration membranes.

For the ABP-AP system, however, there is more than simply an entropic effect induced by the attachment to the B block; there is also an effect arising from the high affinity of the B segments toward the particles, which provides the segments with a strong energetic motivation to cluster around the particles, in addition to the incompatibility of the particles with the A segments. As in the ABP-N system, an acceptable particle concentration (approximately 0.075) can be achieved at the interfaces in the C_B region of parameter space; another positive improvement over the ABP-N system is that the cylinder domain regions (C_A and C_B) of the phase diagram are much wider than the previous case, allowing more flexibility in the tuning of design parameters.

In the case of the ABP-BP system, where the particles disfavor the B segments and favor the A segments, the cylinders are very diffuse, with wide interfaces. Although the particle distribution exhibits peaks in the relatively large interfacial regions, the overall magnitude of ϕ_P does not meet the stated design criterion of 0.06. Furthermore, the concentration of the respective blocks within the matrix or cylinder cores is very low, approximately 0.7.

In the APB-N system, the particles act merely as a screen to shield the A and B segments from each other. Consequently, the maximum concentration of particles occurs at the interfaces, where the particles act to screen the A and B segments from each other. Nevertheless, since the particles are neutral to both types of segments, there is a

significant concentration of particles that remain in the cylinder cores and the matrix phase, thus reducing the concentration at the interface to a value below the stated design criterion. However, increasing the degree of mismatch between the A and B segments can drive more particles to the interface, where they reduce the system energy by screening the A and B segments from each other; hence an acceptable value of ϕ_P can actually be achieved if $\chi_{AB}N$ is high enough.

The APB-AP system, in which particles disfavor the A segments and favor the B segments, provides a very wide range of possibilities for NF membrane applications. When the length of the A block is relatively small (the C_A region), A segments are predominantly located within the cylinder cores, with a high concentration of particles at the interface screening the B blocks; however, these particles are only located there because of their location along the chain (*i.e.*, tethered between the A and B blocks) simply because from the viewpoint of the A segments, the particles are energetically more unfavorable than the B segments at low values of $\chi_{AB}N$. Nevertheless, the highest particle concentration is within the matrix domain since the particles are attractive to the B segments, which thus tend to surround them. As $\chi_{AB}N$ is increased, the energetic mismatch between the A and B segments increases in magnitude relative to the mismatch between the A segments and particles ($\chi_{AP}N = 30.0$), and hence the A blocks ultimately view the particles as simply additional B segments. Hence there is a decreasing energetic tendency for the A blocks to push the particles away from the interface and into the matrix phase. At the same time, there is a lower driving force for the B blocks to pull the particles into the matrix phase since the B segments increasingly want to avoid the

interfaces where they come into close proximity with the A segments. Hence, as $\chi_{AB}N$ is increased, the natural location of the center-tethered particles concentrates them at the interface, and it indeed becomes possible to meet the stated design criteria. When the A blocks are relatively long (the C_B region), the natural tendency of the A segments to repulse the particles pushes them toward regions of high interfacial curvature, forcing the B segments into highly compacted cylinder cores. This effect is intensified as $\chi_{AB}N$ is elevated since the degree of mismatch between the A and B segments increases relative to the A-P and B-P interactions. Consequently, the particles are increasingly located at the interfaces, given their tethering location between the two blocks. In both the C_A and C_B regions, the cylinder cores and surrounding matrix are almost entirely free of the opposite segments at high values of $\chi_{AB}N$; *i.e.*, ϕ_A and ϕ_B are approximately 0.95 in their respective domains. Note that the APB-BP morphological phase diagram is simply the mirror image of the APB-AP diagram, so the stated conclusions also apply to the BCP-NP system.

In summary, the most reliable way to produce copolymer thin films with cylinders of highly concentrated particles at the interface is to have particles that possess a high affinity for the B segments while strongly disfavoring the A segments. In this case, a moderately sized domain of the phase diagram, the C_B region, is accessible to this particular morphology. Careful tuning of the relevant interaction parameters between the blocks and the particles might therefore provide a pathway to tailoring of both steric and charge screening in nanoporous copolymer membranes once the cylinder-forming block of the copolymer has been thermally or chemically degraded.

Table 2-3. The particle-rich domains for different cylindrical morphologies in BCP-NP systems and particle volume fractions at the interfaces. The matrix, interface, and cylinder core are defined in Figure 2-5a. As $\chi_{AB}N$ or f_A increases, the particle density also increases (but generally less than 0.01 in absolute value).

System	*Morphology region*	*Particle-rich domain*	*Typical value of particle density at the interface*	*Candidate for NF?*
ABP-N	C_A	*matrix*	*~0.035*	
	C_B	*cylinder core*	*~0.065*	*yes*
ABP-AP	C_A	*matrix*	*~0.040*	
	C_B	*cylinder core*	*~0.075*	*yes*
ABP-BP	C_A	*interface*	*~0.045*	
	C_B	*interface*	*~0.050*	
APB-N	C_A	*interface*	*~0.055*	*yes, if* $\chi_{AB}N \geq 28$
	C_B	*interface*	*~0.055*	*yes, if* $\chi_{AB}N \geq 28$
APB-AP	C_A	*matrix*	*~0.050*	*yes, if* $\chi_{AB}N > 21$
	C_B	*interface*	*~0.070*	*yes*

2.2.4 Critical point of the phase diagrams

It is interesting to examine the effect that particle affinity has upon the ordered-phase segregation in the ABP and APB systems. The critical point of the ordered-phase envelope is displayed as a function of different pairs of of $\chi_{AP}N$ and $\chi_{BP}N$ at $f_A \approx 0.5$ in Figure 2-6. For the ABP system (Figure 2-6a), the left most datum point corresponds to the ABP-BP system studied above, and the right most to the ABP-AP system, with the ABP-N system at the center of the profile. When the particles are highly repulsive to the B segments and highly attractive to the A segments, the critical point remains constant at a value of $\chi_{AB}N \approx 13$. In this regime, the entropically unfavorable configurations caused by the particle attraction to the A segments dominate the overall free energy, as described above. Because of this, morphologies with the desired concentration of particles at the interface of the cylinder domains cannot be achieved. As the particle interaction strength

decreases, the energetic effects begin to counteract the effect of the configurational entropy until the particles are completely neutral in the ABP-N system. Here the particles tend to agglomerate at the interface to screen the A and B segments from each other, producing a counterintuitive high concentration of particles between the cylinder cores and matrix phase. Moving further to the right in Figure 2-6a, the end-tethered particles primarily act as additional B segments, at least from the perspective of the A segments, and so the particle concentration in the A phase, whether in the cylindrical domains (C_A region) or in the matrix phase (C_B region), is exceedingly low; consequently, the particle concentration at the interface and in the B-rich domains is higher than in the neutral particle system. This increasingly high degree of segregation moving to the right in Figure 2-6a provides the driving force for the decrease in the critical point.

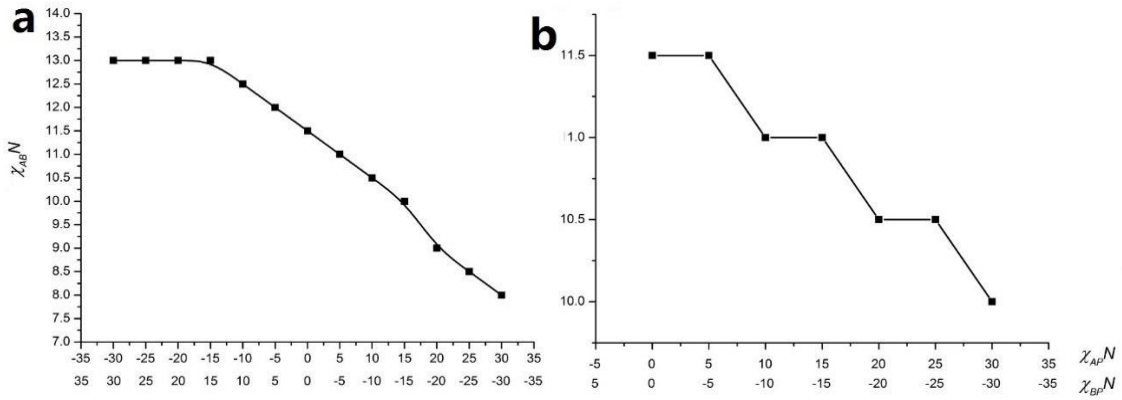

Figure 2-6. Values of $\chi_{AB}N$ of the ordered-phase critical points for diblock copolymers as functions of the particle/block interaction parameters. a.) end-tethered particles. b.) center-tethered particles. Note that the data profile should be symmetric around the point $\chi_{AP}N = \chi_{BP}N = 0$ due to the symmetry of the APB systems.

As for the APB system displayed in Figure 2-6b, the qualitative behavior displays the same trend exhibited by the ABP systems; *i.e.*, the minimum decreases with increasing

disparity between the two block-particle interaction parameters moving to the right from the neutral APB-N system. The reason for this is the same as above: the increasingly repulsive force between the A segments and the particles drives a higher degree of segregation of the particles at the cylinder interfaces and within the B-rich domains. Consequently, the APB-AP system possesses higher concentrations of particles at the interfaces than the neutral APB-N system, in general, and an increasing value of $\chi_{AP}N$ drives down the ordered-phase critical point and leads to even higher concentrations of particles at the cylinder interfaces. This type of information could be very important for initial screening of particle interaction properties for grafting onto block copolymers designed for specific applications.

Chapter 3

Simulations of Block Copolymer/Charged Particle Systems at Variable Particle Radius

This chapter is based on the published paper

"The effect of particle size on the morphology and thermodynamics of diblock copolymer/tethered-particle membranes" B. Zhang, and B.J. Edwards, *J. Chem. Ph*ys, **142**, 21, 214907 (2015)[85]

3.1 Methodology

We applied the real-space self-consistent field theory coupled with density functional theory (SCFT/DFT)[36, 37] as discussed in the Ch. 2 to simulate the BCP-NP systems studied in this chapter. In general, a suite of simulations was performed for systems of B-end-tethered (ABP) and center-tethered (APB) particles with ranges of radii ($R_P \in [0.1, 0.4\,R_g]$), volume fraction of the A segment ($f_A \in [0.20, 0.80]$), and interaction parameters ($\chi_{AP}N = \chi_{BP}N \in [0, 20]$), where $\chi_{iP}N$ is the Flory/Huggins-type interaction parameter between the particles and the *i*-th block segments multiplied by the chain length, which includes both neutral and strongly interacting particles. Exact details of the systems examined will be described below.

The overall volume fraction of the particles is determined based on the radius of the particle size being simulated as f_P = 0.0009, 0.0079, 0.026, and 0.0602 for the particle

radii of 0.1, 0.2, 0.3, and 0.4 R_g, respectively. A continuity relationship can then be used to calculate the overall volume fraction of component B: $f \cdot (f_A + f_B) + f_P = 1$.

The general procedure for solving the SCFT/DFT system of equations was described by Zhang *et al*.,[41] as described in Sec. 2.1. Summarizing, simulations were performed in cubic boxes made up of an equivalent number of cubic cells in each direction. The size of each cell was held constant at 0.109 R_g; however, the overall simulation volume was varied in increments of 0.109 R_g ranging from 3.27 R_g to 5.232 R_g, which corresponds to simulation boxes with 30-48 cells in each direction. When necessary, smaller and larger simulation boxes were also used to check for slight variations in the free energy minima. Each simulation began with setting the initial local values of $\phi_A(\mathbf{r})$ and $\phi_B(\mathbf{r})$ using a Gaussian random number generator, whereas $\rho_P(\mathbf{r})$ was uniform and $\xi(\mathbf{r})$ was zero at all locations. (In certain cases, a prescribed initial morphological condition was specified to examine closely the free energy differences of local minima of comparable magnitudes.)

3.2 Results and Discussion

Results of the simulations are presented below in context of four critical areas of practical interest necessary to understand the physical effects of particle size on the self-assembly processes of tethered-particle/block-copolymer systems. The first phenomenon to be examined is the effect of particle size and particle/block interaction strength on the critical point where ordered phase formation first appears as a function of the A-B interaction energy parameter, $\chi_{AB}N$. Second, the effect of particle size and particle/block interaction strength on the free energy of the overall system is studied, paying particular

attention to its decomposition into energetic and entropic contributions. Next, the variations in the morphological phase diagrams of two systems studied in Ch. 2 in response to changes in particle size are discussed, and finally, several technologically important morphologies induced by particles of different sizes are displayed along with their associated density profiles.

3.2.1 Examination of the critical point for the order/disorder transition

Table 3-1 displays the critical points for the disorder/order transition of the morphological phase envelope at $f_A = 0.5$ for several cases of particle-block interaction parameters, $\chi_{iP}N$, where $i = A, B$, for both B-end-tethered (ABP) and center-tethered (APB) particle/copolymer systems. The critical point is herein defined as the value of $\chi_{AB}N$ in each specific case at which the morphology of the system first switches from a disordered phase to an ordered, lamellar microstructure as f_A is varied over the range [0.2, 0.8]. To obtain a reasonably objective and system-independent quantitative measure of the critical value of $\chi_{AB}N$, we employed the somewhat arbitrary criterion that the critical point occurs when the maximum difference of $\phi_A(\mathbf{r})$ and $\phi_B(\mathbf{r})$ at any location within the system is greater than 0.3; *i.e.*, max $|\phi_A(\mathbf{r}) - \phi_B(\mathbf{r})| > 0.30$. This value was chosen based primarily on intuition gained from past experience more than anything else, although we also chose the value 0.3 based on the match between the known value of $\chi_{AB}N$ (~ 10.5—11.0) for the transition point in the case of a pure A-B block copolymer (*i.e.*, without particles)[86, 87] to the (ABP) case of neutral particles ($\chi_{AP}N = \chi_{BP}N = 0$) with $R_P = 0.1R_g$, which was the smallest value of radius examined herein. For the pure

A-B block copolymer, Leibler[86] calculated a value of 10.5 for the transition, whereas Fredrickson and Helfand[87] determined that the critical point depended on the chain length, approaching a value of ~11 as N decreased from the limit of infinite chain length. As it turned out, however, the exact critical point value calculated in this manner was for the most part independent of the value chosen as long as it fell within the range of [0.2, 0.8], since ϕ_A and ϕ_B vary strongly near the critical point, producing very steep transition functions.

Table 3-1: The critical points (quantified using the value of $\chi_{AB}N$ at the disorder/lamellar transition) of the ABP and APB systems at $f_A = 0.5$. Error is believed to be less than ± 0.05.

	$\pm\chi_{AP}N$	0	5	10	15	20
$R_P\,(R_g)$		*Critical points of the ABP system*				
0.1	$\chi_{AP}N = \chi_{BP}N$	11.0	11.0	11.0	11.0	11.0
	$\chi_{AP}N = -\chi_{BP}N$		10.9	10.9	10.9	10.9
	$-\chi_{AP}N = \chi_{BP}N$		11.0	11.0	11.0	11.0
0.2	$\chi_{AP}N = \chi_{BP}N$	11.1	11.1	11.1	11.1	11.1
	$\chi_{AP}N = -\chi_{BP}N$		11.0	10.8	10.7	10.5
	$-\chi_{AP}N = \chi_{BP}N$		11.3	11.4	11.6	11.7
0.3	$\chi_{AP}N = \chi_{BP}N$	11.5	11.5	11.5	11.5	11.5
	$\chi_{AP}N = -\chi_{BP}N$		11.1	10.6	10.1	9.6
	$-\chi_{AP}N = \chi_{BP}N$		11.9	12.3	12.7	13.0
0.4	$\chi_{AP}N = \chi_{BP}N$	12.2	12.1	12.1	12.1	12.0
	$\chi_{AP}N = -\chi_{BP}N$		11.3	10.3	9.1	7.8
	$-\chi_{AP}N = \chi_{BP}N$		12.8	13.4	13.8	14.0
		Critical points of the APB system				
0.1	$\chi_{AP}N = \chi_{BP}N$	10.9	10.9	10.9	10.9	10.9
	$\chi_{AP}N = -\chi_{BP}N$		10.9	10.9	10.9	10.9
0.2	$\chi_{AP}N = \chi_{BP}N$	11.0	11.0	11.0	11.0	11.0
	$\chi_{AP}N = -\chi_{BP}N$		11.0	11.0	11.0	11.0
0.3	$\chi_{AP}N = \chi_{BP}N$	11.2	11.2	11.2	11.2	11.2
	$\chi_{AP}N = -\chi_{BP}N$		11.2	11.2	11.1	11.0
0.4	$\chi_{AP}N = \chi_{BP}N$	11.7	11.6	11.6	11.6	11.6
	$\chi_{AP}N = -\chi_{BP}N$		11.6	11.4	11.0	10.6

In the absence of particles, the critical point occurs at $f_A = 0.5$, since this corresponds to the highest free energy of interaction based on the maximum in the internal energy, which varies as the integral of the term $\chi_{AB}N\phi_A(\mathbf{r})\phi_B(\mathbf{r})$ and which quantifies the concept that the highest energy state corresponds to the situation which contains the most repulsive interactions; *i.e.*, the case where the number of A and B segments is the same. Keep in mind that although the A and B segments experience repulsive interactions with each other, from a statistical point of view they are equivalent, implying that chain configurational entropy is constant irrespective of the value of f_A in the disordered phase; *e.g.*, see Figure 2-2. Consequently, the maximum in the internal energy at $f_A = 0.5$ determines the exact value of the critical point. It corresponds to the point where the A-B repulsive interactions become large enough to induce a transition to an ordered phase, even though such an occurrence drastically reduces the chain configurational entropy. In the presence of particles, however, the value of f_A is only approximately 0.5 since the particles contribute to the free energy of the system through the integral of the additional energetic terms $\chi_{AP}N\phi_A(\mathbf{r})\phi_P(\mathbf{r}) + \chi_{BP}N\phi_B(\mathbf{r})\phi_P(\mathbf{r})$ in Eq. (2.1). In other words, given the continuity expression $f_A + f_B + f_P = 1$, the transition point is located in the general neighborhood of $f_A \approx 0.5$ since $f_P \ll 1$.

For the ABP system, four cases were examined: the first (case 1) was $\chi_{AP}N = \chi_{BP}N = 0$, corresponding to neutral particles. Case 2 was given by $\chi_{AP}N = \chi_{BP}N > 0$, corresponding to particles disfavoring both A and B segments, as well as cases 3 and 4 where $\chi_{AP}N = -\chi_{BP}N \neq 0$, in which the value of $\chi_{AP}N$ was both positive and negative, corresponding to particles disfavoring A segments while favoring B segments, and vice

versa. In all cases, the absolute value of $\chi_{AP}N$ was varied over the range of [0, 20]. For center-tethered particle chains (APB), only three cases were studied due to the symmetry of the copolymer; hence the case where $\chi_{AP}N$ assumed negative values was physically equivalent to the one in which it was always positive.

3.2.1.1 End-tethered particle/copolymer systems

3.2.1.1.1 Case 1

From Table 3-1, it is evident that the critical point of the B-end-tethered neutral particle system (case 1: $\chi_{AP}N = \chi_{BP}N = 0$) is a strong function of particle radius, increasing from a value of 11.0 for $R_P = 0.1R_g$ to 12.2 for $R_P = 0.4R_g$. One must keep in mind that the stable, equilibrium morphology of the system is determined by the global minimum in free energy with respect to each possible microphase. Whereas the free energy is the sum of two contributions, *i.e.*, the internal energy and the entropy ($F = U - TS$), the transition from the disordered phase to the ordered, lamellar structure is dictated by a complex balance between these two contributions. The internal energy contribution to F is given by the integral of the first three terms of the integrand on the right side of Eq. (2.1), $\chi_{AB}N\phi_A(\mathbf{r})\phi_B(\mathbf{r}) + \chi_{AP}N\phi_A(\mathbf{r})\phi_P(\mathbf{r}) + \chi_{BP}N\phi_B(\mathbf{r})\phi_P(\mathbf{r})$, whereas the entropic contribution is constituted of all the remaining terms in Eq. (2.1). Since it is universally true that $\phi_P \ll 1$, $\phi_B \approx 1 - \phi_A$, the integrand of the energetic contribution to the free energy can be expressed as approximately equal to $\chi_{AB}N\phi_A(1 - \phi_A) + \chi_{AP}N\phi_A\phi_P + \chi_{BP}N(1 - \phi_A)\phi_P$. For neutral particles, only the first of these terms is non-zero, and in the disordered phase, ϕ_A tends to values in the middle of its range of [0, 1] because the entropic contribution dominates the free energy, even though the internal

energy attains its maximum value at about $\phi_A \approx 0.5$. As $\chi_{AB}N$ increases, the internal energy within the disordered phase increases proportionally, driving up the free energy even though the entropic contribution still dictates the stable (disordered) morphology and changes little with increasing $\chi_{AB}N$. Nevertheless, given the inverted parabolic form of the internal energy contribution ($\chi_{AB}N\phi_A[1-\phi_A]$), eventually the free energy of the system can be lowered by driving ϕ_A toward the fringes of its range, causing an abrupt, dramatic decrease in the internal energy, and hence initiating a phase separation to a more ordered phase, even though this results in a substantial decrease in the configurational entropy of the system. [The reader can visualize the above arguments with reference to Figure 3-2, below.]

With no intrinsic preference for A or B segments ($\chi_{AP}N = \chi_{BP}N = 0$), neutral particles contribute directly only to the entropic part of the free energy, although they indirectly influence the internal energy by locally affecting the value of ϕ_A. Hence when the neutral particles are relatively small, they do not greatly influence the system configurational entropy or internal energy, and values of $\chi_{AB}N$ at the critical point are approximately the same (10.5—11.0) as in the case of a pure A-B block copolymer.[86-88] As particle size becomes significant, however, the particles influence the entropic contribution to the free energy by increasing the effective non-local particle volume fraction, $\overline{\phi}_P$, according to the Carnahan-Starling expression in Eq. (2.1), $\left(4\overline{\phi}_P - 3\overline{\phi}_P^2\right)/\left(1-\overline{\phi}\right)^2$. Hence increasing particle size, which effectively increases $\overline{\phi}_P$, results in a corresponding increase in the configurational entropy of the system. Although A and B segments are statistically equivalent, the same is not true of the particles, and

hence increasing particle volume fraction results in an increase of the entropic contribution to the free energy. As a consequence, the energetic repulsive interactions of the A and B segments must be stronger as R_P increases in order to overcome the additional entropic penalty associated with forcing the chains into an ordered state.

For the most part, the neutral particles generally concentrate within the B-rich domains since they are tethered to the B-end of the block copolymer. However, in some circumstances, the neutral particles will preferentially occupy sites that tend to screen the repulsive A and B segments from each other at the interfaces of the A-rich and B-rich domains, thereby effectively lowering the internal energy contribution to the free energy. As a consequence, a greater value of $\chi_{AB}N$ is required to reduce the mitigating screening effect of the particles in order to drive the system into an ordered phase. As the particles increase in size, their screening potential becomes higher, and thus it requires a greater degree of repulsion between the A and B segments to initiate a microphase separation. Therefore, in these circumstances, this additional screening mechanism can play an important role in determining the relative concentrations of the particles within and at the interfaces of the A-rich and B-rich domains.

3.2.1.1.2 Case 2

Irrespective of particle size, when the particles are equally repulsive to both A and B segments, the effect of increasing $\chi_{iP}N$ is negligible. When $\chi_{iP}N < \chi_{AB}N$, the particles can still act as screens, although less effectively, between the more repulsive A and B segments. However, once $\chi_{iP}N > \chi_{AB}N$, the driving force toward particle screening between the A and B segments is removed, resulting in a lower entropically-induced

increase in F, and therefore one might expect to observe an associated decrease of the critical value of $\chi_{AB}N$. This is due to the fact that the particle no longer has a screening effect when it is highly repulsive to both blocks, and as such it merely acts as an additional segment attached to the end of the B chain, which does not affect the configurational state of the polymer chain to as great of a degree as it does when the particle prefers to locate between the highly repulsive A and B segments, regardless of the magnitude of $\chi_{iP}N$. Nevertheless, the overall effect of repulsive particles to both A and B segments is to lower the critical value of $\chi_{AB}N$ necessary to induce a morphological phase transition from a disordered state to an ordered one, although this trend is very slight given that the contributions of $\chi_{iP}N$ to the free energy are quite small in that the energetic term, $\chi_{AB}N\phi_A(1-\phi_A)+\chi_{AP}N\phi_A\phi_P+\chi_{BP}N(1-\phi_A)\phi_P$, is relatively unchanged since $\phi_P \ll 1$. Consequently, such a trend is only barely noticeable in the data of Table 3-1 for the largest particle radius, $R_P = 0.4R_g$, where the slight additional contribution of the particles to the internal energy effectively lowers the necessary degree of repulsion (quantified by $\chi_{AB}N$) to initiate a transition to an ordered morphology.

Although there appears to be little effect on the value of the critical point, increasing the particle/block interaction parameters when $\chi_{AP}N = \chi_{BP}N > 0$ induces a slight but definite increase in the degree of segregation between the A-rich and B-rich domains, as displayed in Figure 3-1 for the case of $R_P = 0.2R_g$. This appears to be a consequence of the slight but increasing contribution to the internal energy of the particle density distribution, $\chi_{AP}N\phi_A\phi_P+\chi_{BP}N(1-\phi_A)\phi_P$, and hence to the overall system free

energy, which effectively pushes the phase separating ordered morphology slightly further toward the fringes of the ϕ_A range [0, 1].

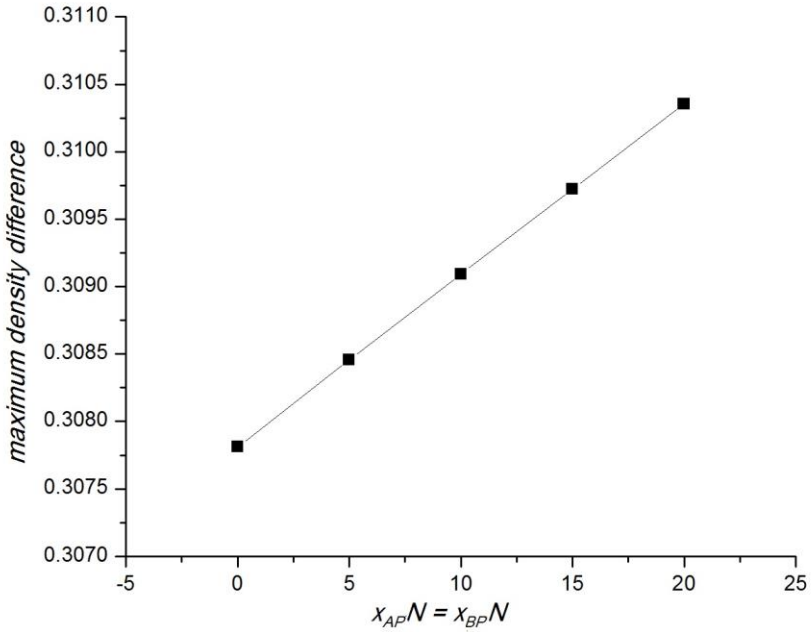

Figure 3-1. The maximum density difference ($max|\phi_A - \phi_B|$) as a function of the particle/block interaction parameters $\chi_{AP}N = \chi_{BP}N$ at $R_P = 0.2R_g$ and $\chi_{AB}N = 11.1$ in the ABP system.

3.2.1.1.3 Case 3

The next case corresponds to the situation where the particles disfavor the A segments and favor the B segments; *i.e.*, $\chi_{AP}N > 0$ and $\chi_{BP}N < 0$. In this case, there is a generally strong decrease in the critical value of $\chi_{AB}N$ affected by the increasing magnitude of $\chi_{AP}N = -\chi_{BP}N$, which grows stronger as particle size is increased—see Table 3-1. At the smallest particle radius, $R_P = 0.1R_g$, the effect is only slight. This is a consequence of the small reduction in the internal energy due to the presence of the particles, not only since $\phi_P \ll 1$, but also since the contributions of the two particle terms to the internal energy have opposite signs and tend to cancel each other since $\chi_{AP}N =$

$-\chi_{BP}N$. The net effect is to lower the value of $\chi_{AB}N$ necessary to achieve the ordered phase formation. With regard to the entropy, since the particles are attached to the end of the B block, which they favor, there is no driving force to induce a major configurational rearrangement in which the particles encroach upon the A block, which the particles disfavor. Consequently, the situation for particles of size $R_P = 0.1R_g$ is very similar to the case of particles which are repulsive to both A and B segments, with similar quantitative values of the critical point between these two cases. As particle size increases, the critical point likewise increases due to the increase in ϕ_P manifesting through the Carnahan-Starling excluded volume potential; *i.e.*, the entropy grows commensurately with particle size, as discussed previously.

For larger particle radii, the decreasing trend with increasing particle interaction strength becomes more significant—see Table 3-1. This is primarily caused by a dramatic decrease in the internal energy with ordered phase formation since the particles are highly motivated to congregate in the B-rich domains of the overall system. The driving force is thus the tendency of the particles to migrate away from A segments and surround themselves with B segments. Consequently, the internal energy contribution to the free energy, $\chi_{AB}N\phi_A(\mathbf{r})\phi_B(\mathbf{r}) + \chi_{AP}N\phi_A(\mathbf{r})\phi_P(\mathbf{r}) + \chi_{BP}N\phi_B(\mathbf{r})\phi_P(\mathbf{r})$, dominates the free energy. In the disordered state, where the particles are more evenly distributed throughout the domain, the final two terms in the above expression tend to cancel themselves out due to the difference in signs of the interaction parameters, $\chi_{AP}N = -\chi_{BP}N$. In the ordered state, ϕ_P concentrates in the B-rich regions and is relatively depleted in the A-rich regions, and hence the magnitude of the third term is significantly greater than that of the

second. Since the third term involves an attractive interaction parameter (*i.e.*, it is negative), its net effect is to lower the internal energy of the system and thereby induce an ordered phase formation at a lower value of the critical point than would otherwise occur. This trend increases dramatically with increasing particle/block interaction strength, resulting in the substantial decrease in the critical point within increasing $\chi_{AP}N = -\chi_{BP}N$ at constant particle radius, as observed in Table 3-1.

3.2.1.1.4 Case 4

The final case of the ABP system corresponds to the situation in which the particles favor the A segments and disfavor the B segments; *i.e.*, $\chi_{AP}N < 0$ and $\chi_{BP}N > 0$. As the magnitude of $\chi_{AP}N$ increases, the effect on the critical point is extremely pronounced, showing a substantial increase in the value of $\chi_{AB}N$. This dramatic rise is due to the weighting of the relative effects of entropy and internal energy on the free energy. Due to the mismatch in the signs of $\chi_{AP}N$ and $\chi_{BP}N$, the particles tend to migrate to regions of high A segment concentrations, distorting the B-block chain configurations into low entropy states, and hence driving up the free energy. However, since the particles are repulsive to B segments, they are not effective at screening the A and B segments from each other, as in the case of neutral particles. Indeed, for higher magnitudes of $\chi_{AP}N$ the particles are actually concentrated within the A-rich domains and A segments occupy interfacial locations with the B segments since the repulsion between A and B segments is weaker than the repulsion between B segments and the particles. This imparts even greater configurational contortions to the B-blocks of the chains, thus driving down the entropy and increasing the free energy of the disordered state. Furthermore, since the

internal energy expression scales with particle interaction strength as $\chi_{AB}N\phi_A(\mathbf{r})\phi_B(\mathbf{r}) + \chi_{AP}N\phi_A(\mathbf{r})\phi_P(\mathbf{r}) + \chi_{BP}N\phi_B(\mathbf{r})\phi_P(\mathbf{r})$, there is a strong positive contribution to the free energy resulting from the relatively high magnitude of the second (positive) term with respect to the third (negative) term. On account of this, a higher absolute value of $\chi_{AB}N$ is required to drive the system to the ordered state to overcome the entropic penalty of forcing the blocks and particles into a configurationally unfavorable state.

3.2.1.2 Center-tethered particle/copolymer systems

3.2.1.2.1 Case 1

The center-tethered particle/copolymer system with neutral particles exhibited the same qualitative behavior as the end-tethered system; *i.e.*, the critical value of $\chi_{AB}N$ at the disorder/order transition increased with particle radius, as displayed in Table 3-1. As in the ABP system, there was only a slight effect at small particle radii, which was due to the low configurational entropic penalty induced by the presence of the particles. For larger particle radii, where the impact of the particles on the internal energy was more severe, again the effect on the critical point was more substantial, but for each value of particle radius, the cumulative effect was smaller for the center-tethered particle system than the end-tethered one. For example, at $R_P = 0.4R_g$, the critical point of the ABP system occurred at $\chi_{AB}N = 12.2$, whereas it occurred at 11.7 for the APB system—see Table 3-1. This is a direct consequence of the tethering position: for the center-tethered system, the neutral particle was already located at a point in the chain where it could induce maximal screening between the repulsive A and B segments, without causing a

substantial decrease in the configurational entropy of the B block, as required in the ABP system. Consequently, the entropic penalty imparted to the free energy imposed a significantly lower entropically-induced increase in F in the APB system than in the ABP, hence requiring a smaller energetic contribution from $\chi_{AB}N$ in the APB system relative to the pure copolymer case to induce the morphological phase transition from a disordered state to an ordered one.

3.2.1.2.2 Case 2

When the particles disfavor both blocks equally ($\chi_{AP}N = \chi_{BP}N > 0$), there is practically no effect of particle interactions on the critical point irrespective of the magnitude of the specific value of $\chi_{AP}N$. Since the particle is located at the center of the chain, once again the decrease in the configurational entropy of the APB system is very slight relative to that in the ABP system. The particles tend to concentrate at the interfaces between the A-rich and B-rich domains, as one might expect from their tethering location, essentially screening the A segments from the B segments. However, since the particles are equally repulsive to both types of segments, there is no impetus for the particles to change location as $\chi_{AP}N$ is increased, implying that this quantity has little effect on the configurational entropy. Furthermore, whereas the contributions of the particle/block interaction parameters to the internal energy are very small (since $\phi_P \ll 1$), there is not much difference in the free energy from one value of $\chi_{AP}N$ to the next. Therefore, even at the largest particle radius, only a slight effect is barely discernible in Table 3-1.

3.2.1.2.3 Case 3

In the third case, where particles disfavor the A segments and favor the B segments (*i.e.*, $\chi_{AP}N > 0$ and $\chi_{BP}N < 0$), there is essentially no discernible effect of increasing $\chi_{AP}N$ on the critical point except for the largest particle radius, $R_P = 0.4R_g$. This is primarily a result of the tethering location, which tends under most conditions to concentrate the particles at the interface, rather than within domains of A-rich or B-rich phases. Consequently, with ϕ_P more spatially uniform (with respect to the A-rich and B-rich domains), the opposite signs in the particle contributions to the internal energy (*i.e.*, $\chi_{AP}N = -\chi_{BP}N$) tend to cancel each other out, thereby mitigating any potential impact on the free energy of the overall system.

In the case of $R_P = 0.4R_g$, the trend is one of decreasing values of $\chi_{AB}N$ at the critical point as the particle/block interaction parameters increase in magnitude. Even though the particles always remain concentrated at the interfaces between the A-rich and B-rich domains on account of their tethering location, the increasing repulsion/attraction between the particles and A/B segments tends to shift their concentration increasingly toward the B-rich interfacial region as $\chi_{AP}N$ $(= -\chi_{BP}N)$ increases. Hence there is a slight configurational entropic penalty that affects the critical point as the particles are pulled deeper into the B-rich domain by their attractive interactions with the B segments and repulsive interactions with the A segments. Furthermore, the internal energy decreases since the negative B-P interaction term in the internal energy expression becomes increasingly significant relative to the A-P interaction term. The net result is the

decreasing trend in the critical point with increasing $\chi_{AP}N$, as evident in Table 3-1, since a lower value of $\chi_{AB}N$ is required to initiate a phase separation into an ordered phase.

3.2.2 Thermodynamics of tethered particle/block copolymer systems

The effects of the tethered particles on the overall system thermodynamics can be assessed by examining the relative changes in the free energy, internal energy, and entropy in response to variations of particle size and interaction strength. In the following discussion, we examine only neutral particle ABP and APB systems ($\chi_{AP}N = \chi_{BP}N = 0$), since similar diagrams and arguments to those described below apply to the other cases discussed in Section 3.2.1. In Figure 3-2, plots of ΔF, ΔU, and $-\Delta TS$ are displayed as functions of $f_A \in [0.2, 0.8]$ for the ABP and APB systems. U and ΔTS are rendered dimensionless in the same fashion as ΔF; *i.e.*, with respect to $N_c k_B T$. Values of the entropy change are calculated with reference to the value of TS for the $R_P = 0.1R_g$ particles at $f_A = 0.2$; hence the value of $-\Delta TS = 0$ for the $R_P = 0.1R_g$ curve at the point $f_A = 0.2$ in Figure 3-2e, f. This then translates into appropriate relative reference points for ΔF and ΔU that are determined from the Legendre transformation $\Delta F = \Delta U - \Delta TS$. The value of the A-B interaction parameter is held constant in the following discussion at $\chi_{AB}N = 18$ since this value is known to produce a wide variety of morphologies, dependent on the particular value of f_A under consideration—see Ch. 2. Note that the global maxima in the ΔF curves and the global minima in the ΔU curves do not occur exactly at $f_A = 0.5$ due to the small but finite effect of the particles. Also note that the

three panels of the APB systems, Figure 3-2b, d, and f, only cover the range of $f_A \in [0.2, 0.5]$ since the curves are symmetric due to the center-tethered particle location.

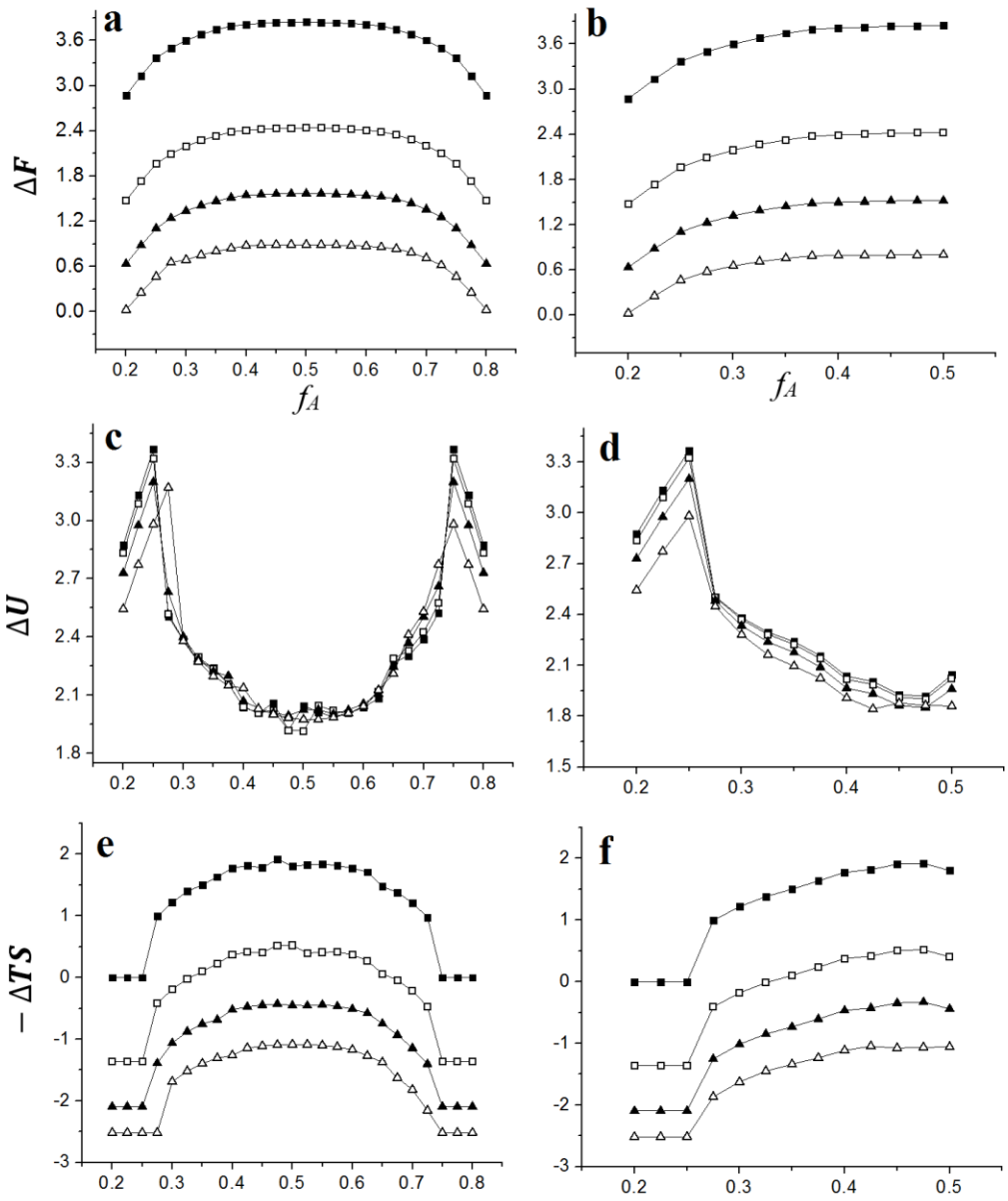

Figure 3-2. Key thermodynamic quantities as functions of f_A for neutral particles of varying radii at $\chi_{AB}N = 18$. The left column is the ABP system and the right column is the APB system. Symbols denote particles of a certain radius as follows: ■ ($0.1R_g$), □ ($0.2R_g$), ▲ ($0.3R_g$), and △ ($0.4R_g$). Panels a, b depict the free energy change (ΔF), c, d show the internal energy change (ΔU), and e, f display the entropic change ($-\Delta TS$).

3.2.2.1 Effect of particle size

3.2.2.1.1 The ABP system

The effects of the tethered particles on the overall system thermodynamics can be assessed by examining the relative changes in the free energy, internal energy, and entropy in response to variations of particle size and interaction strength. First, we will examine the thermodynamics of the ABP tethered-particle/copolymer system. From Figure 3-2e, it is evident that $-\Delta TS$ is constant at both low and high values of f_A (*i.e.*, 0.275 < f_A > 0.75), regardless of particle size. This is because of the statistical equivalence of the A and B segments, as discussed in 3.2.1.1: since the A and B segments are statistically indistinguishable from each other, there is no entropy of mixing effect upon the system as f_A is varied. The entropy increases with increasing particle size in Figure 3-2e, which is due to the Carnahan-Starling form of the excluded volume potential, $\left(4\overline{\phi}_P - 3\overline{\phi}_P^2\right)/\left(1-\overline{\phi}\right)^2$, which is an increasing function of particle size since $\overline{\phi}_P$ scales with R_P. Hence the particles, which are not statistically equivalent with the A and B segments, increase the system configurational entropy by augmenting the final term in the continuity equation $f_A + f_B + f_P = 1$, thereby introducing an entropy of mixing effect into the system. When $f_A \in [0.3, 0.725]$, the entropy experiences a sharp decrease on account of the transition to one of several well-known ordered phases (lamellar, cylindrical, spheroidal, *etc*.), depending on the particular value of f_A. This is caused by the packing frustration experienced by the chains as they experience configurational changes to accommodate the ordered phase formation. The entropy change exhibits a minimum at $f_A \approx 0.5$, which is due to the increasing degree of order

imparted to the system as the number of A and B segmental interactions (with strength $\chi_{AB}N$) are maximized because the number of A and B segments are approximately equal at this value of f_A.

In the range of $0.275 < f_A > 0.75$, the internal energy of the ABP system changes dramatically, as evident in Figure 3-2c, increasing at low f_A and decreasing at high f_A. This is caused by the increasing number of A-B interactions in the disordered phase and the relative numbers of A and B segments as f_A increases (at low values of f_A), thereby influencing the overall strength of the repulsive A-B interactions. However, in the range of $f_A \in [0.3, 0.725]$, the internal energy experiences an abrupt, significant decrease as the ordered phases are formed, which greatly reduce the number and strength of A-B interactions. A minimum is evident at $f_A \approx 0.5$, even though in principle a stronger A-B overall interaction energy would be intuitively expected due to the equal number of A and B segments; however, the increase in the degree of ordering more than offsets this effect. As particle size increases, there is a significant drop in the internal energy change, which is a result of the fact that larger particles more effectively screen the A and B segments from each other. Mathematically speaking, for neutral particles $\chi_{AP}N = \chi_{BP}N = 0$, which implies that the internal energy varies as $\chi_{AB}N\phi_A\phi_B$; *i.e.*, ϕ_A and ϕ_B decrease slightly on average as particle size, and hence ϕ_P, increases due to the incompressibility condition. An interesting observation taken from Figure 3-2c is that there does not appear to be much effect of particle size on the internal energy change inside the ordered-phase regime of the ABP system when $f_A \in [0.3, 0.725]$. This can partially be explained by considering the tethering location of the particles. Since the

particles are tethered to the B-end of the block copolymer chain, as the degree of order increases, the particles are effectively confined to the B-rich domains by the entropic chain packing frustration, thereby effectively reducing the screening effect between A and B segments at the interfaces of the A-rich and B-rich domains. Since the interfaces are relatively depleted of particles, the local particle volume fraction, ϕ_P, in these regions is very small, and hence does not affect the internal energy, $\chi_{AB}N\phi_A\phi_B$, to an appreciable degree.

The free energy change within the ABP system is quantified by the difference in the internal energy and entropy changes through the Legendre transformation $\Delta F = \Delta U - \Delta TS$. In the disordered state, when $0.275 < f_A > 0.75$, the free energy rises rapidly as f_A increases or decreases from the extremes of its range. Here, the free energy change is identical with the change in the internal energy, since the change in the entropic contribution to ΔF is zero—see panel Figure 3-2e. Hence a sharp parabolic profile is observed, as expected from the mathematical form of $U = \chi_{AB}N\phi_A\phi_B \approx \chi_{AB}N\phi_A(1 - \phi_A)$. When $f_A \in [0.3, 0.725]$, ΔF flattens off to a maximum at $f_A \approx 0.5$ in the ordered phase regime, since the sharp parabolic form of the internal energy is dampened by the decrease in the entropic contribution to the free energy. This flatness of ΔF in the ordered-phase region indicates only slight free energy differences between the various ordered-phase morphologies appearing within this range of f_A values. As the particle size increases, ΔF decreases, with the primary determinant being the entropic contribution, since the internal energy does not change substantially with particle radius, as discussed above.

3.2.2.1.2 The APB system

The thermodynamics of the APB system are very similar to those of the ABP system, with the minor exception of the internal energy change, which exhibits a distinct trend with respect to variable particle radius; *i.e.*, within the ordered-phase regime of $f_A \in [0.3, 0.725]$, the internal energy decreases as particle size increases, as displayed in Figure 3-2d. The reason for this is related to the tethering position of the particle, directly between the A and B blocks of the particle chain. At this location, the particles are always at positions near to the interfaces of the A-rich and B-rich domains where they can effectively screen the A and B segments from each other, thereby reducing the A and B net repulsive energy in the system. The mitigating effects of this screening are felt more substantially for the larger particles, which create a more effective blocking network between the A and B segments. From a mathematical perspective, the local particle concentrations, ϕ_P, at the interfaces are relatively higher with respect to the ABP system, and hence the interfacial internal energy change, $U = \chi_{AB} N \phi_A \phi_B$, decreases significantly with particle size since ϕ_A and ϕ_B at the interfaces are substantially smaller than in the ABP case.

3.2.2.2 Effect of particle/block energetic interactions

The effects of the particle/block interaction potential upon the thermodynamic properties of the system are presented in Figure 3-3 for the ABP and APB systems for particles that disfavor both blocks of the copolymer chain; *i.e.*, $\chi_{AP} N = \chi_{BP} N \equiv \chi_{A/BP} N \geq 0$. The value of the A-B interaction parameter, $\chi_{AB} N$, is once again set at the value 18, whereas the particle block interaction parameters vary over the range [0, 15].

The reference state is the same as in Figure 3-2: all quantities are calculated relative to the value of entropic contribution to the free energy at $R_P = 0.1R_g$, $f_A = 0.2$ and $\chi_{A/BP}N = 0$. Once again, the APB profiles are symmetric around the corresponding maximum in each curve, such that only the limited range of $f_A \in [0.2, 0.5]$ is presented in panels b, d, and f of Figure 3-3.

In the case of interacting particles, the behavior of the thermodynamic functions with respect to particle/block interaction energy is essentially independent of the tethering point of the particle along the chain backbone. Hence the ABP and APB systems can be discussed collectively, with only small quantitative discrepancies between the two cases. The entropic contributions to the free energy are independent of the interaction potential, as would be expected, since these are not direct functions of $\chi_{A/BP}N$. Since the particles are equally repulsive to both types of segments, the statistical configurational state of the chains is unaffected by the particle/segment interaction strength. In other words, the maximum entropy configurational state is the same as for the neutral particle case, implying equivalent morphologies for any particular value of $\chi_{AB}N$. (We shall see an interesting consequence of this observation in §3.2.3.) The internal energy changes slightly with particle/block interaction strength, increasing with $\chi_{A/BP}N$. This is the expected consequence of the energetic expression $\chi_{AB}N\phi_A(1-\phi_A) + \chi_{AP}N\phi_A\phi_P + \chi_{BP}N(1-\phi_A)\phi_P$, which grows stronger as $\chi_{A/BP}N$ increases. This directly impacts the free energy change within the system, producing an inverted parabolic profile for ΔF that grows sharper with increasing $\chi_{A/BP}N$. The ΔF profiles in Figs. 3-3a, b tend to flatten out in the

middle of the f_A range, indicating fairly similar free energy values of the various ordered phases that appear in this region of the phase diagram.

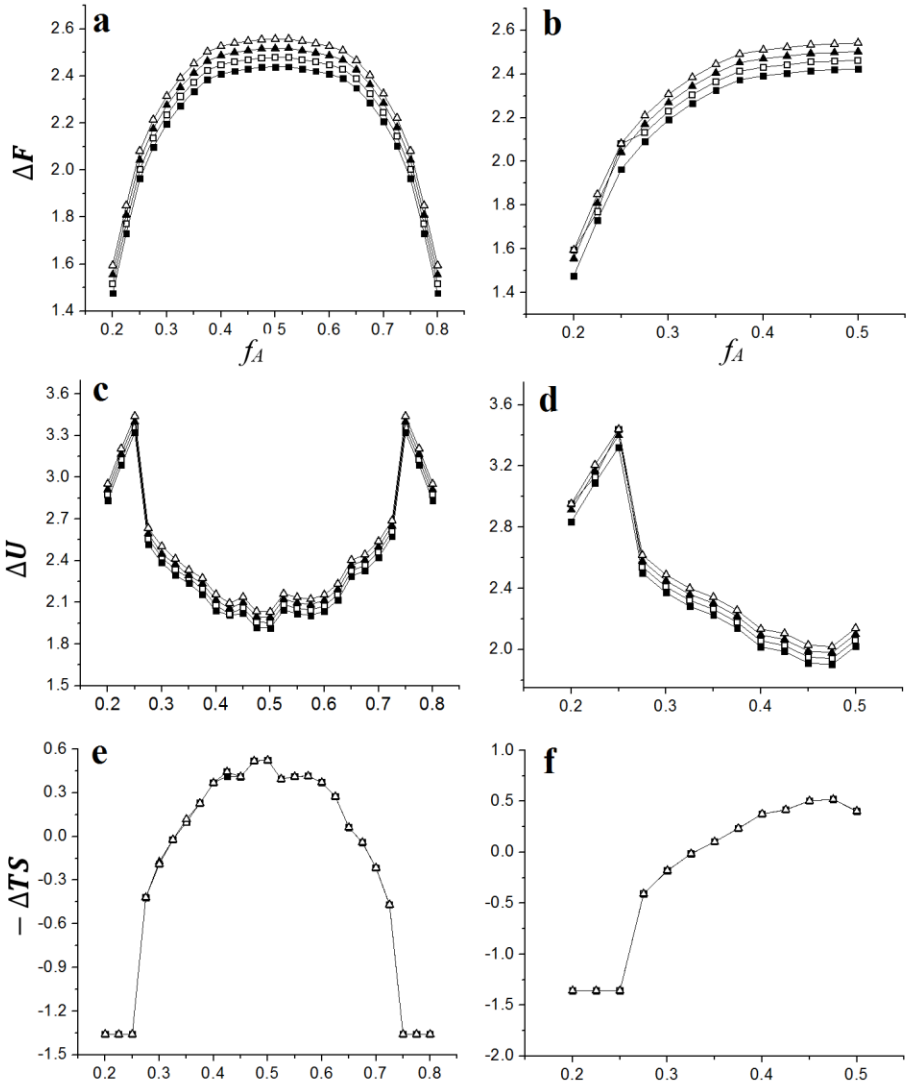

Figure 3-3. The thermodynamic quantities as functions of f_A for repulsive particles of varying interaction potential strength, where $\chi_{AP}N = \chi_{BP}N \equiv \chi_{A/BP}N \geq 0$ at $\chi_{AB}N = 18$ and $R_P = 0.2R_g$. The left column is the ABP system and the right column is the APB system. Symbols denote particles of a certain interaction energy as follows: ■ ($\chi_{A/BP}N = 0$), □ ($\chi_{A/BP}N = 5$), ▲ ($\chi_{A/BP}N = 10$), and △ ($\chi_{A/BP}N = 15$). Panels a, b depict the free energy change (ΔF), c, d show the internal energy change (ΔU), and e, f display the entropic change ($-\Delta TS$).

3.2.3 Particle size effect on the morphology

Morphological phase diagrams for several cases of ABP and APB tethered-particle/copolymer systems were presented in Ch. 2. The effect of particle size on the phase diagrams is discussed below with reference to the neutral particle ($\chi_{A/BP}N = 0$) ABP and APB systems at $\chi_{AB}N = 18$, since these phase diagrams are representative of those found in the other cases discussed previously in §3.2.1and §3.2.2. Phase diagrams (in R_P-f_A space) for these two cases are presented in Figure 3-4. The APB phase diagram is symmetric about the point $f_A \approx 0.5$ due to the centralized tethering position of the particles between the two blocks of the copolymer chains.

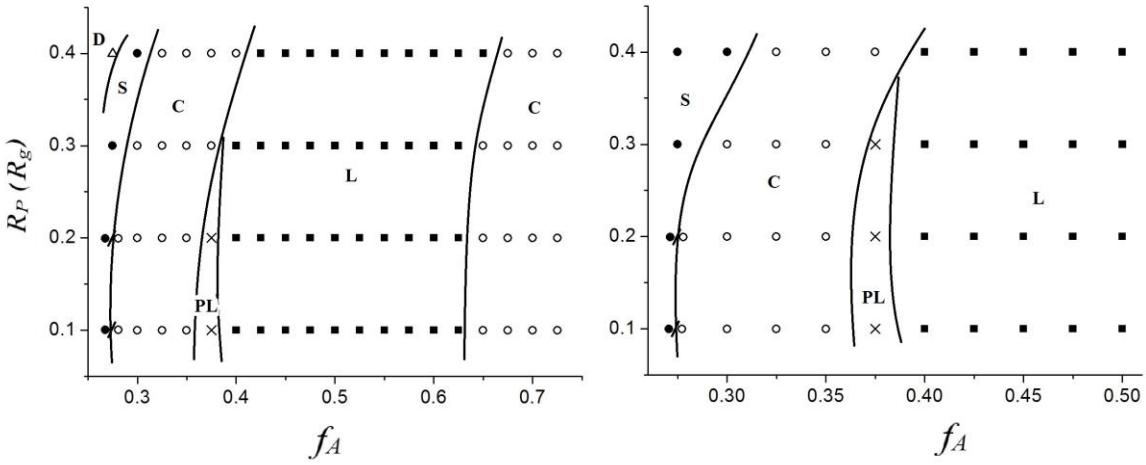

Figure 3-4. Morphological phase diagrams of the ABP (left panel) and APB (right panel) systems as functions of f_A for different particle radii at $\chi_{AB}N = 18$ and $\chi_{A/BP}N = 0$. The symbols in these diagrams denote various phases as follows: ■ lamellae (L), ○ cylinders (C), ● spheroids (S), ●/○ the cylinder/spheroid transition zone, × perforated lamellae (PL), and △ disordered (D).

In the ABP system, the predominant ordered phase is the lamellar (denoted as 'L' in Fig. 3-4) for all particle radii, which stretches over roughly 25% of the available f_A range in the middle of the phase diagram. Particles are typically dispersed within the B-rich domains,

in some circumstances tending to concentrate at the interfaces between the two types of domains. On either side of the lamellar region is a cylindrical phase (C), which consists of either B-rich cylinders arranged in a hexagonal packing pattern contained within an A-rich matrix phase (high f_A), or vice versa (low f_A). As observed previously, particles tend to disperse within the B-rich phase (at low f_A) due to the tethering location, but sometimes congregate at the interface between the two phases (see Figure 3-5). An interesting feature of these hexagonally-packed cylinder domains is that at low f_A the particles tend to concentrate in very small regions within the matrix phase that are arranged symmetrically around the cylinder phase in a hexagonally packed array, forming cylindrical nanowire structures that parallel the cylindrical domains—see Figure 3-5a. At the low and high extremes of the f_A range, ordered phases consisting of spheroids (S) arranged on body-centered cubic lattices are observed, with the particles concentrated within the B-rich spheroids or at the interfaces for high f_A values, or within the B-rich matrix phase at low f_A. At the far extremes of the f_A range, disordered phases (D) still remain visible in the phase diagram. At low values of particle radii, there exists a small region of the phase diagram of Figure 3-4 where a perforated lamellar morphology (PL) is the lowest free energy state (see Figure 3-6).

Regardless of particle diameter, the driving force behind the ordered-phase formation, and the particular ordered morphology that is formed, is the minimization of the overall free energy, which results from a delicate balance between the energetic effects which favor the ordering process and the entropic configurational effect which favors a disordered state. Ordered-phase formation is favorable to the free energy because it

minimizes repulsive interactions between the A and B segments; however, this creates unnatural chain configurations (packing frustration) as the copolymer blocks contort to adjust to the spatial constraints forced on them by the geometry of the ordered phase. Consequently, which ordered morphology appears under a given circumstance is a strong function of f_A, since this determines the number of A-B repulsive interactions: the more A-B interactions, the stronger the energetic effect contributes to the free energy, which leads to a higher possible degree of packing frustration imparted to the copolymer chains. Hence a critical determiner of the particular ordered morphology formed for a specified value of f_A is the surface area to volume ratio; *i.e.*, a large interfacial surface area allows for a higher energetic contribution to the free energy since more A and B segments can interact with each other, whereas a large volume (in the minority phase) results in a lower degree of chain packing frustration, which lowers the entropic contribution to the free energy. Therefore, as the overall average interfacial surface area to volume ratio (S/V) increases, the tendency is to drive the system morphology toward the disordered state. When f_A is approximately 0.5, there are relatively many A-B interactions, and both blocks of the chain are fairly long. Hence a large relative volume is required to relieve some of the packing frustration, while at the same time a relatively small surface area is required to minimize the A-B interactions as much as possible. These conditions favor the formation of the lamellar morphology. As f_A decreases, the B blocks become larger and the A blocks comprise the minority phase. Since the A blocks of the chains are shorter, they are able to pack into smaller volumes, thus allowing for geometric structures with greater surface areas, such as hexagonally arranged cylinders, to appear since the

number of A-B interactions is lower simply because the number of A segments is lower. Further decrease in f_A allows the A blocks to pack into even smaller volumes with greater surface area, such as spheroids. At the extreme ends of the f_A range, the number of A-B interactions is so few, due to the shortness of one block or the other of the chain, that the configurational entropy dominates the free energy and the chains take on more natural configurations, producing the disordered phase.

The effect of particle radius on the phase diagram is remarkable. For very low radii, the effects of the particle are only slight, and the phase diagram is very similar quantitatively to that of the pure diblock copolymer system. The effect of increasing particle size is to drive the phase diagram transition zones inwards toward the mid-range of f_A. Since the larger particles impart a greater entropic contribution to the free energy than the smaller ones (as discussed in §3.2.1and §3.2.2), their net effect is to drive the system morphology toward a larger value of S/V at a constant value of f_A. In other words, the larger particles create a greater degree of packing frustration at a specific value of S/V, which implies a greater entropic contribution to the free energy.

The phase diagram of the APB system is very similar to that of the ABP system, except in this case the particles are almost always exclusively concentrated at the domain interfaces (see Figure 3-5c), which is primarily a direct result of their tethering locations between the A and B blocks. Indeed, this is the major driving force behind the differences between the phase diagrams of the ABP and APB systems; *i.e.*, the neutral particles serve to screen the A and B segments from each other, hence reducing the energetic contribution to the free energy. Consequently, at a specific value of f_A, the surface area of

the APB system can be significantly smaller than that of the ABP system where the majority of particles are dispersed within the B-rich domains. Hence the ratio S/V is smaller, allowing for corresponding ordered phases to exist at lower (when $f_A < 0.5$, higher when $f_A > 0.5$) values of f_A in the APB system than in the ABP one.

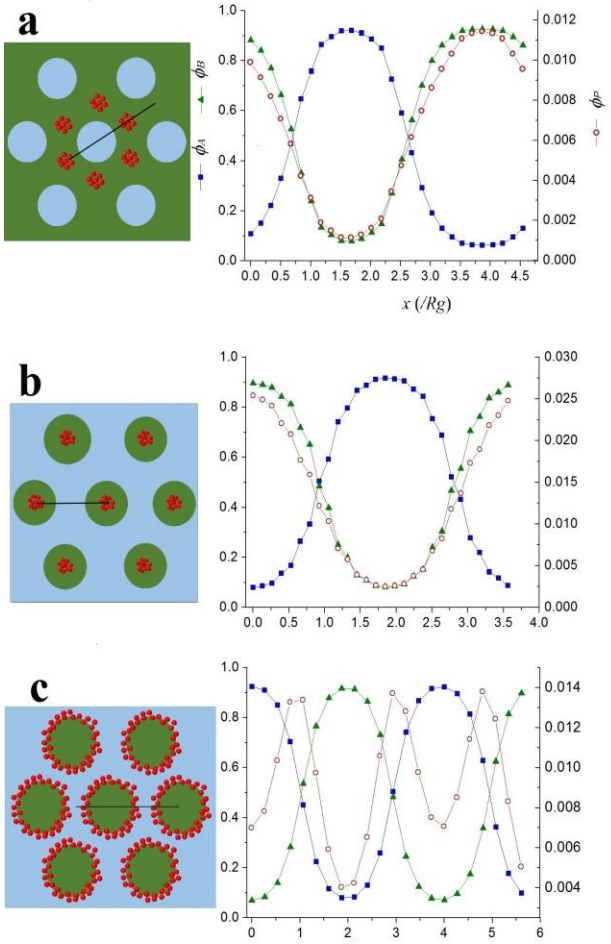

Figure 3-5. Schematic morphology of the cylinder hexagonal packing configuration (left) and density distributions (right) at $\chi_{AP}N = \chi_{BP}N = 0$, $\chi_{AB}N = 18$, and $R_P = 0.2R_g$ corresponding to **a)** $f_A = 0.3$, ABP system, **b)** $f_A = 0.7$, ABP system, and **c)** $f_A = 0.3$, APB system. The blue, green and red colors represent the A-rich domains, the B-rich domains, and the primary regions of particle concentrations, respectively. The density distributions in the right panels are calculated over the spatial periods indicated in the left panels by the solid black lines.

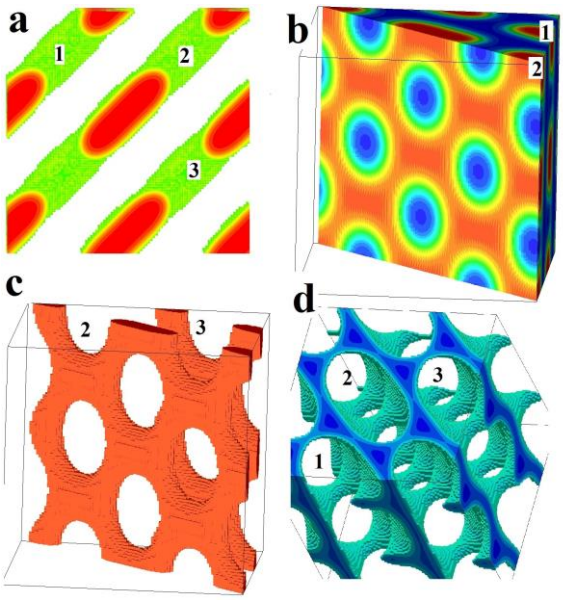

Figure 3-6. Configuration of the perforated lamellar phase (PL) for neutral particles in the ABP system at $f_A = 0.375$, $\chi_{AB}N = 18$, and $R_P = 0.2R_g$. **a)** The morphology of the A-block domain: 1, 2, and 3 are the layers formed by the A block. **b)** A side view from layer 2 to layer 1 (blue represents the B-block domain. **c)** The side view of the A-block domain (with $\phi_A > 0.8$) from layer 2 to layer 3. **d)** The B-block domain **(**$\phi_B > 0.8$).

The maxima in the particle density distributions, such as those in the right-side panels of Figure 3-5, are useful for quantifying the degree of relative concentration of particles at various locations within the ordered-phase morphology at $\chi_{AB}N = 18$. In Table 3-2, we present data for the maximum particle density and the morphology wherein it appears in reference to Figure 3-5, above, for neutral and interacting particles which disfavor both A and B segments for the ABP and APB systems. The symbol (a) denotes particles concentrated within hexagonally-arrayed nanowires within the B-rich matrix phase, (b) corresponds to particles concentrated at the center of A-rich cylinders, and (c) denotes particles lining the interfaces between the B-rich matrix phase and the A-rich cylindrical domains. Additionally, the symbols (*) and (**) denote the spheroidal morphology,

which assumes a body-centered cubic arrangement. Particles concentrate in the surrounding B-rich matrix in (*), whereas they concentrate at the interfaces of the A-rich spheroids in (**)

Table 3-2. Maximum particle densities (ϕ_P^{max}) and observed morphology of the ABP and APB systems as functions of particle radius and interaction parameter at $f_A = 0.3$ and $\chi_{AB}N = 18$. Numerical values correspond to ϕ_P^{max} whereas the letters denote the location of the particles with reference to the three cases of Fig. 3-5; *i.e.*, (a) represents particles concentrated within hexagonally-arrayed nanowires within the B-rich matrix phase, (b) corresponds to particles concentrated at the center of A-rich cylinders, and (c) denotes particles lining the interfaces between the B-rich matrix phase and the A-rich cylindrical domains.

ABP	$\chi_{AP}N = \chi_{BP}N$			
$R_P(R_g)$	0	5	10	15
0.1	0.0014 (a)	0.0014 (a)	0.0014 (a)	0.0014 (a)
0.2	0.011 (a)	0.011 (a)	0.011 (a)	0.011 (a)
0.3	0.034 (a)	0.034 (a)	0.034 (a)	0.034 (a)
0.4	0.07 (*)	0.07 (*)	0.07 (*)	0.07 (*)
APB	$\chi_{AP}N = \chi_{BP}N$			
$R_P(R_g)$	0	5	10	15
0.1	0.0018 (c)	0.0018 (c)	0.0018 (c)	0.0018 (c)
0.2	0.013 (c)	0.013 (c)	0.013 (c)	0.013 (c)
0.3	0.04 (c)	0.04 (c)	0.04 (c)	0.04 (c)
0.4	0.08 (**)	0.08 (**)	0.08 (**)	0.08 (**)

Note that (*) and (**) denote the spheroidal morphology, which assumes a body-centered cubic arrangement. Particles concentrate in the surrounding B-rich matrix in (*), whereas they surround the A-rich spheroids in (**).

The maximum particle density increases substantially as the particle size increases in both the ABP and APB systems, indicating that the particles are more preferentially concentrated in certain locations within the phase morphology, although this is to some degree simply an expected consequence of the increase in the global average particle density, f_P, with particle size. A more interesting observation is that ϕ_P^{max} is independent

of the particle/segment interaction strength for equally repulsive particles ($\chi_{AP}N = \chi_{BP}N > 0$); *i.e.*, each value of interaction strength in Table 3-2 has the same value of ϕ_P^{max} as the neutral particle case. Although the particle/segment interactions can affect the critical point (see Table 3-1), particularly at high particle radius, their effect on the maximum particle density is negligible, which is responsible for the common curve for the various entropy changes in Figure 3-3e,f. Because the particles are equally repulsive to both A and B segments, there is no net effect of internal energy on the configurational state of the copolymer chains; *i.e.*, whatever so happens to be the most favorable entropic configurational state of the neutral particle system also is the most favorable state of an interacting particle system. Hence the particular morphology formed at a given value of $\chi_{AB}N$ is independent of the interaction strength when the particles are equally repulsive to A and B segments.

Table 3-3 displays similar ϕ_P^{max} and morphology data as Table 3-2 for several different f_A phase points for the ABP and APB systems. These data exhibit the same trends as those of Table 3-2, but additionally illustrate the change in particle concentration that occurs as the particle tethering position changes and as the minority phase changes from A to B. Changing the tethering point of the particle at constant $f_A = 0.3$ results in a movement of the particles from the bulk B-rich matrix phase to the interfaces between the A and B domains. As f_A is increased from 0.3 to 0.7 in the ABP system, the morphology switches from the A-rich cylindrical phase to a B-rich cylindrical phase, with a migration of the particles to the center of the cylinders and a commensurate

dramatic increase in the particle concentration at the preferred location. Once again, there is no effect of particle/segment interaction strength on the position of the particles.

Table 3-3. Maximum particle density and the observed morphology for tethered particles as functions of particle radius and f_A for the ABP and APB systems at $\chi_{AB}N = 18$. (a) represents particles concentrated within hexagonally-arrayed nanowires within the B-rich matrix phase, (b) corresponds to particles concentrated at the center of A-rich cylinders, and (c) denotes particles lining the interfaces between the B-rich matrix phase and the A-rich cylindrical domains.

	ϕ_P^{max}			
System	R_P (for $\chi_{AP}N = \chi_{BP}N = 0$)			
	0.1	0.2	0.3	0.4
ABP: $f_A = 0.3$	0.0014 (a)	0.011 (a)	0.034 (a)	0.07 (*)
ABP: $f_A = 0.7$	0.0034 (b)	0.024 (b)	0.065 (b)	0.11 (b)
APB: $f_A = 0.3$	0.0018 (c)	0.013 (c)	0.04 (c)	0.08 (**)
	$\chi_{AP}N = \chi_{BP}N$ (for $R_p = 0.2$)			
System	0	5	10	15
ABP: $f_A = 0.3$	0.011 (a)	0.011 (a)	0.011 (a)	0.011 (a)
ABP: $f_A = 0.7$	0.024 (b)	0.024 (b)	0.024 (b)	0.024 (b)
APB: $f_A = 0.3$	0.013 (c)	0.013 (c)	0.013 (c)	0.013 (c)

Note that (*) and (**) denote the spheroidal morphology, which assumes a body-centered cubic arrangement. Particles concentrate in the surrounding B-rich matrix in (*), whereas they surround the A-rich spheroids in (**).

It is also interesting to study the effect of simulation box size on the observed morphology formed by the self-assembly of tethered-particle/copolymer materials. The constraint-free equilibrium morphology was always selected as that corresponding to the absolute minimum calculated value of the free energy, which was obtained by meticulously varying the simulation box dimensions over wider ranges of multiples of the copolymer radius of gyration; however, in so doing, we noted that the stable morphology varied remarkably with box size. In Figure 3-7, we display various system morphologies obtained at one distinct set of parameter values, $R_p = 0.2R_g$, $\chi_{AB}N = 18$, $\chi_{A/BP}N = 10$,

and $f_A = 0.3$ of the ABP system. The four morphologies observed in relation to box size were a) cylindrical minority phases arranged in quadrilateral arrays with particle-rich nanowires running axial-wise through the center of the interstice formed by four neighboring cylinders, b) ellipsoidal domains arranged in quadrilateral arrays, c) spheroids arranged on a body-centered cubic lattice, and d) hexagonally-packed cylinders (which was the globally stable phase). This illustrates clearly two points: 1) the effect of confinement to narrow dimensions upon the globally stable morphology induced by the self-assembly process, and 2) the great care that must be taken to ascertain the globally stable morphology when performing SCFT/DFT simulations. According to 1), it is possible to influence the morphology of a BCP-NP system considerably by applying boundary constraints (such as solid surfaces) upon the self-assembly process. With regard to 2), it is evident from Figure 3-7 that even in a constraint-free (unbounded) system, the global minimum in the free energy is not necessarily obtained in the limit of large box sizes; *i.e.*, the appropriate box size must be chosen so as to conform to the natural periodicity of the most stable morphology or else unphysical configurations can be forced upon the block copolymer chains, resulting in morphologies that would not otherwise be globally stable under equilibrium conditions.

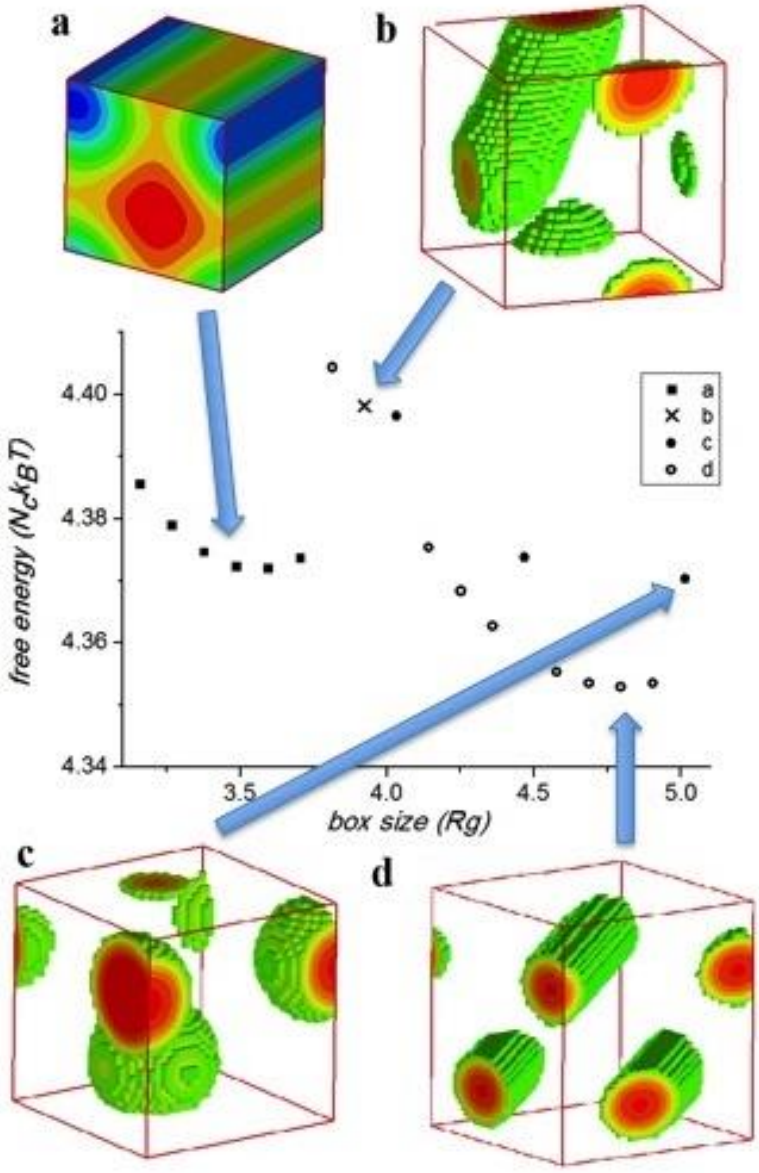

Figure 3-7. The box size confinement effect on the free energy and the resulting morphologies for $R_p = 0.2R_g$, $\chi_{AB}N = 18$, $\chi_{A/BP}N = 10$, and $f_A = 0.3$ of the ABP system: **a)** cylindrical domains in a quadrilateral array: the cylinders at the four corners (blue) are the A-block domains, and the red in the center is a particle nanowire; **b)** ellipsoidal domains in quadrilateral arrays; **c)** spheroids arranged on a body-centered cubic lattice; and **d)** hexagonally-packed cylinders. The **b, c**, and **d** cells show only the shape of the A-block domain (green and red).

Chapter 4

Self-assembly of a Diblock Copolymer under Application of an External Field

4.1 Methodology

In the framework of the SCFT/FENE-P method, the dimensionless free energy, F, (relative to nk_BT, where n is the number of chains, k_B is Boltzmann's constant, and T is the absolute temperature) consisted of the standard SCFT contribution and the free energy expression of the FENE-P dumbbell model, which yields

$$F = -\ln\left(Q/V\right) + \frac{1}{V}\int d\mathbf{r}\Big[\chi N\varphi_A\left(\mathbf{r}\right)\varphi_B\left(\mathbf{r}\right) - w_A\left(\mathbf{r}\right)\varphi_A\left(\mathbf{r}\right) - w_B\left(\mathbf{r}\right)\varphi_B\left(\mathbf{r}\right) - \xi\left(\mathbf{r}\right)\left(1-\varphi_A\left(\mathbf{r}\right)-\varphi_B\left(\mathbf{r}\right)\right) + \varphi_A\left(\mathbf{r}\right)\left[\widetilde{E}_A\left(\mathbf{r}\right) - \widetilde{TS}_A\left(\mathbf{r}\right)\right] + \varphi_B\left(\mathbf{r}\right)\left[\widetilde{E}_B\left(\mathbf{r}\right) - \widetilde{TS}_B\left(\mathbf{r}\right)\right]\Big] \tag{4.1}$$

In this expression, the $\varphi_A(\mathbf{r})$, $\varphi_B(\mathbf{r})$, $w_A(\mathbf{r})$, and $w_B(\mathbf{r})$ are the local volume fractions of the A-blocks and B-blocks and their local mean field potentials, respectively. $\xi(\mathbf{r})$ is the Lagrange multiplier (in the form of pressure) that is used to ensure the incompressibility condition is satisfied. The χN is the dimensionless Flory-Huggins interaction parameter, which describes the short-range chemical immiscibility between the A and B blocks, and $Q = \int q(\mathbf{r},s)q^{+}(\mathbf{r},s)d\mathbf{r}$ is the partition function of a single diblock copolymer chain in a volume, V, under the mean field. The last four terms, $\widetilde{E}_A$, $\widetilde{TS}_A$, $\widetilde{E}_B$ and $\widetilde{TS}_B$, on the right side of Eq. (4.1) are the dimensionless internal energy and entropic terms that are contributed by FENE-P model. The FENE-P internal energy, $\widetilde{E}_i(\mathbf{r})$, ($i$ =*A, B*), contains two parts: one

arises from the conformation tensor, $\tilde{E}_{ic}$, the other is from the external field, $\tilde{E}_{ie}$. These quantities depend on the state of the microstructure (*i.e.*, the extension and orientation of the local segment population), which is quantified using a dimensionless conformation tensor for each type of segment, as defined below. The entropic terms are also functions of the conformation tensor of each segment type. The relevant expressions are thus

$$\widetilde{E}_i\left(\mathbf{r}\right)=\widetilde{E}_{ie}\left(\mathbf{r}\right)+\widetilde{E}_{ic}\left(\mathbf{r}\right)=-\frac{1}{2}\mathbf{H}_i\mathbf{H}_i:\tilde{\mathbf{c}}_i\left(\mathbf{r}\right)\varphi_i\left(\mathbf{r}\right)-\frac{1}{2}\frac{K}{k_BT}R_0^2\ln\left(1-\frac{\mathbf{tr}\,\mathbf{c}_i\left(\mathbf{r}\right)}{R_0^2}\right) \tag{4.2}$$

$$\widetilde{TS}_i\left(\mathbf{r}\right)=\frac{TS\left(\mathbf{r}\right)}{nk_BT}=\frac{1}{2}\ln\left(\left(\frac{K}{k_BT}\right)^3\det\mathbf{c}\left(\mathbf{r}\right)\right) \tag{4.3}$$

The R_0 ($R_0=Nl$) is the maximum polymer chain length, where N is the segment number and l is the segment length. The K is the Hookean spring constant, which can be obtained via $Nl^2=3k_BT/K$. $\mathbf{H}_i$ is the dimensionless block external field interaction vector field, which is defined by Eq. (4.4), where the field is assumed to lie in the y-z plane pointed in the x-direction; therefore, we have $H_x=H_i\neq 0$.

$$\mathbf{H}=\begin{bmatrix}H_i\\0\\0\end{bmatrix} \tag{4.4}$$

The $\mathbf{c}(\mathbf{r})$ is the local conformation tensor of the polymer segment at position $\mathbf{r}$, which was rendered dimensionless according to $\tilde{\mathbf{c}}=\mathbf{c}K/k_BT$. This tensor is depicted below. Since the external field lies in the x-direction, the off-diagonal elements are all zero.

$$\tilde{\mathbf{c}}_i(\mathbf{r}) = \frac{\mathbf{c}(\mathbf{r})K}{k_B T} = \begin{bmatrix} \tilde{\mathbf{c}}_{i-xx}(\mathbf{r}) & \tilde{\mathbf{c}}_{i-xy}(\mathbf{r}) & \tilde{\mathbf{c}}_{i-xz}(\mathbf{r}) \\ \tilde{\mathbf{c}}_{i-yx}(\mathbf{r}) & \tilde{\mathbf{c}}_{i-yy}(\mathbf{r}) & \tilde{\mathbf{c}}_{i-yz}(\mathbf{r}) \\ \tilde{\mathbf{c}}_{i-zx}(\mathbf{r}) & \tilde{\mathbf{c}}_{i-xx}(\mathbf{r}) & \tilde{\mathbf{c}}_{i-zz}(\mathbf{r}) \end{bmatrix} = \begin{bmatrix} \tilde{\mathbf{c}}_{i-xx}(\mathbf{r}) & 0 & 0 \\ 0 & \tilde{\mathbf{c}}_{i-yy}(\mathbf{r}) & 0 \\ 0 & 0 & \tilde{\mathbf{c}}_{i-zz}(\mathbf{r}) \end{bmatrix} \quad (4.5)$$

Minimizing the total free energy with respect to the densities $\varphi_A(\mathbf{r})$, $\varphi_B(\mathbf{r})$, conformation tensor, $\tilde{\mathbf{c}}$, and mean field variables $w_A(\mathbf{r})$, $w_B(\mathbf{r})$, leads to the SCFT/FENE-P equations, given by

$$w_A(\mathbf{r}) = xN\varphi_B(\mathbf{r}) + \widetilde{E}_A(\mathbf{r}) - \widetilde{TS}_A(\mathbf{r}) + \xi(\mathbf{r}) \quad (4.6)$$

$$w_B(\mathbf{r}) = xN\varphi_A(\mathbf{r}) + \widetilde{E}_B(\mathbf{r}) - \widetilde{TS}_B(\mathbf{r}) + \xi(\mathbf{r}) \quad (4.7)$$

$$\varphi_A(\mathbf{r}) + \varphi_B(\mathbf{r}) = 1 \quad (4.8)$$

$$\varphi_A(\mathbf{r}) = -\frac{V}{Q}\frac{\partial Q}{\partial w_A(\mathbf{r})} = \frac{V}{Q}\int_0^{f_A} q(\mathbf{r},s)q^+(\mathbf{r},s)ds \quad (4.9)$$

$$\varphi_B(\mathbf{r}) = -\frac{V}{Q}\frac{\partial Q}{\partial w_B(\mathbf{r})} = \frac{V}{Q}\int_{f_A}^{1} q(\mathbf{r},s)q^+(\mathbf{r},s)ds \quad (4.10)$$

$$\frac{\partial q(\mathbf{r},s)}{\partial s} = \nabla^2 q(\mathbf{r},s) - w(\mathbf{r})q(\mathbf{r},s) \quad (4.11)$$

$$\frac{\partial q^+(\mathbf{r},s)}{\partial s} = -\nabla^2 q^+(\mathbf{r},s) + w(\mathbf{r})q^+(\mathbf{r},s) \quad (4.12)$$

$$-\frac{1}{2}H_\alpha H_\beta \varphi_i(\mathbf{r})\delta_{\alpha\beta} + \frac{1}{2}\left(\frac{R_0^2}{R_0^2 - \frac{k_B T}{K}\mathbf{tr}\tilde{\mathbf{c}}_i(\mathbf{r})}\right)\delta_{\alpha\beta} - \frac{\tilde{\mathbf{c}}_{i-\alpha\beta\gamma}(\mathbf{r})}{2} = 0 \quad (4.13)$$

These equations must be solved simultaneously to yield the SCFT/FENE-P model results. In the diffusion equations, Eqs. (4.11) and (4.12), the $w(\mathbf{r}) = w_A(\mathbf{r})$ for $0 \le s \le f_A$,

while $w(\mathbf{r}) = w_B(\mathbf{r})$ for $f_A < s \leq 1$. The $q(\mathbf{r}, s)$ and $q^+(\mathbf{r}, s)$ represent the chain propagators, with specific initial conditions: $q(\mathbf{r}, 0) = 1.0$ and $q^+(\mathbf{r}, 1) = 1.0$. Note that the Lagrange multiplier $\xi(\mathbf{r})$ and φ_i are not functions of $\tilde{\mathbf{c}}$. We assume there is only one segment in each cell, because the discretization will not affect the final result in the random walk model. Here, we define $a = -H_\alpha H_\beta$. Solving Eq. (4.11), we obtain the conformation tensor component expressions

$$\tilde{\mathbf{c}}_{i-xx}(\mathbf{r}) = \frac{3 + 3\varphi_i(\mathbf{r}) + 3a\varphi_i(\mathbf{r}) - \sqrt{-12a\varphi_i(\mathbf{r}) + \left(3 + 3\varphi_i(\mathbf{r}) + 3a\varphi_i(\mathbf{r})\right)^2}}{2a} \tag{4.14}$$

$$\tilde{\mathbf{c}}_{i-yy}(\mathbf{r}), \tilde{\mathbf{c}}_{i-zz}(\mathbf{r}) = \frac{-3 - 3\varphi_i(\mathbf{r}) + 3a\varphi_i(\mathbf{r}) + \sqrt{-12a\varphi_i(\mathbf{r}) + \left(3 + 3\varphi_i(\mathbf{r}) + 3a\varphi_i(\mathbf{r})\right)^2}}{2\left(2 + 3\varphi_i(\mathbf{r})\right)a} \tag{4.15}$$

We have performed simulations for field strengths in the range of $H_A \in [1.0,\ 8.0]$ in increments of 1.0 units. Only the A segments are significantly affected by the applied field, whereas the B segments are only mildly affected: $H_B = 0.01$, which was held constant over all simulations. Both H_A and H_B lie solely in the x-direction. The simulations were based on the following conditions: (1) 3 dimensional periodic boundary conditions were employed; (2) the number of polymer chain segments was 200; and (3) the simulation lattice cell size was 0.109 R_g, where R_g, is the radius of unperturbed polymer gyration. We performed verifications typically using 20 different box sizes varying from about 3.27 R_g to 5.45 R_g (from 30×30×30 to 50×50×50 cell numbers). All other aspects of the simulation methodology are as described in preceding chapters.

4.2 Results and Discussion

4.2.1 Polymer Conformation Tensor

In Eqs. (4.14) and (4.15), the diagonal components of conformation tensor in one cell ($\tilde{c}_{i-xx}$, $\tilde{c}_{i-yy}$, $\tilde{c}_{i-zz}$, i = *A, B*) only depend on the local block segmental density and the external field strength. Meanwhile, the block density distribution highly depends on the Flory-Huggins parameters χN via the modified diffusion equations (shown in Eqs. (4.11) and (4.12)). In our calculations, the $\boldsymbol{H}$ vector contains only one nonzero component (H_i, i=*A* or *B*) at position x (shown in Eq. (4.4)), and the value of H_A and H_B are both positive. Therefore, only the values of diagonal components in the conformation tensor ($\tilde{c}_{i-xx}$, $\tilde{c}_{i-yy}$, $\tilde{c}_{i-zz}$, i=*A* or *B*) are nonzero, and the polymer blocks would only be elongated along the x direction, and compressed in the y and z directions. The most stable value of $\tilde{c}_{i-xx}$, $\tilde{c}_{i-yy}$ and $\tilde{c}_{i-zz}$ (i=*A* or *B*) under the condition of φ_i=1.0, $H_i = 0.0$ is 0.5, and the trace of the conformation tensor is 1.5 according to the Eqs. (4.14) and (4.15). If the $H_i \to \infty$, the value of $\tilde{c}_{i-xx}$ goes to 3.0 while the $\tilde{c}_{i-yy}$, $\tilde{c}_{i-zz}$ would be reduced to 0.0, which implies the polymer chain is elongated into a straight line along the x direction. This is the limit of a Hookean dumbbell model.

The $\tilde{c}_{i-xx}$ component increases as either the block density or external field strength increases. As shown in Figure 4-1, the densities φ_A range from 0.0 to 1.0, the external field H_A varies from 0.0 to 8.0, and the $\tilde{c}_{A-xx}$ do not vary linearly with H_A (Eq. (4.14)). At low densities, the conformation tensor component $\tilde{c}_{A-xx}$ remains almost constant with varying external field strength; however, in the high density regime, especially when the density is close to 1.0, the $\tilde{c}_{A-xx}$ component changes dramatically with increasing H_A. For

the y and z directions, there is only a mild decrease with increasing field strength, since the chain compression perpendicular to the direction of extension is limited by the finite diameter of the chain. As for the conformation tensor of the B segments, the increase of $\tilde{c}_{B-xx}$ and the decreases in $\tilde{c}_{B-yy}$ and $\tilde{c}_{B-zz}$ are quite small because the B segment is not much affected by the external field ($H_B = 0.01$).

The results describe above are in no way surprising, or even interesting. They are exactly what one would expect from a polymer subjected to an external magnetic or electric field, being it susceptible to the same. What is interesting and surprising is the affect that the segmental orientation and extension has upon the stable morphological phase and its associated dimensions, as described below.

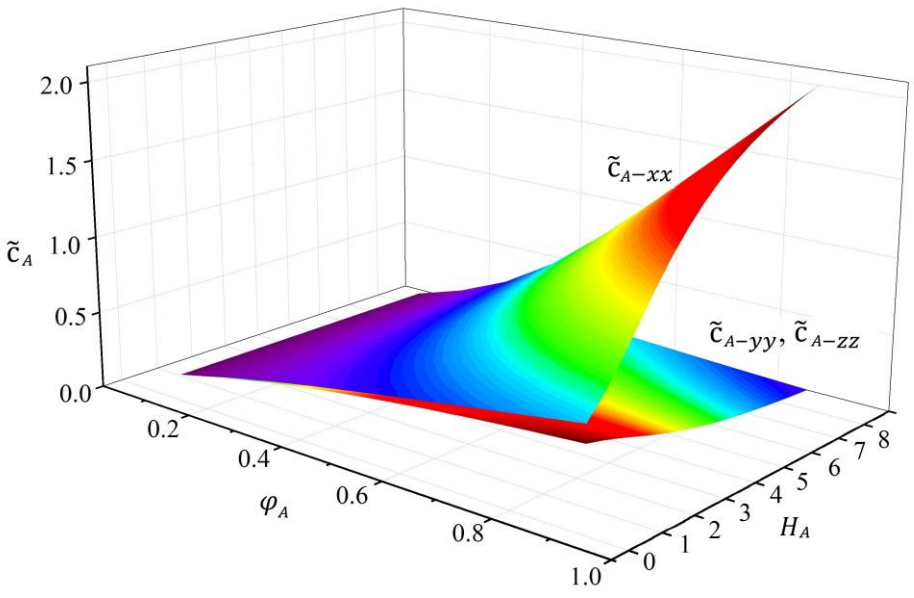

Figure 4-1. The dimensionless values of the diagonal components of the conformation tensor ($\tilde{c}_{A-xx}$, $\tilde{c}_{A-yy}$, and $\tilde{c}_{A-zz}$) as functions of external magnetic field strength (H_A) and density (φ_A).

4.2.2 Thermodynamic Properties

Given the number of parameters involved in this model, a complete exploration of the state space of the SCFT/FENE-P system is untenable as one of three projects comprising this dissertation. Therefore, no effort was made to present a complete and thorough description of the system properties. Rather, we chose to focus on one particular aspect of the system morphology: the effects of the external field on the critical dimensions and orientation of the lamellar morphology.

The free energy of lamellae-forming diblock copolymer systems was investigated under the conditions of f_A = 0.5; χN = 12.0, 15.0, 18.0, and H_A varying from 1.0 to 8.0 in increments of 1.0 The free energy of Eq. (4.1) is split into components arising from energetic effects (the χN, $\tilde{E}_i$ terms within the integral), which we assign the symbol *U*, and entropic effects (all other terms), which we define as $-TS$, according to the standard Legendre transformation, $F = U - TS$. The internal energy *U* can be divided into three components: chemical immiscibility of the blocks ($\chi N - U$), FENE-P model contribution (*FENE-P-U*), and the external field contribution ($H - U$).

4.2.2.1 Constant H_A

At a constant value of H_A, as χN increases, both the free energy *F*, and -*TS* also increase (*i.e.*, the value of *TS* decreases); however, the total internal energy *U* remains constant, as depicted in the Figure 4-2. A higher value of χN results in a greater degree of morphological phase separation, and therefore a more ordered arrangement. Therefore, the value of entropic term decreases. In Table 4-1, we list the value of each type of internal energy contribution in the case of χN = 12.0, 15.0, and 18.0 at H_A = 5.0. The

total internal energy of χN = 12.0, 15.0 and 18.0 are 1.0412, 1.0005, and 0.9680, respectively; as evident, they are very close to each other. It is apparent that with the increasing value of χN, the chemical immiscibility contribution to the internal energy increases, which is readily apparent from the Table 4-1. The *FENE-P* model contribution also increases as a result of higher microphase separation degree. The external field contribution $(H - U)$ assumes a negative value, which implies that the external field applies work to the system. However, the value of $H - U$ is also a function of the density. Thus the magnitude of the external field contribution will increase with rising values of H_A.

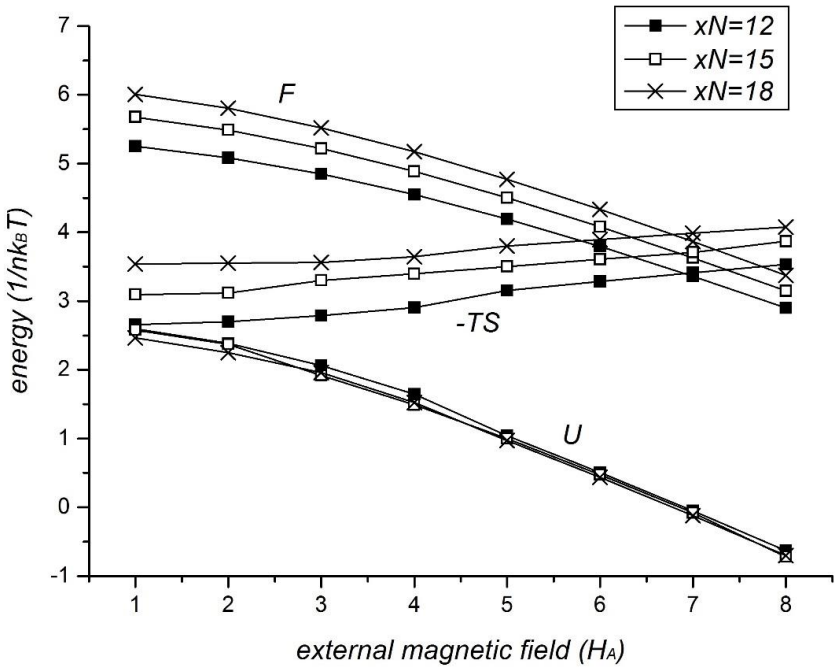

Figure 4-2. The energy analysis at different external field strengths (H_A) and block-block interactions (χN). The ■ represents the $\chi N = 12$, □ represents $\chi N = 15$ and × represents $\chi N = 18$ system.

Table 4-1. The internal energy contribution at H_A=5.0.

χN	12	15	18
χN -U	1.4435	1.4795	1.5025
FENE-P-U	1.3799	1.4556	1.5093
$H-U$	-1.7822	-1.9346	-2.0438
Total	1.0412	1.0005	0.9680

4.2.2.2 Constant χN

At constant χN, if H_A increases, both the free energy F and the internal energy U decrease; however, the -*TS* term increases, (which implies that the value of *TS* decreases), as displayed in the Figure 4-2. The values of each type of internal energy contribution in the cases of χN =18.0 as H_A varies from 1.0 to 8.0 are listed in Table 4-2. The $\chi N - U$ contribution decreases with increasing H_A ; however, there was a small increase at H_A = 2.0 and 3.0. The difference in $\chi N - U$ between two adjacent values of H_A is about 0.03-0.04, except at H_A = 0.4 and 0.5. The small decrease at these values is due to the density separation degree increasing, since the value of $\chi N - U$ is calculated according to $\chi N \varphi_A \varphi_B$. The sum of φ_A and φ_B always equals one; therefore, the higher separation degree, the lower the value of $\chi N - U$. The resulting values at H_A = 2.0 and 3.0 are due to the orientation of the lamellae. The higher value of H_A would also affect the mean field potential (Eqs. (4.6) and (4.7)) as well as the FENE-P energy (Eq. (4.2)). The energy of the spring is a function of the elongation; therefore, the higher the external field strength, the higher the value of *FENE-P-U*. The external field contribution is quite clear in this table: as H_A increases, more work is performed on the system and the internal energy of the system decreases.

Table 4-2. The internal energy contributions by chemical immiscibility, external field, and conformation orientation (in units of nk_BT).

HA	1.0	2.0	3.0	4.0	5.0	6.0	7.0	8.0
xN-U	1.607	1.589	1.616	1.586	1.503	1.470	1.438	1.407
FENE-P-U	1.019	1.131	1.258	1.385	1.509	1.612	1.704	1.787
H-U	-0.164	-0.473	-0.919	-1.450	-2.044	-2.647	-3.267	-3.898
Total	2.463	2.247	1.955	1.520	0.968	0.435	-0.125	-0.705

4.2.3 Lamellar Morphology

The density and microphase separation degree and the dimensions of the stable periodic lamellar morphology were also investigated under different conditions of H_A and χN (listed in the Table 4-3). As χN or H_A increase, the maximum densities of the A, B blocks (φ_{A-max} and φ_{B-max}), within the overall system, increases as discussed above. Most values of φ_{A-max} are higher than φ_{B-max}, except for two points (H_A=1.0 χN=12.0 and H_A=1.0 χN=15.0). The minimum densities of A, B blocks also behave in a similar way; therefore, the separation degree ($\Delta\varphi_A$ and $\Delta\varphi_B$) are the equivalent at the same values of H_A and χN, whereas the separation degree increases with increasing values of H_A and χN.

The stable periodic scale (l_s) increase with an increase of either H_A or χN, which implies that the stable morphology length scales are very sensitive to the specific values of H_A and χN. The absolute value of minimum free energy was obtained by meticulously varying the simulation box dimensions over wider ranges of multiples of the copolymer radius of gyration; however, in so doing, we noted that the stable morphology varied remarkably with box size, even though all of these morphologies were lamellar by nature and $f_A = 0.5$. It is evident that it is possible to tune the morphological length scale of a

BCP-NP system significantly by applying an external field. The A block thickness and its percentage will also increase with increasing H_A (around 0.5), which means that the relative contributions of the A block and B block to the whole system are almost equal. For lower H_A, the A block contribution is lower than 0.5, while as H_A increases, its value increases to 0.5 or even higher.

Table 4-3. The density properties and periodic scale of diblock lamellae morphology at f_A = 0.5.

χN	12.0	12.0	12.0	15.0	15.0	15.0	18.0	18.0	18.0
H_A	1.0	5.0	8.0	1.0	5.0	8.0	1.0	5.0	8.0
φ_{A-max}	0.920	0.962	0.978	0.966	0.983	0.991	0.989	0.993	0.995
φ_{A-min}	0.080	0.041	0.026	0.035	0.019	0.012	0.012	0.009	0.007
$\Delta\varphi_A$	0.841	0.921	0.952	0.931	0.964	0.979	0.977	0.983	0.988
φ_{B-max}	0.921	0.960	0.975	0.966	0.982	0.989	0.989	0.992	0.995
φ_{B-min}	0.080	0.039	0.023	0.035	0.018	0.011	0.012	0.009	0.007
$\Delta\varphi_B$	0.841	0.921	0.952	0.931	0.964	0.979	0.977	0.983	0.988
l_s	3.597	4.033	4.033	3.597	4.033	4.251	4.251	4.251	4.251
A thickness	1.744	1.962	2.071	1.744	1.962	2.071	2.071	2.071	2.180
Percentage	0.485	0.486	0.514	0.485	0.486	0.487	0.487	0.487	0.513

Chapter 5

Modelling Proton Conductivity in Perfluorosulfonate Acid Membranes

This chapter is based on the paper

"Proton Conductivity in Perfluorosulfonate Acid Membranes via Continuum Percolation Theory". B. Zhang, and B.J. Edwards. *J. Electrochem. Soc.* **162** (9), 2015[89]

5.1 Methodology

The morphology of a PFSA polymer membrane is herein idealized as a nanoporous network structure of indeterminate geometry. This network is stabilized throughout the membrane by the stiff helical backbones of the PFSA polymers with the short hydrophilic side chains protruding inside the pore walls. Water and hydronium ions occupy these pores to an extent determined by the applicable hydration level.[90] The architectures of the different membrane polymers (N, 3M, C, D) are displayed in Table 5-1. Each type of PFSA has a specific side-chain architectural unit. The C and N membranes have the same side chain, on which a $-CF_3$ group is attached, whereas the D membrane does not contain this unit and the monomer is shorter than for N and C. The 3M membrane shares a similar side-chain structure with the D membrane, although the side chain contains an additional $-(CF_2-CF_2)-$ linkage.[9, 61]The number of $-(CF_2-CF_2)-$ units is an average value calculated using the PFSA equivalent weight, *EW*, which is the ratio of the weight of dry membrane in grams to the moles of acid groups in the membrane, with units of g/mole. The *EW*s of N, 3M, C, and D are 1100, 1000, 900, and 800 g/mole, respectively, as listed in Table 5-1.

The overall membrane volume per sulfonic acid group V_o is defined as $V_o = EW/(N_A\rho_{dm})$, where N_A is Avogadro's number and ρ_{dm} is the dry membrane density. The monomer excluded volume, V_m, of the PFSA can be calculated using Chem3D software developed by CambridgeSoft® (PerkinElmer, Inc.) by inputting the architectural units of the various membranes, as depicted in Table 5-1. This software calculates the Connolly solvent-excluded surface (which is related to the volume contained within the accessible, or contact, molecular surface).[91] The contact surface was created using a spherical probe particle representing the solvent; the default probe radius used in the calculations was the standard 1.4 Å (the Van der Waals radius of a water molecule[92]) that is effectively rolled over the molecular model. The difference between these two volumes ($V_C = V_o - V_m$) is identified as the overall channel (or void) volume per sulfonic acid group, V_C, of the dry membrane. At zero hydration, this volume is assumed to be empty.

Table 5-1: Polymer monomeric architectures for Nafion 117, the 3M membrane, Membrane C, and Dow XUS 13204.10.

Name	Structure
Nafion 117 *EW*≈1100	-$(CF_2$-$CF_2)_6$-CF-CF_2- O-CF_2-CF-O-CF_2-CF_2-SO_3H CF_3
3M *EW*≈1000	-$(CF_2$-$CF_2)_6$-CF_2-CF- $OCF_2CF_2CF_2CF_2$-SO_3H
Membrane C *EW*≈900	-$(CF_2$-$CF_2)_4$-CF-CF_2- O-CF_2-CF-O-CF_2-CF_2-SO_3H CF_3
Dow *EW*≈800	-$(CF_2$-$CF_2)_5$-CF-CF_2- O-CF_2-CF_2-SO_3H

The water content of the model nanoporous network is defined as the number of water molecules per sulfonic acid group, and is denoted by the symbol λ. When the dry membrane is exposed to humidified air or immersed in the liquid water, water molecules are assumed to enter into the nanoporous network. At low vapor pressures, the water content of the membrane is very low and presumably the overall volume of the membrane changes little from its dry condition. Hence water fills the voids within the membrane material without affecting the morphology of the membrane. However, as the vapor-phase activity increases, the membrane will begin to swell with increasing water content as the water molecules expose more of the free volume to sulfonate-water interactions, hence altering the nature of the nanoporous network in terms of size, number, and connectivity of the channels.[47] With continued exposure to increasingly humidified vapor, we assume that a maximum in water absorption of the membrane will occur once all available free volume has been filled with water. According to this assumption, the maximum water capacity (λ_{max}) in the humidified vapor condition of the pore network can be calculated as $\lambda_{max} \approx V_C/V_w$, in which V_w is the spherical volume of one water molecule.

The mean van der Waals diameter of water has been reported as 2.82 Å;[92] however, radial distribution functions derived from interatomic energy potentials for water (such as the TIP3P model) in molecular dynamics simulations of hydrated Nafion provide an estimate of approximately 3.2 Å, which appears to be relatively independent of hydration level.[47] Note that this value is based on the distance between the oxygen atoms of neighboring water molecules and of hydronium ions, which is actually fairly typical of

radial distribution function data even in bulk water. Therefore, we assume the volume of a water molecule, V_w, to be 17.1 Å[62] based on a sphere of radius 1.6 Å, which is consistent with values measured experimentally in comparable nanoporous membranes.[93, 94] Note that this value corresponds to an effective partial molar volume for water in the membrane of 10.3 cm^3/mol, which is significantly smaller than the value of 18 cm^3/mol based on the density of pure water at room temperature; this latter value corresponds to a spherical molecular volume of 30 $Å^3$, or a molecular diameter of 3.8 Å. This is significantly higher than the van der Waals diameter of a water molecule because of the extensive hydrogen bonding network that exists in bulk water, and which is presumably destroyed within the confines of narrow and only partially hydrated pores, especially when the few water molecules present tend to cluster around the functional groups of the polymer chains.

In measurements of water sorption and hydrogen bonding in cellulose acetate membranes, Scherer and Bolton[94] found that the value of the partial molar volume of water, $\bar{V}_w$, at low hydration levels is substantially less than 30 $Å^3$/per molecule. Indeed, the applicable value of $\bar{V}_w$ and V_w depends on a balance between the membrane expansion caused by the intrusion of water into the pores and the filling of void spaces within the pores. It was determined that the molecular volume of water was a function of hydration level, varying between the van der Waals volume of a single water molecule, $V_w = 17.1$ $Å^3$, to that of a completely hydrogen-bonded molecule in bulk water, 30 $Å^3$. As a consequence, for purposes of determining the dry membrane density, we chose to use the value of 17.1 $Å^3$, which was the experimentally determined limit at low water content.

Scherer and Bolton[94] also found that the partial molar volume, $\bar{V}_w$, assumed effective values over the entire range of approximately zero to the bulk value of 30 Å^3/molecule because of what they termed "void utilization." Furthermore, Scherer[93] demonstrated for lipid bilayer systems that the partial molar volume of water was a strong function of the number of water molecules clustered around a lipid, exhibiting three regimes of behavior: 1) a region in which $\bar{V}_w$ and V_w is effectively a constant (10.3 cm^3/mol and 17.1 Å^3/molecule) value in the range of $[0, 5]$ water content, 2) a region of dramatic and essentially linear increase in $\bar{V}_w$ and V_w as functions of number of water molecules between roughly 5 and 20, and 3) another region of constant partial molar water volume with the plateau value $V_w = 30$ Å^3/molecule (the bulk value) for all higher water numbers. These data strongly suggest a 3-stage absorption mechanism for water in the lipid bilayer as a function of increasing hydration.

Further evidence in support of the 3-stage absorption process described above has been provided recently by Bai *et al*.,[95, 96] who also observed a dramatic, almost linear increase in the partial molar volume of water with increasing hydration level in several types of ionomeric membranes, including PFSAs. These authors showed that the membranes examined displayed a linear increase in the partial molar volume of water contained as a function of hydration level, specifically over ranges of water numbers approximately covering $\lambda \in [2, 6]$. The partial molar volume ranged from about 10 cm^3/mol at the low end of the range to the bulk value of about 18 cm^3/mol, in qualitative agreement with the results of Scherer and Bolton.[93, 94]

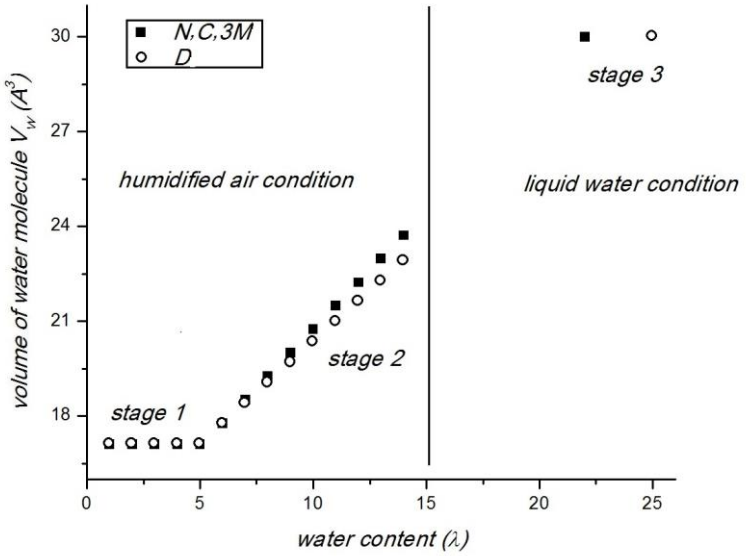

Figure 5-1: The volume of a water molecule (V_w) within a PFSA membrane as a function of water content according to the three-stage absorption hypothesis.

As the conductivity expression derived below depends critically on the partial molar volume of water within the membrane, we developed a 3-stage absorption process in view of the experimental data described above, which has also been hypothesized based on the molecular probe experiments of Spry and Fayer[11] as well as the results of several prior simulation studies of proton conduction is Nafion membranes. This series of stages will be described in more detail below; however, at this point, we begin by hypothesizing a variable molar volume of water which is qualitatively consistent with the results of Scherer and Bolton[93, 94] and Bai *et al*.,[95, 96] as displayed in Figure 5-1.

We hypothesize that the three distinct hydration regimes occurring in PFSA membranes induce different molecular conduction mechanisms for the protons. Within the range $\lambda \in [0,5]$, the water molecules tend to form tight clusters around the sulfonate groups with very little inter-cluster connectivity inside the pores, which is evident from

molecular dynamics simulations of the morphology of Nafion 117 (*EW*=1100) membranes at low water content.[47] These simulations showed that protons were hydrated by only two or three water molecules at low values of λ ($\leq$ 5), thus largely inhibiting structural diffusion (*i.e.*, proton transport via the creation and destruction of hydrogen bonds between neighboring water molecules, usually referred to as the Grotthuss mechanism) by prohibiting the formation of Eigen ion complexes. Hence most proton conduction at these low water contents is primarily vehicular, and likely induced by the gradient in the chemical potential across the membrane. Furthermore, the water clusters tended to be located in close proximity to the sulfonate groups.

Spry and Fayer's recent experiments determined that 3 to 4 water molecules per sulfonate group were required to form a hydration layer between the ions (*i.e.*, between contact ion pairs of sulfonate groups and hydronium ions), thus mobilizing the protons for transport.[11] This is consistent with findings from previous experiments of Zawodzinski *et al*., who found a distinct transition in water vapor activity (*i.e.*, solvation level) at a critical water content of approximately $\lambda \approx 5$ in the N, C, D, and 3M membranes.[9, 95-98] Again, these experiments appear to align with the hypothesis that conductivity at low water content is primarily limited to vehicular diffusion, or diffusion of hydronium ions between clusters once the percolation threshold has been achieved and a solvation layer interposed between the contact ion pairs of hydroniums and sulfonate groups.

Clark and Paddison[99, 100] have recently shown via *ab initio* electronic structure calculations of *EW*=590 and 690 PFSAs that approximately two water molecules are

required to hydrate fully a single proton, whereas it required 3-5 water molecules to hydrate a second, depending on the length of the side chains and their spacing along the polymer backbone. At low hydration levels, the established hydrogen-bond network involved two neighboring sulfonic acid groups and 2-5 water molecules forming a connectivity bridge between both side chains, again depending on the characteristic architecture of the polymer.[99-101] In addition, Choi and Datta[102] were able to model quantitatively the sorption data of Zawodzinski *et al.*[98] for water content versus activity by assuming five water molecules occupied the primary hydration shell surrounding each sulfonic acid group. In view of the above remarks, the proton conductivity at low hydration levels is essentially restricted to an effective volume determined by the upper limit of the low hydration regime, which we set to 5: $\lambda \in [0,5]$. Note that the effective conductivity range is defined as $\lambda \in [\lambda_0, 5]$, where λ_0 is the minimum water content necessary for a sufficient level of proton hydration necessary to achieve transport. The value of this quantity is typically approximately 2 for the membranes under consideration.[9, 103] Based on these arguments and the molecular simulations of molecular size of Cui *et al.*,[47] we set the molecular volume of water to have a constant value of 17.1 $Å^3$ within the range of $\lambda \in [\lambda_0, 5]$ in Figure 5-1.

The second proton conduction regime lies within the range $\lambda \in (5, \lambda_{max}]$, where the upper limit is the critical water content of the membrane as exposed to water vapor at 100% saturation and unit activity. For most of the membranes examined herein, $\lambda_{max} \approx 14$. In this hydration regime, the acidic protons have become fully hydrated and capable of experiencing transport via the Grotthuss mechanism over an extended network of

hydrogen-bonded water molecules and sulfonic acid groups. This corresponds to region 2 of the water uptake curves of Zawodzinski *et al*.[9, 98] where a rapid change in water activity occurred upon increased hydration level. Within this region, the authors hypothesized that water began to fill the nanopores and swell the membrane. Furthermore, the simulations of Nafion of Cui *et al.*[47] ($\lambda = 8.6, 11.8$) revealed large cluster formation of water molecules and hydronium ions around sulfonate ions, with radii of approximately 4.5 Å, which produced sample spanning, tortuous channels throughout the membrane. Furthermore, increasing the water content increasingly pulled the hydronium ions away from the sulfonate units, increasing the hydration level of the hydroniums to approximately eight water molecules each, although they remained generally situated in close proximity to the terminal groups[47] (in agreement with the experimental measurements of Spry and Fayer[11]). This simulated cluster size is consistent with the pore model of Choi and Datta,[102] who observed an increase of pore radius from approximately 2 nm at low water content to 4 nm at higher values; these values were also consistent with those obtained by Divisek *et al*. in the micropore region based on measurements of the pore size distribution of Nafion 117.[104]

Peterson and Voth[48] used empirical valence bond molecular dynamics simulations to show that structural diffusion of protons occurred at the same rate as vehicular diffusion, although the two processes were negatively correlated, for Nafion 117 at $\lambda = 15$, which is close to the experimental maximum water content for this membrane under exposure to water vapor ($\lambda = 14$).[9, 98] These authors demonstrated that a proton is solvated between two water molecules in a Zundel moiety in the vicinity of the contact ion, but transitions

into an Eigen-like configuration once a solvation layer has been interposed between the contact pair,[48] which evidence presented above suggests occurs around $\lambda = 5$.

For water contents lying within the second regime, $\lambda \in [5, \lambda_{max}]$, it is likely that the specific value of λ determines the ratio of structural to vehicular diffusion constants. As λ increases, it is probable that the structural contribution to proton transport increases; however, the negatively correlated vehicular component tends to offset this gain in proton transport, resulting in a slower rise in conductivity with increasing hydration level that one would intuitively expect. Note that this hypothetical slowdown in conductivity increase beginning at $\lambda = 5$ has been observed in experiment for several PFSA membranes.[9, 98] This hypothesis is also consistent with the observations of Spry and Fayer,[11] who found a slowed orientational diffusion of a probe molecule within water-filled pools of Nafion 117 membranes at higher water contents, which was probably due to the enhanced hydrogen bond network formed at elevated hydration levels. In essence, the hydrogen bond network slows down vehicular diffusion as the network tends to restrict the translational motion of the hydronium ions. Furthermore, any translational protonic motion that does occur will disrupt the hydrogen bond network, thus slowing structural diffusion; this possibly explains the negative correlation between vehicular and structural diffusive transport observed by Petersen and Voth.[48]

In view of the above-stated results, we hypothesize that the water content region $\lambda \in [5, \lambda_{max}]$ is also that within which the majority of the increase in the molecular volume of water occurs, which is approximately linear according to the available experimental data. Hence we assume that in stage 2 of the absorption mechanism, V_w

takes on a linear increase over the stated range, as in Figure 5-1, ultimately attaining the bulk value of 30 Å^3 in stage 3, which occurs under conditions of full membrane immersion in bulk water. The justification lies in the assumption that as the membrane swells, more volume becomes available to the pores, and the water is allowed to take on an increasingly normal or bulk-like molecular volume; this is consistent with the radial density profiles of Cui *et al*.[47] Hence at λ values corresponding to liquid immersion, the membrane has been expanded to a degree sufficient to allow bulk water type behavior within the pores, thus effectively limiting the conductivity of the membrane.

The dry membrane density of the Nafion and 3M membranes are known from experiments to be $\rho_{dm} = 2.05$ and 2.03 g/cm^3, respectively,[10, 95] whereas the dry membrane densities of the C and D and membranes have not been reported; however, these can be estimated from the experimental values of λ_{max} (the reported values[95, 99, 103] are presented in Table 5-2 below) according to

$$\rho_{dm} = \frac{EW}{N_A V_0} = \frac{EW}{N_A\left(V_m + V_C\right)} = \frac{EW}{N_A\left(V_m + \lambda_{\max} V_w\right)} \tag{5.1}$$

Table 5-2**:** The dry membrane densities and maximum water contents of the various PFSA membranes.

	N[a]	3M[a]	C[b]	D[b]
V_m (10^{-30} m	521	485	424	388
EW (g/mol)	1100	1000	900	800
ρ_{dm} (g/cm^3)	2.05	2.03	1.97	1.86
λ_{max}	15 (~14)	14 (~12)	~14	~14

a: The experimental value of the dry membrane density was known and the theoretical maximum water content in the vapor phase was calculated according to Eq (5.1)The numbers within the parentheses are the experimental values.[9, 95, 96, 98]
b: The experimental maximum water content was known and the dry membrane density was calculated according to Eq. (5.1).

For Nafion and 3M, using the known value of the dry membrane density yields a maximum water content in humidified vapor of 15 and 14, respectively, which is very close to the experimental values of approximately 14 and 12—see Table 5-2.[95, 98, 103] For the other two membranes, ρ_{dm} was estimated according to Eq. (5.1) using the experimental values of λ_{max} and V_w= 23.8 Å^3 (for C) and 23.2 Å^3 (for D) obtained from the linear interpolations of molecular water volume of Table 5-1; the results of these calculations are collected in Table 5-2. The values of ρ_{dm} thus calculated vary from one membrane to another in terms of both molecular architecture and equivalent weight (*EW*). With so few cases available to examine, it is difficult to establish definite trends of ρ_{dm} and λ_{max} variations with molecular architecture or *EW*; however, the density appears to decrease with decreasing *EW* of the membranes.

Theoretically, the number of hydronium ions inside the porous network should equal the number of sulfonic acid groups to satisfy the electroneutrality constraint. Thus the effective proton number density ($\bar{\rho}_\alpha$) per unit mass of membrane can be estimated by using the ratio of the number of protons with respect to the effective hydrophilic space (V_e),

$$\bar{\rho}_\alpha = \frac{1}{V_e} = \frac{1}{\lambda V_w} = \frac{N_A}{\lambda V_w} \ , \tag{5.2}$$

which depends on the number of water molecules present within the pores and the their effective size.

The overall transport of the hydronium ions and water molecules was assumed to be one-dimensional in the axial direction of an applied external field. Hence, we denote the

average momentum of the hydronium ions within the pore as $\bar{\rho}_\alpha u_\alpha$, where u_α is the average velocity in the axial direction. This velocity was calculated using the simplified Nernst-Einstein equation (*i.e.*, the density gradient was zero and the chemical potential gradient was completely determined by the external field, E_{ext}),

$$u_\alpha = \frac{D_P}{R_g T} F E_{ext} \ , \tag{5.3}$$

Accordingly, the velocity of the hydronium ions is functionally related only to the diffusivity of hydronium ions within the pore (D_p), and the magnitude of the external field (E_{ext}).[72] In this expression, R_g is the ideal gas constant, T is absolute temperature, and F is the Faraday constant. Therefore, the flux of charges within the pore, j, is expressed as

$$j = \bar{\rho}_\alpha u_\alpha \frac{F}{N_A} \ , \tag{5.4}$$

The proton conductivity, σ, of the pore is given by the ratio of the current density with respect to the external electric field. Therefore, by combining Eqs. (5.3) and (5.4), the conductivity can be determined as

$$\sigma = \frac{j}{E_{ext}} = \frac{D_P}{R_g T} F^2 \frac{\bar{\rho}_\alpha}{N_A} \ , \tag{5.5}$$

In this equation, the modified diffusion coefficient of hydronium ions within the pore, D_p, is a function of the architectural structure of the PFSA material, the water content, and the diffusion coefficient in bulk water, D_w, as discussed below—see Eq. (5.6). An effective structural coefficient, *K*, was introduced by Thampan *et al*. to account for the influence of the pore structure (and the associated surface charge density) on the

diffusion coefficient of the hydronium ions within the pore.[105] These authors established a power-law relationship between D_w and D_p using this structural coefficient

$$D_P = KD_w \ , \tag{5.6}$$

where

$$K = \left(\varepsilon_w - \varepsilon_{w0}\right)^q \ , \tag{5.7}$$

$$\varepsilon_w = \frac{\lambda \bar{V}_w}{\lambda \bar{V}_w + \bar{V}_m} = \frac{\lambda}{\lambda + \bar{V}_m / \bar{V}_w} \ , \tag{5.8}$$

$$\bar{V}_m = EW/\rho_{dm} \ , \tag{5.9}$$

$$D_w = \frac{k_B T}{2\pi\eta}\left(\frac{N_A}{V_w}\right)^{1/3} \ . \tag{5.10}$$

In these expressions, ε_w and ε_{w0} are the membrane porosities corresponding to water contents at λ and λ_0, respectively, k_B is Boltzmann's constant, and η is the viscosity of bulk water, which varies with temperature accordingly (as determined from published viscosity tables). λ_0 is the minimum water content below which proton diffusion does not occur (herein assumed to be $\lambda_0 = 1.9$)[9, 98, 103]. In Eq. (5.7), q is a structural parameter that is related to the nature of the nanoporous network structure and the fraction of a pore that is filled with water, under the assumption that the electrical conductivity follows a power-law relationship (Archie's law) with respect to porosity.[106-108] Combining these relationships provides an expression for the modified diffusion constant:

$$D_P = \left(\frac{\lambda}{\lambda + \dfrac{EW}{\bar{V}_w \rho_{dm}}} - \frac{\lambda_0}{\lambda_0 + \dfrac{EW}{\bar{V}_w \rho_{dm}}}\right)^q D_w \tag{5.11}$$

Eq. (5.7) was developed and motivated using continuum percolation theory, which delivers global properties, such permittivity, conductivity, and transport coefficients, from the disordered microstructural characteristics of the system.[106] When $\lambda \to \infty$, $q \to 0$ and $D_p = D_w$, which corresponds to the case of bulk water. As $\lambda \to \lambda_0$ from above, the percolation threshold is approached, below which $D_p = 0$. (The q parameter will be discussed in greater detail below.)

The porosity of the membrane, ε_w, is proportional to the size of the hydrophilic domain in the swollen membrane, which could be calculated through the volume fraction of water, as displayed in Eq. (5.8). The $\bar{V}_m$ and $\bar{V}_w$ are the partial molar volumes of dry membrane and water respectively, with the latter quantity be specified according to Figure 5-1. The molar volume of the dry membrane was approximated as the ratio of equivalent weight, *EW*, with respect to the density of the dry membrane, ρ_{dm}, according to Eq. (5.9).[106] When ε_w is larger than ε_{w0}, percolation occurs, wherein hydronium ion transport begins to take place through a model pore.[106] The size of a hydronium ion was assumed to be the same as that of a water molecule; hence, they were treated as identical particles. The expression of the self-diffusion coefficient, Eq. (5.10), was derived from the Stokes-Einstein equation,[72] and the conductivity expression was obtained by combining the Eqs. (5.6)-(5.10) as

$$\sigma = \left(\frac{\lambda}{\lambda + \dfrac{EW}{\bar{V}_w \rho_{dm}}} - \frac{\lambda_0}{\lambda_0 + \dfrac{EW}{\bar{V}_w \rho_{dm}}} \right)^q \frac{F^2 \bar{\rho}_\alpha}{2\pi\eta N_A^2} \left(\frac{N_A}{V_w} \right)^{1/3} . \tag{5.12}$$

Numerous papers have presented derivations and discussions of the exponent q in Eqs. (5.7) and (5.12), where it has been studied both in 2D and 3D simulations or experiments based on Archie's law.[109] This paradigm relates the electrical conductivity (σ) of a sedimentary solid object to its porosity and degree of water saturation (ϕ) via a power-law expression ($\sigma \propto (\phi - \phi_t)^q$).[107, 109] The exponent q varies with the nature of the microstructural domain of the pore network, and therefore reflects the effects of the pore microstructure as felt at the macroscopic scale (*i.e.*, over the entire material object).[108] Frisch *et al*. investigated the nature of the q parameter by introducing a 2D lattice gas automaton (LGA) model fluid in 1986.[110] In this approach, the fluid is simulated as a collection of discrete particles with specific values of mass and momentum. At each time step, particles move from one lattice unit to an adjacent site along the direction of flow. These particles might undergo collisions, but the mass, momentum, and energies are locally conserved. The porosity of the material is used to define the relative ratio of "fluid" sites (that is, the volume of the channel) to "solid" sites (representing the material object), the latter of which consist of standard geometries (such as triangles or diamonds) of adjacent sites arranged randomly within the lattice structure. Küntz *et al*. performed a numerical simulation of a 2-dimensional LGA fluid and found approximate values around 1.21 and 1.38 for the q parameter used in Eqs. (5.7) and (5.12).[108] Thompson *et al.* reported values of approximately 1.8 based on their experiments and simulations of 3-dimensional sandstone materials.[106, 111] Decreasing the degree of disorder of the transport medium could possibly reduce the value of q, which could be interpreted as the

fractal dimension of the channel or movement path, if we view the nature of the transport process to be in accordance with percolation theory.[107]

In a perfectly one-dimensional channel, a modified diffusion coefficient can be expressed as $D' = (p - p_0)D$, where p is a percolation probability parameter. If $p > p_0$, a percolation-type of diffusive process occurs; otherwise, there is no transport. Similarly, in a perfectly two-dimensional structure, the modified diffusion constant assumes the functional form $D' = (p - p_0)^2 D$. If the transport space is a fractal structure, however, q does not necessarily take on integer values. This phenomenon is very common in nature; *e.g.*, the dimensional boundary value of Brownian motion is 1.33 and that of a random walk without self-intersection is 1.55.[112] Nevertheless, q is commonly used as a fitting parameter with a value of approximately 1.5 ± 0.3 in both experiments and simulations, since the exact fractal dimensionality of the membrane is unknown.[10, 105, 113, 114] We will examine this parameter with respect to experimental trends in the following section.

5.2 Results and Discussion

5.2.1 Conductivity

Since the chosen value of q is based on the fractal dimension of a particle movement path, which is an unknown quantity for a typical PFSA membrane, its value must be treated as an empirical parameter to be fit to available experimental data. Consequently, plots of conductivity calculated according to Eq. (5.12) were compared with experimental data for the four membranes under investigation while adjusting the parameter q to obtain the best possible fit to the data. (Note that this was the only empirical parameter used in the model calculations, with the remainder of those appearing in Eq. (5.12) being

calculated according to the theory presented in the previous section and embodied by Eqs. (5.2)-(5.10).) Results of the calculations of conductivity versus water content at constant temperature (303 K) under a humidified air environment are presented in Figure 5-2 for the four membranes under investigation, plotted alongside the available experimental data.[95, 96, 98, 103]

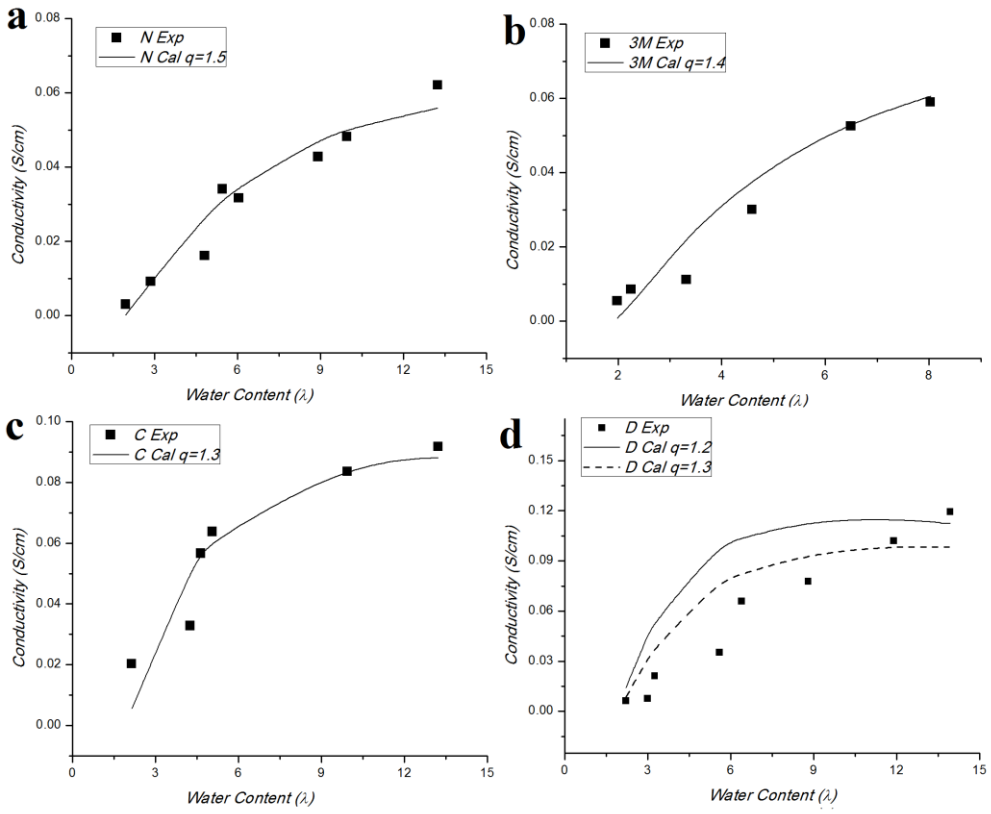

Figure 5-2: Comparison of conductivity vs. water content as calculated according to Eq. (12) and experiment data of four different membranes at 303 K: a.) N (*EW*=1100); b.) 3M (*EW*=1000); c.) C (*EW*=900); d.) D (*EW*=800).[95, 96, 98, 103] Note that the value of *q* decreases linearly with decreasing *EW*.

In general, the match between the experimental data and the model calculations is very good, with the exception of the Dow membrane. Values of *q* range from a maximum

value of 1.8 for the Nafion membrane to a value of 1.3 or 1.2 for the 3M membrane, depending on the perceived quality of the fit. These values of q are well within the range ($q = 1.5 \pm 0.3$) that is commonly associated with the applicable percolation theory. One immediately evident trend in Figure 5-2 is that of a decreasing value of q with decreasing *EW*; indeed, this decrease is essentially linear, indicating that, as the number of sulfonate groups increases relative to the dry membrane density (*i.e.*, as *EW* decreases), the membrane porosity apparently increases, thus creating larger and more connected channels in which the inhabitants increasingly assume the characteristics of bulk-like water. (Note that a decreasing value of q is consistent with increasingly bulk-like behavior of water; *e.g.*, the diffusion coefficients within the membrane pores of Eq. (5.6) become equivalent at $q = 0$.) If q is envisioned as a quantitative measure of membrane network "tortuosity," as some authors have stated,[72, 106, 107] then a decreasing value of this parameter again signals a more porous and more connected network of larger water clusters, in accordance with past simulation and experiment.[47, 48, 68]

For each membrane, the conductivity calculated according to Eq. (5.12) displays a dramatic increase at low hydration levels, $\lambda \in [0,5]$, and a rather slow increase thereafter, $\lambda \in [5.1,\ \lambda_{max}]$, ultimately approaching a plateau value as $\lambda \to \lambda_{max}$. Given the uncertainty associated with the experimental data, it is difficult to determine whether or not the experimental data actually display the model 2-stage conductivity trends described above; however, the overall quantitative agreement between the model calculations and experimental data is encouraging nonetheless. At low water contents, the protons are hydrated within water clusters and the primary mode of diffusion appears to

be vehicular, in which the hydronium ions move from one neighboring water cluster to another under the influence of osmotic drag. As λ continues to increase, however, structural diffusion plays an increasingly important role because water clusters become larger, allowing complex ionic structures to form, such as Zundel and Eigen ions. From the perspective of the simulation results of Petersen and Voth,[48] the eventual plateau of the model conductivity at high water contents is indicative of the negative correlation observed between vehicular and structural diffusion of the protons, as discussed in the preceding section. As such, the general trends displayed by the model can be interpreted as supporting the basic tenets of several prior simulation studies.[47, 48, 72, 99-101]

Figure 5-3 displays results of a comparison of the model calculations and the available experimental data[98, 103] for three of the membranes investigated above; note that there is no comparable data for the 3M membrane. These data were obtained under conditions of full membrane immersion in bulk water. The corresponding values of water content for each membrane are $\lambda = 22$ (N), $\lambda = 22$ (C), and $\lambda = 25$ (D). The observed qualitative trends displayed by the experimental data are captured well by the model calculations, especially for the Nafion and C membranes. The conductivity increases mostly linearly with increasing temperature, except at low values of T. The model conductivity equation,(5.12), is fit to the experimental data by varying the q parameter until an optimal value is obtained in each case. Values thus obtained are 1.2 for the Nafion membrane, 1.1 for the C membrane, and 0.9 for the Dow membrane. These values are somewhat lower than those obtained for conductivity data under humidified air conditions, which might be expected since fully immersed membranes would have lower

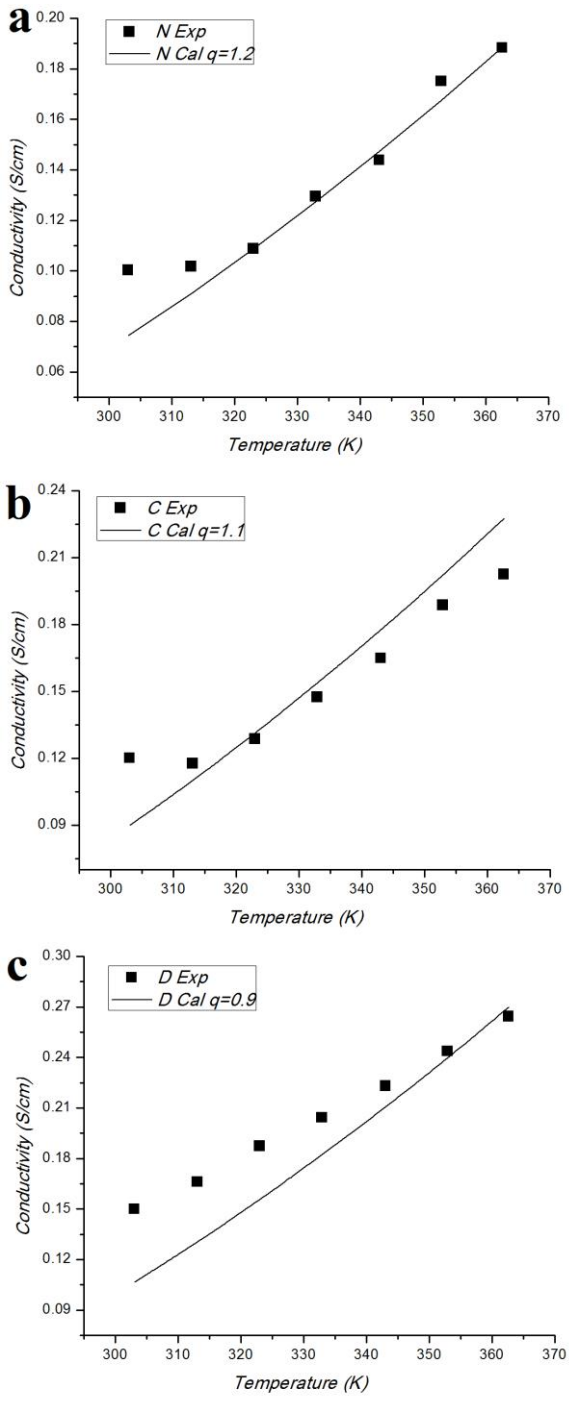

Figure 5-3: Comparison of conductivity vs. temperature as calculated according to Eq. (12) and experiment data of three different membranes at the λ value corresponding to full immersion in bulk water: a.) N ($\lambda = 22$); b.) C ($\lambda = 22$); c.) D ($\lambda = 25$).[98, 103]

densities and larger volumes, thus exhibiting more bulk-like behavior. Again, the value of q decreases almost linearly with decreasing membrane EW, indicating a general trend of more bulk-like behavior as the porosity of the PFSA membrane decreases, which is consistent with the decreasing trend in dry membrane density observed in Table 5-1. In each case, the experimental data and model calculations diverge primarily at low values of temperature, where proton and water molecule diffusion are relatively slow, indicating an opening of the network pore structure with increasing T. This is consistent with the hypothesis that the vehicular diffusion mechanism is relatively stronger at higher values of temperature. This is also consistent with lower values of q for each membrane with respect to the constant (low) temperature data of Figure 5-2.

5.2.2 Diffusivity of the PFSA Membrane Structure

In the preceding section, the diffusivity power-law exponent, q, was treated as a constant for each data series of conductivity, either as a function of water content (Figure 5-2) or temperature (Figure 5-3). It is also interesting to examine the variations in q that occur if it is allowed to vary from one data point to the next. In Figure 5-4, q is plotted versus temperature (Figure 5-4a) and versus water content (Figure 5-4b) for the four membranes under investigation. These curves were obtained by fitting Eq. (5.12) to each data point independently, instead of collectively, by optimizing the value of q in each case.

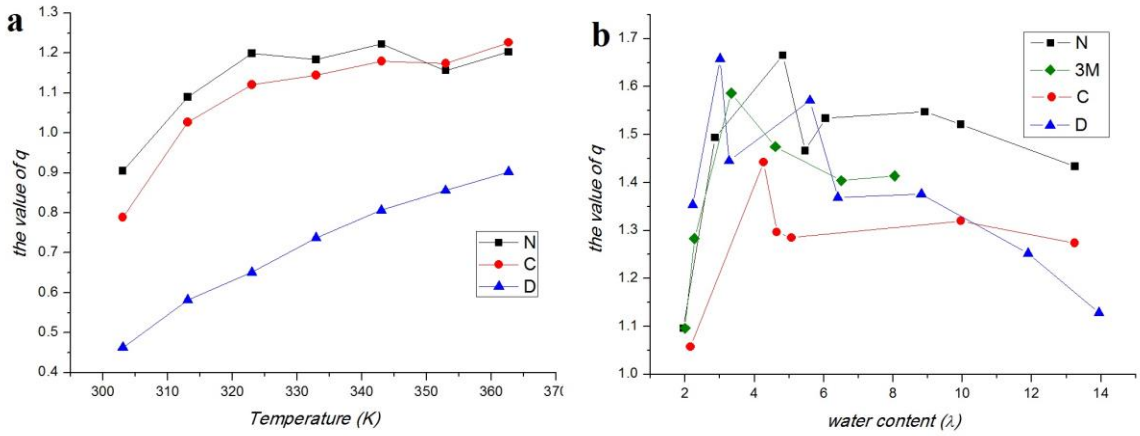

Figure 5-4: The value of q calculated from individual data points at different values of temperature (**a**) and water content (**b**) using the conductivity data of Figure 5-2 and Figure 5-3.

In Figure 5-4a, q increases steadily with increasing temperature for all three membranes; however, in most cases the increase occurs primarily at relatively low values of temperature and appears to approach a plateau at high values of T. In Figure 5-4b, there is a dramatic jump in the value of q in the first hydration regime of $\lambda \in [0,5]$, attaining a maximum at or near the upper limit of this range. Thereafter, q decreases slowly in the second hydration regime of $\lambda \in [5.1,\ \lambda_{max}]$.

As defined in Eqs. (5.6) and (5.7), this parameter is intimately related to the diffusion of the hydronium ions through the membrane channels, whether partially or fully filled with water. As q decreases toward zero, the diffusivity of Eq. (5.6) approaches that of bulk water. We hypothesize that the value of q is highly dependent on the type of hydronium transport process that occurs within the membrane. The data seem to suggest that q increases as the degree of structural diffusion increases, and decreases as vehicular diffusion becomes predominant.

With regard to Figure 5-4b, in the low hydration regime, q increases very quickly with λ as the additional water molecules enable a proton-hopping mechanism from one water cluster to the next. However, as the channels become more fully hydrated with water molecules at higher λ, vehicular diffusion is enabled and q begins to be affected by a process that tends to reduce this parameter toward its value in bulk water. Hence the specific value of q represents a balance between the two types of diffusive processes.

As for the temperature dependence of q observed in Figure 5-4a, at low temperatures, where the viscosity of water is relatively high, one might expect structural diffusion to play a more dominant role in the hydronium ion transport, whereas with decreasing viscosity, vehicular diffusion would become increasingly important. The observed trends in Figure 5-4a appear to support this hypothesis, with a sharp increase at low T and a slower increase at higher T, eventually leveling off to a plateau once the structural and vehicular transport mechanisms have attained some sort of equilibrium condition.

Chapter 6

Conclusions

6.1 Self-Consistent Field Theory

In summary, it was determined that there are a variety of 3-dimensional morphologies that can be produced from the self-assembly of diblock copolymer chains with tethered nanoparticles that possess the desired characteristics for potential application to nanofiltration membranes and other thin film applications. The targeted morphologies were those in which hexagonally packed cylinders, composed primarily of an easily degradable block, were formed within a surrounding non-degradable matrix phase, with a specific concentration of particles at the interface between the two domains. The cylinder diameter, hexagonal packing dimensions, and the distributions of particles at the interfaces could be tuned via varying the interaction parameters of the blocks and particles, as well as using the relative lengths of the copolymer blocks, f_A, thus providing an opportunity to tailor the steric and charge screening of potential nanofiltration and other ion transport membranes. As a general guideline, the greatest degree of interfacial particle concentration is achieved when the incompatibility between the two copolymer blocks is fairly high, but this may lead to cylinders of larger diameter with more diffuse interfaces for end-tethered particle systems. Hence both steric and charge exclusion would decrease simultaneously. However, the cylinder size could be more effectively controlled, especially if smaller diameter cylinders are desired with sharp interfaces, by choosing particles that are very incompatible with one of the copolymer blocks.

Nevertheless, the number of competing phenomena that contribute to the overall balance of entropy and energetic effects that constitute the overall free energy is so delicate that identifying general trends is very difficult.

The pore size is critical for steric exclusion in nanofiltration applications, as is their number density, which is closely related to the packing dimension of the hexagonal array. Both of these quantities need to be tuned to ensure that the membrane has a reasonable throughput at low pressures. Consequently, a balance must be struck between the pore diameter, the packing dimension, and the surface charge density of the particles in order to tailor the proper steric and charge exclusion for a particular nanofiltration application, and varying $\chi_{AB}N$ alone will likely not be effective.

The particle size was also shown to have a dramatic effect on the morphology and thermodynamics of both end-tethered and center-tethered particle/block copolymer systems. Increasing particle size raises the configurational entropy of the system, resulting in more disordered phases at equivalent values of the block length (f_A) and A-B block interaction strength ($\chi_{AB}N$). The particles generally congregate within the B-rich phase in the case of end-tethered particles, or at the interfaces between the A and B domains in the case of center-tethered particles, although the particular morphology formed, spheroidal, lamellar, or cylindrical, is highly dependent on the value of f_A. The number of stable morphologies is reduced as particle radii increases, with the perforated lamellar morphology disappearing for particle radii larger than $R_p = 0.3$. Which particular morphology was formed under a specific circumstance was also highly dependent on the nature of the particles; *i.e.*, how they interacted with the A and B

copolymer segments. Thermodynamically, the particle radius has a dramatic effect on the configurational entropy of the system, but only a relatively weak effect on the internal energy. Hence the free energy change that accompanies an increase in particle size is mostly due to its entropic contribution. The effect of particle size on the disorder/order phase transition was demonstrated to depend highly on the nature of the particles as well as the tethering point, with end-tethered particles displaying much larger variations in the critical value of $\chi_{AB}N$ due to the impact of energetic screening by the particles located at the interfaces for center-tethered particle systems.

Given these results, it is apparent that particle size, interaction $\chi_{ij}N$ and the molecular weight of the copolymer, could possibly be chosen *a priori* to coarse-tune the approximate pore size of the self-assembled membrane desired. The volume fraction of the A block, f_A, was determined to be only effective at fine-tuning the cylinder diameters and packing dimensions because these quantities vary only slightly with f_A since the C_A and C_B regions are rather narrow.

In Chapter 4, the SCFT/FENE-P model was developed. An applied external field was found to potentially dramatically affect the self-assembly of lamellar-forming diblock copolymer systems, and its effect on the free energy, separation density, periodic length scale, *etc*., were calculated. The symmetric, fully separated diblock copolymer system (f_A=0.5, χN =12.0, 15.0 and 18.0) under different external field strengths was investigated. Under different external field strengths, the behavior of the free energy, entropy, and internal energy are quite different than when the field is not present. Specifically, by changing the external field strength, the periodic length scale of the

lamellae and the A block thickness could be tuned. These results demonstrate a promising strategy for fabrication of new nanostructural membranes using external fields.

Given the enormous wealth of unexplored potential membrane materials, it is certainly possible that a judicious design of either a diblock copolymer system under external field or a diblock copolymer with tethered, charged nanoparticles could ultimately lead to advances in the applicability of nanofiltration and other ion transport membranes. The use of self-consistent field simulations offers another avenue of exploration in this direction for targeting specific design criteria, such as pore size and surface charge density, in block copolymer membrane production.

6.2 Conductivity Modeling

An expression for the quantification of proton conductivity in PFSA membranes was proposed based on a porous network model including a 3-stage absorption mechanism and a simplified version of the Nernst-Einstein relation. A prototypical membrane was modeled as an indeterminate collection of nanopores with the anionic groups (i.e., $–SO^{3–}$) assumed to line the insides of the pore walls as specified by the equivalent weight of the membrane and its dry density. Experimental data for conductivity of four common membranes were examined in light of this model in terms of a single parameter that was related to the diffusivity of hydronium ions within the membrane. The model matched the experimental trends reasonably well, both qualitatively and quantitatively, and provided insight into the nature of the diffusivity power-law exponent, which was hypothesized to increase at low water contents and temperatures where proton diffusion was primarily via

a structural or proton shuttling mechanism, and to decrease at high water contents or temperatures where diffusion was dominated by a vehicular mechanism.

List of References

1. Shim, Y.K. and S. Chellam, *Steric and electrostatic interactions govern nanofiltration of amino acids.* Biotechnology and Bioengineering, 2007. **98**(2): p. 451-461.
2. Hussain., A.A. and A.E. Al-Rawajfeh, *Recent Patents of Nanofiltration Applications in Oil Processing, Desalination, Wastewater and Food Industries,*, in *Recent Patents Chemi. Eng*. 2009. p. 51-66.
3. Donnan, F.G. and W.E. Garner, *Equilibria across a copper ferrocyanide and an amyl alcohol membrane.* Journal of the Chemical Society, 1919. **115**: p. 1313-1328.
4. Donnan, F.G., *The theory of membrane equilibria.* Chemical Reviews, 1924. **1**(1): p. 73-90.
5. Dutournie, P., et al., *Unsteady transport of divalent salt through a mineral membrane of ultrafiltration: Numerical estimation of physical parameters.* Desalination, 2011. **265**(1-3): p. 184-189.
6. Dutournie, P., et al., *Facilitated transport of monovalent salt mixture through ultrafiltration Na-Mordenite membrane: Numerical investigations of electric and dielectric contributions.* Desalination, 2011. **280**(1-3): p. 397-402.
7. Zhu, H.C., A. Szymczyk, and B. Balannec, *On the salt rejection properties of nanofiltration polyamide membranes formed by interfacial polymerization.* Journal of Membrane Science, 2011. **379**(1-2): p. 215-223.
8. Geise, G.M., et al., *Sodium chloride sorption in sulfonated polymers for membrane applications.* Journal of Membrane Science, 2012. **423**: p. 195-208.
9. Zawodzinski, T.A., et al., *Characterization of Polymer Electrolytes for Fuel-Cell Applications.* Solid State Ionics, 1993. **60**(1-3): p. 199-211.
10. Morris, D.R. and X.D. Sun, *Water-sorption and transport-properties of Nafion-117-H.* Journal of Applied Polymer Science, 1993. **50**(8): p. 1445-1452.
11. Spry, D.B. and M.D. Fayer, *Proton Transfer and Proton Concentrations in Protonated Nafion Fuel Cell Membranes.* Journal of Physical Chemistry B, 2009. **113**(30): p. 10210-10221.
12. Zhao, Q., et al., *Polyelectrolyte complex membranes for pervaporation, nanofiltration and fuel cell applications.* Journal of Membrane Science, 2011. **379**(1-2): p. 19-45.
13. Decher, G. and J.D. Hong, *Buildup of Ultrathin Multilayer Films by a Self-Assembly Process .1. Consecutive Adsorption of Anionic and Cationic Bipolar Amphiphiles on Charged Surfaces.* Makromolekulare Chemie-Macromolecular Symposia, 1991. **46**: p. 321-327.
14. Kulkarni, A., D. Mukherjee, and W.N. Gill, *Flux enhancement by hydrophilization of thin film composite reverse osmosis membranes.* Journal of Membrane Science, 1996. **114**(1): p. 39-50.
15. Fredrickson, G.H., *The Equilibrium Theory of Inhomogeneous Polymers*. 2006, Oxford: Oxford University Press.
16. Drolet, F. and G.H. Fredrickson, *Optimizing chain bridging in complex block copolymers.* Macromolecules, 2001. **34**(15): p. 5317-5324.

17. Drolet, F. and G.H. Fredrickson, *Combinatorial screening of complex block copolymer assembly with self-consistent field theory.* Physical Review Letters, 1999. **83**(21): p. 4317-4320.
18. Matsen, M.W. and F.S. Bates, *Origins of complex self-assembly in block copolymers.* Macromolecules, 1996. **29**(23): p. 7641-7644.
19. Matsen, M.W. and F.S. Bates, *Unifying weak- and strong-segregation block copolymer theories.* Macromolecules, 1996. **29**(4): p. 1091-1098.
20. Matsen, M.W. and F.S. Bates, *Block copolymer microstructures in the intermediate-segregation regime.* Journal of Chemical Physics, 1997. **106**(6): p. 2436-2448.
21. Daoulas, K.C., et al., *Fabrication of complex three-dimensional nanostructures from self-assembling block copolymer materials on two-dimensional chemically patterned templates with mismatched symmetry.* Physical Review Letters, 2006. **96**(3).
22. Ye, X.G., B.J. Edwards, and B. Khomami, *Block Copolymer Morphology Formation on Topographically Complex Surfaces: A Self- Consistent Field Theoretical Study.* Macromolecular Rapid Communications, 2014. **35**(7): p. 702-707.
23. Ye, X.G., B.J. Edwards, and B. Khomami, *Morphology Tailoring of Thin Film Block Copolymers on Patterned Substrates.* Macromolecular Rapid Communications, 2012. **33**(5): p. 392-395.
24. Ye, X.G., B.J. Edwards, and B. Khomami, *Elucidating the Formation of Block Copolymer Nanostructures on Patterned Surfaces: A Self-Consistent Field Theory Study.* Macromolecules, 2010. **43**(23): p. 9594-9597.
25. Choi, J.Y., et al., *Preparation and characterization of nanoporous films derived from alicyclic copolyimides having pendent poly(propyleneglycol) groups.* Polymer, 2012. **53**(6): p. 1328-1338.
26. Hirai, T., et al., *One-Step Direct-Patterning Template Utilizing Self-Assembly of POSS-Containing Block Copolymers.* Advanced Materials, 2009. **21**(43): p. 4334-+.
27. Sarkar, B. and P. Alexandridis, *Self-Assembled Block Copolymer-Nanoparticle Hybrids: Interplay between Enthalpy and Entropy.* Langmuir, 2012. **28**(45): p. 15975-15986.
28. Pan, Q.Y., C.H. Tong, and Y.J. Zhu, *Self-Consistent-Field and Hybrid Particle-Field Theory Simulation of Confined Copolymer and Nanoparticle Mixtures.* Acs Nano, 2011. **5**(1): p. 123-128.
29. Martin, T.B., A. Seifpour, and A. Jayaraman, *Assembly of copolymer functionalized nanoparticles: a Monte Carlo simulation study.* Soft Matter, 2011. **7**(13): p. 5952-5964.
30. Trombly, D. and V. Ganesan, *Interactions between Polymer-Grafted Particles and Bare Particles for Biocompatibility Applications.* Journal of Polymer Science Part B-Polymer Physics, 2009. **47**(24): p. 2566-2577.

31. Meli, L., A. Arceo, and P.F. Green, *Control of the entropic interactions and phase behavior of athermal nanoparticle/homopolymer thin film mixtures.* Soft Matter, 2009. **5**(3): p. 533-537.
32. Zhang, L., J. Lin, and S. Lin, *Self-assembly behavior of amphiphilic block copolymer/nanoparticle mixture in dilute solution studied by self-consistent-field theory/density functional theory.* Macromolecules, 2007. **40**(15): p. 5582-5592.
33. Sides, S.W., et al., *Hybrid particle-field simulations of polymer nanocomposites.* Physical Review Letters, 2006. **96**(25).
34. Pryamitsyn, V. and V. Ganesan, *Strong segregation theory of block copolymer-nanoparticle composites.* Macromolecules, 2006. **39**(24): p. 8499-8510.
35. Wang, Q., P.F. Nealey, and J.J. de Pablo, *Behavior of single nanoparticle/homopolymer chain in ordered structures of diblock copolymers.* Journal of Chemical Physics, 2003. **118**(24): p. 11278-11285.
36. Thompson, R.B., et al., *Block copolymer-directed assembly of nanoparticles: Forming mesoscopically ordered hybrid materials.* Macromolecules, 2002. **35**(3): p. 1060-1071.
37. Thompson, R.B., et al., *Predicting the mesophases of copolymer-nanoparticle composites.* Science, 2001. **292**(5526): p. 2469-2472.
38. Doi, M., *Introduction to Polymer Physics*. first ed. 2001, Great Britain: Clarendon press oxford. 115.
39. Huh, J., V.V. Ginzburg, and A.C. Balazs, *Thermodynamic behavior of particle/diblock copolymer mixtures: Simulation and theory.* Macromolecules, 2000. **33**(21): p. 8085-8096.
40. Reister, E. and G.H. Fredrickson, *Nanoparticles in a diblock copolymer background: The potential of mean force.* Macromolecules, 2004. **37**(12): p. 4718-4730.
41. Zhang, B., X.G. Ye, and B.J. Edwards, *A self-consistent field study of diblock copolymer/charged particle system morphologies for nanofiltration membranes.* Journal of Chemical Physics, 2013. **139**(24): p. 14.
42. Xu, G.K. and X.Q. Feng, *Position transitions of polymer-grafted nanoparticles in diblock-copolymer nanocomposites.* Express Polymer Letters, 2011. **5**(4): p. 374-383.
43. Zhu, X.M., et al., *Ordered Nanostructures Self-Assembled from Block Copolymer Tethered Nanoparticles.* Acs Nano, 2010. **4**(9): p. 4979-4988.
44. Chan, E.R., L.C. Ho, and S.C. Glotzer, *Computer simulations of block copolymer tethered nanoparticle self-assembly.* Journal of Chemical Physics, 2006. **125**(6).
45. Yockell-Lelievre, H., J. Desbiens, and A.M. Ritcey, *Two-dimensional self-organization of polystyrene-capped gold nanoparticles.* Langmuir, 2007. **23**(5): p. 2843-2850.
46. Schwab, J.J. and J.D. Lichtenhan, *Polyhedral oligomeric silsesquioxane (POSS)-based polymers.* Applied Organometallic Chemistry, 1998. **12**(10-11): p. 707-713.
47. Cui, S.T., et al., *A molecular dynamics study of a nafion polyelectrolyte membrane and the aqueous phase structure for proton transport.* Journal of Physical Chemistry B, 2007. **111**(9): p. 2208-2218.

48. Petersen, M.K. and G.A. Voth, *Characterization of the solvation and transport of the hydrated proton in the perfluorosulfonic acid membrane nafion.* Journal of Physical Chemistry B, 2006. **110**(37): p. 18594-18600.
49. Helfand, E., *Theory of Inhomogeneous Polymers - Fundamentals of Gaussian Random-Walk Model.* Journal of Chemical Physics, 1975. **62**(3): p. 999-1005.
50. Helfand, E. and A.M. Sapse, *Theory of Unsymmetric Polymer-Polymer Interfaces.* Journal of Chemical Physics, 1975. **62**(4): p. 1327-1331.
51. Yang, Y.L., et al., *Applications of self-consistent field theory in polymer systems.* Science in China Series B-Chemistry, 2006. **49**(1): p. 21-43.
52. Tang, P., et al., *Morphology and phase diagram of complex block copolymers: ABC linear triblock copolymers.* Physical Review E, 2004. **69**(3).
53. Tang, P., et al., *Morphology and phase diagram of complex block copolymers: ABC star triblock copolymers.* Journal of Physical Chemistry B, 2004. **108**(24): p. 8434-8438.
54. Kim, J.U., Y.B. Yang, and W.B. Lee, *Self-Consistent Field Theory of Gaussian Ring Polymers.* Macromolecules, 2012. **45**(7): p. 3263-3269.
55. Ginzburg, V.V., *Polymer-Grafted Nanoparticles in Polymer Melts: Modeling Using the Combined SCFT-DFT Approach.* Macromolecules, 2013. **46**(24): p. 9798-9805.
56. Warner, H.R., *Kinetic-Theory and Rheology of Dilute Suspensions of Finitely Extendible Dumbbells.* Industrial & Engineering Chemistry Fundamentals, 1972. **11**(3): p. 379-&.
57. Herrchen, M. and H.C. Ottinger, *A detailed comparison of various FENE dumbbell models.* Journal of Non-Newtonian Fluid Mechanics, 1997. **68**(1): p. 17-42.
58. Bird, R.B. and J.M. Wiest, *Constitutive-Equations for Polymeric Liquids.* Annual Review of Fluid Mechanics, 1995. **27**: p. 169-193.
59. Chilcott, M.D. and J.M. Rallison, *Creeping Flow of Dilute Polymer-Solutions Past Cylinders and Spheres.* Journal of Non-Newtonian Fluid Mechanics, 1988. **29**(1-3): p. 381-432.
60. Antony N. Beris, B.J.E., *Thermodynamics of Flowing Systems with Internal Microstructure*. 1994, New York Oxford: Oxford University Press.
61. Brandell, D., et al., *Molecular dynamics studies of the Nafion (R), Dow (R) and Aciplex (R) fuel-cell polymer membrane systems.* Journal of Molecular Modeling, 2007. **13**(10): p. 1039-1046.
62. Gierke, T.D., G.E. Munn, and F.C. Wilson, *The morphology in nafion perfluorinated membrane products, as determined by wide-angle and small-angle X-ray studies.* Journal of Polymer Science Part B-Polymer Physics, 1981. **19**(11): p. 1687-1704.
63. Ioselevich, A.S., A.A. Kornyshev, and J.H.G. Steinke, *Fine morphology of proton-conducting ionomers.* Journal of Physical Chemistry B, 2004. **108**(32): p. 11953-11963.

64. Rubatat, L., G. Gebel, and O. Diat, *Fibrillar structure of Nafion: Matching Fourier and real space studies of corresponding films and solutions.* Macromolecules, 2004. **37**(20): p. 7772-7783.
65. Rubatat, L., et al., *Evidence of elongated polymeric aggregates in Nafion.* Macromolecules, 2002. **35**(10): p. 4050-4055.
66. Kreuer, K.D., *On the development of proton conducting polymer membranes for hydrogen and methanol fuel cells.* Journal of Membrane Science, 2001. **185**(1): p. 29-39.
67. Starkweather, H.W., *Crystallinity in Perfluorosulfonic Acid Ionomers and Related Polymers.* Macromolecules, 1982. **15**(2): p. 320-323.
68. Schmidt-Rohr, K. and Q. Chen, *Parallel cylindrical water nanochannels in Nafion fuel-cell membranes.* Nature Materials, 2008. **7**(1): p. 75-83.
69. Din, X.D. and E.E. Michaelides, *Transport processes of water and protons through micropores.* Aiche Journal, 1998. **44**(1): p. 35-47.
70. Paddison, S.J., R. Paul, and T.A. Zawodzinski, *A statistical mechanical model of proton and water transport in a proton exchange membrane.* Journal of the Electrochemical Society, 2000. **147**(2): p. 617-626.
71. Paddison, S.J., R. Paul, and T.A. Zawodzinski, *Proton friction and diffusion coefficients in hydrated polymer electrolyte membranes: Computations with a non-equilibrium statistical mechanical model.* Journal of Chemical Physics, 2001. **115**(16): p. 7753-7761.
72. Kumar, M., B.J. Edwards, and S.J. Paddison, *A macroscopic model of proton transport through the membrane-ionomer interface of a polymer electrolyte membrane fuel cell.* Journal of Chemical Physics, 2013. **138**(6).
73. Hamley, I.W., et al., *Hexagonal Mesophases between Lamellae and Cylinders in a Diblock Copolymer Melt.* Macromolecules, 1993. **26**(22): p. 5959-5970.
74. Hajduk, D.A., et al., *The gyroid- a new equilibrium morphology in weakly segregated diblock copolymers.* Macromolecules, 1994. **27**(15): p. 4063-4075.
75. Schulz, M.F., et al., *Epitaxial Relationship for Hexagonal-to-Cubic Phase-Transition in a Block-Copolymer Mixture.* Physical Review Letters, 1994. **73**(1): p. 86-89.
76. Muller, M., K.C. Daoulas, and Y. Norizoe, *Computing free energies of interfaces in self-assembling systems.* Physical Chemistry Chemical Physics, 2009. **11**(12): p. 2087-2097.
77. Pan, Q.Y., et al., *Phase behaviors of bidisperse nanoparticle/block copolymer mixtures in dilute solutions.* Polymer, 2010. **51**(20): p. 4571-4579.
78. Wu, D.S., S.J. Paddison, and J.A. Elliott, *A comparative study of the hydrated morphologies of perfluorosulfonic acid fuel cell membranes with mesoscopic simulations.* Energy & Environmental Science, 2008. **1**(2): p. 284-293.
79. Carnahan, N.F. and K.E. Starling, *Equation of State for Nonattracting Rigid Spheres.* Journal of Chemical Physics, 1969. **51**(2): p. 635-&.
80. Johnston, K. and V. Harmandaris, *Hierarchical simulations of hybrid polymer-solid materials.* Soft Matter, 2013. **9**(29): p. 6696-6710.

81. Peaceman, D.W. and H.H. Rachford, *The Numerical Solution of Parabolic and Elliptic Diffrental Equations.* Journal of the Society for Industrial and Applied Mathematics, 1955. **3**(1): p. 28-41.
82. Eyert, V., *A comparative study on methods for convergence acceleration of iterative vector sequences.* Journal of Computational Physics, 1996. **124**(2): p. 271-285.
83. Thompson, R.B., K.O. Rasmussen, and T. Lookman, *Improved convergence in block copolymer self-consistent field theory by Anderson mixing.* Journal of Chemical Physics, 2004. **120**(1): p. 31-34.
84. Zhu, S., et al., *Confinement-induced miscibility in polymer blends.* Nature, 1999. **400**(6739): p. 49-51.
85. Zhang, B. and B.J. Edwards, *The Effect of Particle Size on the Morphology and Thermodynamics of Diblock Copolymer/Tethered-Particle Membranes.* Journal of Chemical Physics, 2015. **142**(21): p. 16.
86. Leibler, L., *Theory of Microphase Separation in Block Copolymers.* Macromolecules, 1980. **13**(6).
87. Fredrickson, G.H. and E. Helfand, *Fluctuation Effects in the Theory of Microphase Separation in Block Copolymers.* Journal of Chemical Physics, 1987. **87**(1): p. 697-705.
88. Marko, J.F., *Microphase Separation of Block Copolymer Rings.* Macromolecules, 1993. **26**(6): p. 1442-1444.
89. Zhang, B. and B.J. Edwards, *Modelling Proton Conductivity in Perfluorosulfonate Acid Membranes.* Journal of Electrochemical Society, 2015. **162**(9): p. 8.
90. Ilhan, M.A. and E. Spohr, *Hydrogen bonding in narrow protonated polymer electrolyte pores.* Journal of Electroanalytical Chemistry, 2011. **660**(2): p. 347-351.
91. Connolly, M.L., *Solvent-Accessible Surfaces of Proteins and Nucleic-Acids.* Science, 1983. **221**(4612): p. 709-713.
92. Franks F, W., *A matrix of life,* ed. 2nd. 2000, Cambridge: Royal Society of Chemistry.
93. Scherer, J.R., *The Partial Molar Volume of Water in Biological-Membranes.* Proceedings of the National Academy of Sciences of the United States of America, 1987. **84**(22): p. 7938-7942.
94. Scherer, J.R. and B.A. Bolton, *Water in Polymer Membranes. 5. on the Existence of Pores and Voids.* Journal of Physical Chemistry, 1985. **89**(16): p. 3535-3540.
95. Bai, Y.J., *Membrane and Performance Study in Polymer Electrolyte Membrane Fuel Cells and Hydrogen Bromine Redox Flow Batteries*, in *Chemical Engineering*. 2013, University of Tennessee, Knoxville: University of Tennessee, Knoxville, USA.
96. Bai, Y.J., et al., *Proton Conductivity and Partial Molar Volume of Different Polymer Electrolyte Membranes*, in *Polymer Electrolyte Fuel Cells 11*, H.A. Gasteiger, et al., Editors. 2011, Electrochemical Soc Inc: Pennington. p. 1545-1553.

97. Pushpa, K.K., D. Nandan, and R.M. Iyer, *Thermodynamics of Water Sorption by Perfluorosulfonate (Nafion-117) and Polystyrene-Divinylbenzene Sulfonate (Dow EX 50w) Ion-Exchange Resins at 298 +/- 1K.* Journal of the Chemical Society-Faraday Transactions I, 1988. **84**: p. 2047-2056.
98. Zawodzinski, T.A., et al., *A Comparative-study of water-uptake by and transport through ionomeric fuel-cell membranes.* Journal of the Electrochemical Society, 1993. **140**(7): p. 1981-1985.
99. Clark, J.K. and S.J. Paddison, *The effect of side chain connectivity and local hydration on proton transfer in 3M perfluorosulfonic acid membranes.* Solid State Ionics, 2012. **213**: p. 83-91.
100. Clark, J.K., S.J. Paddison, and S.J. Hamrock, *The effect of hydrogen bond reorganization and equivalent weight on proton transfer in 3M perfluorosulfonic acid ionomers.* Physical Chemistry Chemical Physics, 2012. **14**(47): p. 16349-16359.
101. Clark, J.K., II, *Ab Initio Studies of Proton Transport in Proton Exchange Membranes*. 2014, The University of Tennessee.
102. Choi, P., N.H. Jalani, and R. Datta, *Thermodynamics and proton transport in Nafion - II. Proton diffusion mechanisms and conductivity.* Journal of the Electrochemical Society, 2005. **152**(3): p. E123-E130.
103. Zawodzinski, T.A., et al., *Water-Uptake by and Transport Through Nafion(r) 117 Membranes.* Journal of the Electrochemical Society, 1993. **140**(4): p. 1041-1047.
104. Divisek, J., et al., *A study of capillary porous structure and sorption properties of Nafion proton-exchange membranes swollen in water.* Journal of the Electrochemical Society, 1998. **145**(8): p. 2677-2683.
105. Thampan, T., et al., *Modeling of conductive transport in proton-exchange membranes for fuel cells.* Journal of the Electrochemical Society, 2000. **147**(9): p. 3242-3250.
106. Hunt, A. and R. Ewing, *Percolation Theory for Flow in Porous Media, Second Edition*, in *Percolation Theory for Flow in Porous Media, Second Edition*. 2009, Springer-Verlag Berlin: Berlin. p. 1-319.
107. Hunt, A.G., *Continuum percolation theory and Archie's law.* Geophysical Research Letters, 2004. **31**(19): p. 4.
108. Kuntz, M., J.C. Mareschal, and P. Lavallee, *Numerical estimation of electrical conductivity in saturated porous media with a 2-D lattice gas.* Geophysics, 2000. **65**(3): p. 766-772.
109. Archie, G.E., *The electrical resistivity log as an aid in determining some reservoir characteristics.* Transactions of the American Institute of Mining and Metallurgical Engineers, 1942. **146**: p. 54-61.
110. Frisch, U., B. Hasslacher, and Y. Pomeau, *Lattice-Gas Automata for the Navier-Stokes Equation.* Physical Review Letters, 1986. **56**(14): p. 1505-1508.
111. Thompson, A.H., A.J. Katz, and C.E. Krohn, *The Microgeometry and Transport-Properties of Sedimentary-Rock.* Advances in Physics, 1987. **36**(5): p. 625-694.
112. Lawler, G.F., O. Schramm, and W. Werner, *The dimension of the planar Brownian frontier is 4/3.* Mathematical Research Letters, 2001. **8**(4): p. 401-411.

113. Newman, J.S., *Electrochemical Systems*. 1991, NJ: Prentice Hall.
114. Wesselingh, J.A., P. Vonk, and G. Kraaijeveld, *Exploring the Maxwell-stefand description of ion-exchange.* Chemical Engineering Journal and the Biochemical Engineering Journal, 1995. **57**(2): p. 75-89.

Vita

Bo Zhang was born in Beijing, China in 1988. He attended the Beijing Institute of Technology, China, in 2006 and received his bachelor degree of chemical engineering in 2010. After graduation, he went to the Department of Chemical and Biomolecular Engineering, University of Tennessee, Knoxville (UTK) to pursue graduate education in 2011. Bo joined Dr. Edwards' research group in spring of 2012. His research focuses on modified diblock copolymer morphology simulation and modeling the transfer properties through polymer membranes. The primary goal of his research is to elucidate under which conditions a copolymer system could form appropriate morphologies that could be used in nanofiltration or other membrane technologies. Bo got his Master of Science degree from the UTK in 2013.